

# Advanced Nanoengineering Materials

Lead Guest Editor: Leszek A. Dobrzański  
Guest Editors: Jorge R. Vargas-Garcia, Lothar Kroll,  
Anna D. Dobrzańska-Danikiewicz, and Sabu Thomas





---

# **Advanced Nanoengineering Materials**

Journal of Nanomaterials

---

## **Advanced Nanoengineering Materials**

Lead Guest Editor: Leszek A. Dobrzański

Guest Editors: Jorge R. Vargas-Garcia, Lothar Kroll,  
Anna D. Dobrzańska-Danikiewicz, and Sabu Thomas



---

Copyright © 2018 Hindawi. All rights reserved.

This is a special issue published in "Journal of Nanomaterials." All articles are open access articles distributed under the Creative Commons Attribution License, which permits unrestricted use, distribution, and reproduction in any medium, provided the original work is properly cited.

## Editorial Board

Domenico Acierno, Italy  
Katerina Aifantis, USA  
Nageh K. Allam, USA  
Margarida Amaral, Portugal  
Martin Andersson, Sweden  
Raul Arenal, Spain  
Ilaria Armentano, Italy  
Vincenzo Baglio, Italy  
Lavinia Balan, France  
Thierry Baron, France  
Andrew R. Barron, USA  
Hongbin Bei, USA  
Stefano Bellucci, Italy  
Enrico Bergamaschi, Italy  
D. Bhattacharyya, New Zealand  
Sergio Bietti, Italy  
Giovanni Bongiovanni, Italy  
Mohamed Bououdina, Bahrain  
Victor M. Castaño, Mexico  
Albano Cavaleiro, Portugal  
Bhanu P. S. Chauhan, USA  
Shafiq Chowdhury, USA  
Yu-Lun Chueh, Taiwan  
Elisabetta Comini, Italy  
Giuseppe Compagnini, Italy  
David Cornu, France  
Miguel A. Correa-Duarte, Spain  
P. Davide Cozzoli, Italy  
Anuja Datta, USA  
Loretta L. Del Mercato, Italy  
Yong Ding, USA  
Yu Dong, Australia  
Zehra Durmus, Turkey  
Joydeep Dutta, Oman  
Ovidiu Ersen, France  
Ana Espinosa, France  
Claude Estournès, France  
Andrea Falqui, Saudi Arabia  
Matteo Ferroni, Italy  
Ilaria Fratoddi, Italy  
Siddhartha Ghosh, Singapore  
Filippo Giubileo, Italy  
Fabien Grasset, France

Jean M. Greneche, France  
Kimberly Hamad-Schifferli, USA  
Simo-Pekka Hannula, Finland  
Michael Harris, USA  
Yasuhiko Hayashi, Japan  
Michael Z. Hu, USA  
Nay Ming Huang, Malaysia  
Zafar Iqbal, USA  
Balachandran Jeyadevan, Japan  
Jeong-won Kang, Republic of Korea  
Hassan Karimi-Maleh, Iran  
Antonios Kelarakis, UK  
Alireza Khataee, Iran  
Ali Khorsand Zak, Iran  
Philippe Knauth, France  
Prashant Kumar, UK  
Eric Le Bourhis, France  
Jun Li, Singapore  
Meiyong Liao, Japan  
Shijun Liao, China  
Silvia Licocchia, Italy  
Nathan C. Lindquist, USA  
Zainovia Lockman, Malaysia  
Jim Low, Australia  
Gaurav Mago, USA  
Muhamamd A. Malik, UK  
Francesco Marotti de Sciarra, Italy  
Ivan Marri, Italy  
Laura Martinez Maestro, UK  
Sanjay R. Mathur, Germany  
Tony McNally, UK  
Yogendra Mishra, Germany  
Paulo Cesar Morais, Brazil  
Paul Munroe, Australia  
Jae-Min Myoung, Republic of Korea  
Rajesh R. Naik, USA  
Albert Nasibulin, Russia  
Toshiaki Natsuki, Japan  
Hiromasa Nishikiori, Japan  
Natalia Noginova, USA  
Sherine Obare, USA  
Won-Chun Oh, Republic of Korea  
Abdelwahab Omri, Canada

Ungyu Paik, Republic of Korea  
Piersandro Pallavicini, Italy  
Edward A. Payzant, USA  
Alessandro Pegoretti, Italy  
Oscar Perales-Pérez, Puerto Rico  
Jorge Pérez-Juste, Spain  
Alexey P. Popov, Finland  
Thathan Premkumar, Republic of Korea  
Helena Prima-García, Spain  
Alexander Pyatenko, Japan  
Haisheng Qian, China  
You Qiang, USA  
Philip D. Rack, USA  
Peter Reiss, France  
Ilker S. Bayer, Italy  
Lucien Saviot, France  
Sudipta Seal, USA  
Shu Seki, Japan  
Donglu Shi, USA  
Bhanu P. Singh, India  
Surinder Singh, USA  
Vladimir Sivakov, Germany  
Adolfo Speghini, Italy  
Marinella Striccoli, Italy  
Fengqiang Sun, China  
Xuping Sun, Saudi Arabia  
Ashok K. Sundramoorthy, India  
Angelo Taglietti, Italy  
Bo Tan, Canada  
Leander Tapfer, Italy  
Valeri P. Tolstoy, Russia  
Muhammet S. Toprak, Sweden  
R. Torrecillas, Spain  
Achim Trampert, Germany  
Takuya Tsuzuki, Australia  
Tamer Uyar, Turkey  
Luca Valentini, Italy  
Antonio Vassallo, Italy  
Ester Vazquez, Spain  
Ajayan Vinu, Australia  
Ruibing Wang, Macau  
Shiren Wang, USA  
Yong Wang, USA



---

Magnus Willander, Sweden  
Ping Xiao, UK  
Zhi Li Xiao, USA  
Yingchao Yang, USA

Yoke K. Yap, USA  
Dong Kee Yi, Republic of Korea  
Jianbo Yin, China  
William Yu, USA

Michele Zappalorto, Italy  
Renyun Zhang, Sweden

# Contents

## **Advanced Nanoengineering Materials**

Leszek A. Dobrzański , Jorge R. Vargas-Garcia , Lothar Kroll,  
Anna D. Dobrzańska-Danikiewicz, and Sabu Thomas  
Editorial (1 page), Article ID 8469651, Volume 2018 (2018)

## **Magneto-Optic Properties of Ultrathin Nanocrystalline Ferrite Garnet Films in the 8K to 300K Temperature Interval**

V. A. Kotov , V. G. Shavrov, A. F. Popkov, M. Vasiliev, K. Alameh, M. Nur-E-Alam , L. N. Alyabyeva,  
D. E. Balabanov, V. I. Burkov, and M. K. Virchenko  
Research Article (12 pages), Article ID 7605620, Volume 2018 (2018)

## **Overcoming Multidrug Resistance by On-Demand Intracellular Release of Doxorubicin and Verapamil**

Jianwei Jiang , Shaojuan Liu, Chunlei Wang, and Hongyan Zhang   
Research Article (7 pages), Article ID 3568190, Volume 2018 (2018)

## **Nano-(Ta, Zr)C Precipitates at Multigrain Junctions in TaC Ceramic with 10 mol% ZrC and 5 mol% Cu as Sintering Aid**

Lianbing Zhong, Guihong Geng, Yujin Wang, Feng Ye, and Limeng Liu   
Research Article (5 pages), Article ID 1634814, Volume 2018 (2018)

## **Influence of Milling Time on Structural and Microstructural Parameters of Ni<sub>50</sub>Ti<sub>50</sub> Prepared by Mechanical Alloying Using Rietveld Analysis**

E. Sakher , N. Loudjani, M. Benchiheb, and M. Bououdina   
Research Article (11 pages), Article ID 2560641, Volume 2018 (2018)

## **Dynamic Infrared Thermography of Nanoheaters Embedded in Skin-Equivalent Phantoms**

K. A. López-Varela , N. Cayetano-Castro, E. S. Kolosovas-Machuca, F. J. González , F. S. Chiwo,  
and J. L. Rodríguez-López   
Research Article (8 pages), Article ID 3847348, Volume 2018 (2018)

## **Antimicrobial Nanocomposites Prepared from Montmorillonite/Ag<sup>+</sup>/Quaternary Ammonium Nitrate**

Lin Zhang, Jienan Chen , Wenji Yu, Qingfeng Zhao, and Jin Liu  
Research Article (7 pages), Article ID 6190251, Volume 2018 (2018)

## Editorial

# Advanced Nanoengineering Materials

**Leszek A. Dobrzański** <sup>1</sup>, **Jorge R. Vargas-Garcia** <sup>2</sup>, **Lothar Kroll**,<sup>3</sup>  
**Anna D. Dobrzańska-Danikiewicz**,<sup>4</sup> and **Sabu Thomas**<sup>5</sup>

<sup>1</sup>Medical and Dental Engineering Centre for Research, Design, and Production, Asklepios, Gliwice, Poland

<sup>2</sup>Instituto Politécnico Nacional, Mexico City, Mexico

<sup>3</sup>University of Chemnitz, Chemnitz, Germany

<sup>4</sup>University of Zielona Góra, Zielona Góra, Poland

<sup>5</sup>Mahatma Gandhi University, Kottayam, India

Correspondence should be addressed to Leszek A. Dobrzański; [leszek.adam@gmail.com](mailto:leszek.adam@gmail.com)

Received 5 July 2018; Accepted 6 August 2018; Published 5 September 2018

Copyright © 2018 Leszek A. Dobrzański et al. This is an open access article distributed under the Creative Commons Attribution License, which permits unrestricted use, distribution, and reproduction in any medium, provided the original work is properly cited.

The Guest Editors for this Special Issue were pleased to welcome contributions from researchers studying advanced nanomaterials and nanocomposites from both fundamental and applied perspectives. Manuscripts covered their applications, their development perspectives, their product design, and methods for the investigation of their structure and properties.

Three articles concentrated on bioapplications of nanoengineered materials. K. A. López-Varela et al. explored multibranching gold nanoparticles as a promising tool for localized photothermal therapy. J. Jiang et al. investigated gold liposomes for light-responsive drug release. L. Zhang et al. developed novel nanocomposites with antimicrobial activity against a wide variety of microorganisms.

Meanwhile, the remaining articles probed structural and physical properties. V. A. Kotov et al. studied the preparation and magneto-optical properties of ultrathin bismuth-substituted iron garnet films. E. Sakher et al. used X-ray diffraction techniques to follow the mechanical alloying of Ni and Ti elemental powders into nanocrystalline materials, uncovering details of the phase composition over time. Lastly, L. Zhong et al. uncovered a new type of TaC ceramic containing nanoprecipitates, which may warrant further research.

Although these six papers cannot provide the full image of the field of advanced nanoengineering materials, we nevertheless hope that the combination of these contributed papers will stimulate readers' imagination around

the multifaceted nature and possible effects of this research, and more importantly will inspire them to undertake their work in this very wide and open area of investigation.

## Conflicts of Interest

The editors declare that they have no conflicts of interest regarding the publication of this Special Issue.

## Acknowledgments

We would like to give warm thanks to all authors who submitted their manuscripts to this Special Issue, the editors who have spent their time selecting reviewers and making editorial decisions, and of course the reviewers for providing their expert opinions.

*Leszek A. Dobrzański  
Jorge R. Vargas-Garcia  
Lothar Kroll  
Anna D. Dobrzańska-Danikiewicz  
Sabu Thomas*

## Research Article

# Magneto-Optic Properties of Ultrathin Nanocrystalline Ferrite Garnet Films in the 8K to 300K Temperature Interval

V. A. Kotov <sup>1</sup>, V. G. Shavrov,<sup>1</sup> A. F. Popkov,<sup>2</sup> M. Vasiliev,<sup>3</sup> K. Alameh,<sup>3</sup> M. Nur-E-Alam <sup>3</sup>,  
L. N. Alyabyeva,<sup>4</sup> D. E. Balabanov,<sup>4</sup> V. I. Burkov,<sup>4</sup> and M. K. Virchenko<sup>5</sup>

<sup>1</sup>*Institute of Radio Engineering and Electronics, Russian Academy of Sciences, 11 Mohovaya St., Moscow 125009, Russia*

<sup>2</sup>*National Research University of Electronic Technology-MIET, Bld. 1, Shokin Square, Zelenograd, Moscow 124498, Russia*

<sup>3</sup>*Electron Science Research Institute, Edith Cowan University, 270 Joondalup Dr, Joondalup, WA 6027, Australia*

<sup>4</sup>*Moscow Institute of Physics and Technology, 9 Institutski Per., Dolgoprudny 141700, Russia*

<sup>5</sup>*NIIMV, 4/2 Georgievskiy Avenue, Zelenograd, Moscow 124460, Russia*

Correspondence should be addressed to V. A. Kotov; [kotov.slava@gmail.com](mailto:kotov.slava@gmail.com) and M. Nur-E-Alam; [m.nur-e-alam@ecu.edu.au](mailto:m.nur-e-alam@ecu.edu.au)

Received 28 September 2017; Accepted 16 April 2018; Published 22 July 2018

Academic Editor: Anna D. Dobrzańska-Danikiewicz

Copyright © 2018 V. A. Kotov et al. This is an open access article distributed under the Creative Commons Attribution License, which permits unrestricted use, distribution, and reproduction in any medium, provided the original work is properly cited.

A study of the initial stages of crystallization in RF magnetron-sputtered ferrite garnet films is reported, in which a series of ultrathin  $\text{Bi}_2\text{Dy}_1\text{Fe}_4\text{Ga}_1\text{O}_{12}$  layers is fabricated and characterized. The spectral and temperature dependencies of magnetic circular dichroism (MCD) of these films are studied in the temperature range from 300 K down to 8 K. Measured magneto-optical properties are reported in the spectral range between 300 and 600 nm. In ultrathin garnets at temperatures below 160 K, we found that between 360 and 520 nm, the spectral MCD dependencies were typical of bismuth-substituted garnets with high levels of gallium dilution in the tetrahedral sublattice. The MCD signal strength measured at its 440 nm peak grows linearly with reducing temperature between 160 K and 8 K. This observed temperature dependency of MCD differed dramatically from these measured in thicker (3.7 nm) nanocrystalline garnet films. The peak MCD signal at 440 nm in these 3.7 nm-thick samples grows linearly from 215 K down to 100 K, resembling the same dependency seen in 1.7 nm films. In thinnest layers of thickness 0.6 nm, no MCD signals were observed at any temperature in the range between 8 and 300 K.

## 1. Introduction

In recent years, there has been a significant research interest dedicated to the research fields related to the engineering and characterization of new-generation functional materials, in particular the ultrathin ferrite garnet films of thickness between several nanometers to several tens of nanometers. This is due primarily to the potential advantages of using yttrium-based iron garnets in one of the fast-developing areas of spintronics, which is related to the generation of spin-polarized currents in thin platinum films, assisted by the spin waves generated in yttrium iron garnet (YIG) films of nanoscale thickness [1, 2]. Of particular importance is the fact that this material (YIG) possesses record-low losses in the ultra-high-frequency (UHF)

spectral region, having a very small attenuation parameter  $\alpha \approx 3 \times 10^{-5}$  and ferromagnetic resonance (FMR) linewidth of less than 0.5 Oe (for monocrystalline YIG and LPE-fabricated films) at 9 GHz. Thin films of ferromagnetic metals demonstrate attenuation parameters two orders of magnitude greater compared to those of YIG [3]. It has also been proposed that the use of ultrathin YIG films in spin-valve devices can lead to a significant reduction in the switching currents in these structures [4].

Thin films of bismuth-substituted ferrite garnets are undoubtedly of interest for the design of planar-integrated magneto-optic (MO) devices and also for designing waveguide-based MO modulators, nonreciprocal optical devices, and optical circulators. In planar optical waveguides made using films of bismuth-substituted ferrite garnets of

high MO quality and narrow FMR linewidth, it is possible to achieve MO modulator as well as switching functionality at the working frequencies in the UHF range [5]. Nanocrystalline films of ferrite garnets with small attenuation in the UHF range and high MO quality factors have also been proposed for use in the engineering of new metamaterial types in the gigahertz and optical frequency ranges, as well as for the design of traditional UHF devices, such as band-pass filters utilizing magnetostatic waves [6].

Significant improvements in the MO quality of a range of magnetron-sputtered bismuth-substituted ferrite garnets compared to standard nanocrystalline garnet material have been achieved. Inside these nanocomposite bismuth-substituted ferrite garnet films, quasispherical nanocrystallites of garnets form inside a surrounding material matrix composed mainly of bismuth oxide. In samples of these nanocomposite ferrite garnets, the MO quality of the material (defined as  $Q = 2 \times |\Phi_F|/\alpha$ ) reaches  $50^\circ$  at the wavelength of 633 nm. Here,  $\Phi_F$  is the specific Faraday rotation at the wavelength of interest, and  $\alpha$  is the optical absorption coefficient at the same wavelength.

In another series of composite (YIG +  $\text{Bi}_2\text{O}_3$ ) material synthesis experiments, amorphous-phase films of thickness near 500 nm were deposited, in which the excess volumetric fraction of bismuth oxide was near 20 vol.%. After running the annealing crystallization process, a nanocomposite garnet-type material  $\text{Bi}_{0.5}\text{Y}_{2.5}\text{Fe}_5\text{O}_{12}$  was obtained, in which the X-ray diffraction (XRD) characterization experiments revealed the presence of bismuth-substituted yttrium iron garnet crystallites of average size 36 nm, and the crystal lattice parameter  $a_f(\perp) = 12.450 \text{ \AA}$ . Also, a peak-to-peak FMR linewidth was found to be as low as  $\Delta H_{\text{pp}} = 6.1 \text{ Oe}$  at 9.77 GHz [7]. It is well-known that the substitution of one stoichiometric formula unit of Bi into YIG lattice leads to increasing the material's lattice parameter by  $\Delta a = 0.0829 \text{ \AA}$  [8]. Based on these data, we can conclude that the lattice parameter  $a_f(\perp) = 12.450 \text{ \AA}$  corresponds, in undeformed nanocrystallites, to the composition  $\text{Bi}_{0.5}\text{Y}_{2.5}\text{Fe}_5\text{O}_{12}$ , according to the relationship  $a_f = 12.376 \text{ \AA} + 0.5 \cdot 0.0829 \text{ \AA} = 12.42 \text{ \AA}$ , in which the value of  $12.376 \text{ \AA}$  is the lattice parameter of YIG, and 0.5 is the bismuth substitution coefficient in formula units.

Moving towards depositing ultrathin garnet films of thickness near 10 nm highlights the necessity of undertaking new studies of the fine structure inside the transitional layers existing between the substrate and film materials, since the presence of these layers can change dramatically the magnetic properties of nanoscale films compared to these found in bulk materials or thicker film layers.

It has also been observed that in garnet films grown by LPE, the transitional layers have in fact been composed of two sublayers. The first sublayer of thickness 1–5 nm, which is known as the physical transition layer, represents a physical region of transition in between the substrate and film materials, with its thickness being determined primarily by the quality of substrate polishing [9, 10]. Above this first sublayer of the substrate-to-film transition layer, there exists a technological (epitaxy-related) transition sublayer, the formation of which is due to the special features of the initial

stage of the liquid-phase epitaxy process: the entry of substrate into the solution-melt without rotating the substrate during the first minute, the switch-on of the substrate rotation at 60–100 RPM, and the onset of thermodynamic equilibrium inside the solution-melt lead to the formation of a technological transitional layer of thickness between 5 and 300 nm depending on the value  $\Delta T_s$  of supercooling of the solution-melt. This boundary layer is located near the substrate-film interface (stationary boundary layer), through which the control of the steady-state diffusion of garnet-forming compounds from the bulk of melt-solution occurs towards the growth surface. The thickness of this technological transition layer can vary widely, from a few nanometers (for high growth temperatures in excess of  $900^\circ\text{C}$  and small melt supercooling of  $\Delta T \approx 2\text{--}5^\circ\text{C}$ ) to several hundred nanometers (for growth temperatures near  $700^\circ\text{C}$  and melt supercooling of  $\Delta T \approx 100\text{--}150^\circ\text{C}$  and above [10]). The measurements have shown that under the conditions of high growth temperature and low supercooling  $\Delta T_s$  of the solution-melt, the Curie temperature of a 5 nm-thick epitaxial layer forming between the substrate and the main part of epitaxial layer did not differ from the Curie temperature of the main part of the epitaxial layer. At the same time, the measurements provided on  $1.0 \mu\text{m}$ -thick epitaxial garnet layers of composition  $\text{Bi}_{0.45}\text{Sm}_{0.20}\text{Tm}_{2.35}\text{Fe}_{4.30}\text{Ga}_{0.70}\text{O}_{12}$  demonstrated an initial part of the transitional layer of 100 nm thickness having a  $T_c = 225^\circ\text{C}$ , and in the technological transition layers of thickness 200 nm, we observed a drop in  $T_c$  from  $225^\circ\text{C}$  to  $215^\circ\text{C}$  and a drop in the lattice parameter  $a_f(\perp)$  from  $12.420 \text{ \AA}$  to  $12.411 \text{ \AA}$  for epitaxial films grown at low temperature and at high value of supercooling  $\Delta T_s$  [10].

From the point of view of the practical applications of ultrathin garnet films, the RF magnetron sputtering process is most suitable for depositing amorphous-phase films onto GGG substrates, when followed by high-temperature annealing in air atmosphere at  $550\text{--}650^\circ\text{C}$  (depending on the level of bismuth substitution). The properties of transitional layers existing near the film-substrate interface represent a defining factor, which governs the annealing crystallization process, since the crystallization processes initialize within this transitional region. Bismuth-substituted ferrite garnets also remain the most perspective MO materials for applications in integrated photonics and magneto-plasmonics.

## 2. Sample Fabrication Process

A two-stage sample manufacturing methodology has been used for the preparation of ultrathin iron garnet films. During the first stage, amorphous-phase films of nominal stoichiometry  $\text{Bi}_2\text{Dy}_1\text{Fe}_4\text{Ga}_1\text{O}_{12}$  have been deposited onto GGG substrates using RF magnetron sputtering process. The film thicknesses were 0.6, 1.7, 3.7, 10.3, 50, and 100 nm, calculated based on the measured time durations of the deposition processes, using constant deposition rate approximation and previously obtained calibration data for the deposition rate versus the RF power density. Standard polished- (111) oriented GGG substrates of thickness 0.5 mm were used, heated to  $250^\circ\text{C}$  to improve the film adhesion and

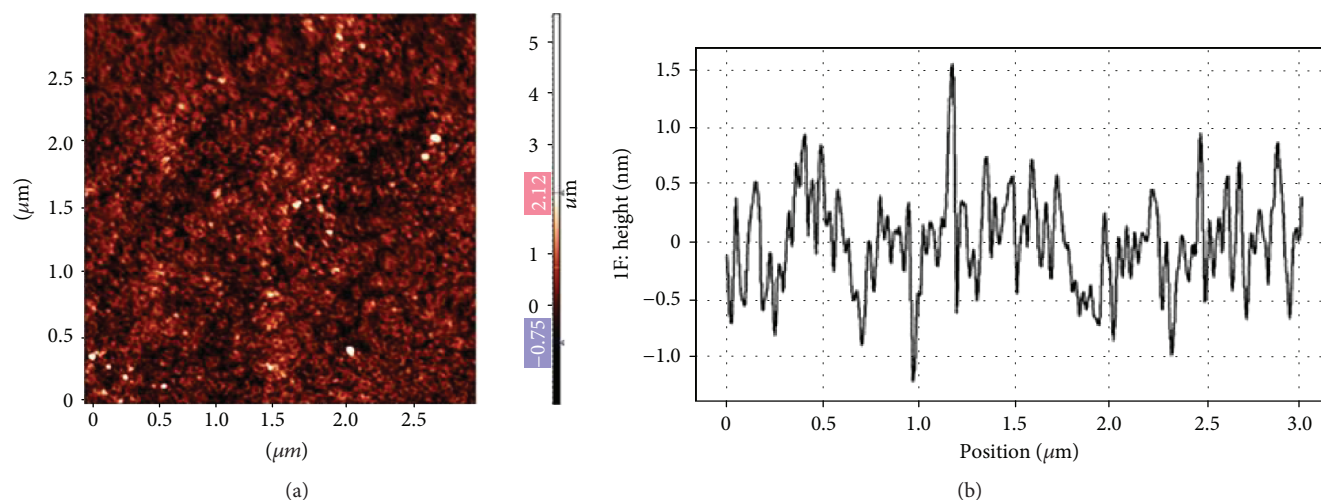


FIGURE 1: (a) GGG substrate surface relief image and (b) profile of GGG substrate-surface relief measured along a scan line across the area ( $3 \mu\text{m} \times 3 \mu\text{m}$ ) shown in (a). A scanning step of 3.7 nm was used; the probe tip radius was less than 30 nm.

density. The sputtering deposition processes were run in pure argon atmosphere at 1 mTorr, at RF power density of  $4 \text{ W}/\text{cm}^2$  at the target surface, which led to a deposition rate close to 4 nm/min. The target-to-substrate distance was 18 cm, and substrate rotation rate was 30 revolutions per minute.

The X-ray diffractometry (XRD) measurements have revealed that all films were amorphous in the phase following the deposition process. We also tested all samples for the presence of any magneto-optic activity using Faraday effect and magnetic circular dichroism measurements in the spectral region between 300 and 800 nm. No signs of magneto-optic activity were detected in any of the amorphous film samples. During the second stage of the sample manufacture process, high-temperature annealing crystallization processes were run in air atmosphere in an electric oven for 1 h, at temperatures ranging between 550 and 650°C. XRD characterization experiments conducted with annealed film samples of thickness 50 nm and 100 nm have revealed the presence of garnet nanocrystallites of average dimensions near 40 nm.

### 3. Microstructural Investigation of Ultrathin Iron Garnet Films

**3.1. Surface Topography Studies.** Figure 1 shows an AFM image revealing the surface relief of the GGG substrate (Figure 1(a)) and the GGG substrate surface relief profile measured along a linear path across the scan of Figure 1(b). When fabricating the ultrathin ferrite garnet films of nominal composition  $\text{Bi}_2\text{Dy}_1\text{Fe}_4\text{Ga}_1\text{O}_{12}$ , we used the substrates with identical polishing quality applicable to both substrate sides, and the data of Figure 1 shows the back side of a substrate having a 1.7 nm-thick film deposited onto its front side. The following scan parameters were used: semicontact mode of scanning, scan area of size  $3 \mu\text{m} \times 3 \mu\text{m}$ , 750 pixels  $\times$  750 pixels (scan step of 4 nm), and using a HA-FM-Pt series cantilever of less than 30 nm nominal tip radius.

An analysis of Figure 1(b) data at high magnification allows obtaining a zoom-in profile of the GGG surface relief,

over a scanning interval from 0.9  $\mu\text{m}$  to 1.3  $\mu\text{m}$ . The obtained data reveals that the substrate surface roughness was rather small and that the surface relief could be characterized by roughness features on a scale near 1 nm. Along a 3  $\mu\text{m}$ -long scan line, we could observe a single 1.6 nm-high columnar feature and a single pit-like feature of depth 1.2 nm (scan line started from the zero height and probe starting position, as shown in Figure 1(b)).

Figure 2(a) shows the surface relief images of an ultrathin (1.7 nm thick) garnet film of nominal composition  $\text{Bi}_2\text{Dy}_1\text{Fe}_4\text{Ga}_1\text{O}_{12}$ , fabricated on the same substrate using RF magnetron sputtering, followed by annealing crystallization process run at 650°C. Figure 2(a) reveals a film surface roughness of around 2 nm and the presence of isolated features of height significantly greater than RMS roughness. Figure 2(b) shows the surface structure details of the same film, obtained from a part of Figure 2(a) scan in the region without any large roughness outliers present. The analysis of data shown in Figure 2(b) reveals, in general, that the film's surface relief is rather similar to that of the GGG substrate. However, a large number of nanocrystallites of height dimensions up to 5 nm were seen, together with a limited number of even larger nanocrystallites. Figure 2(c) shows the surface relief line scan of this 1.7 nm-thick ferrite garnet film, where neither the large nanocrystallites nor the obvious surface contaminants were present within the scanned path.

The analysis of Figure 2(d) shows a somewhat smaller surface roughness in this ferrite garnet film compared to GGG substrate. The data shows that surface relief is represented by small-height (near 0.2 nm) typical roughness features, with base diameter of these features being near 30–50 nm. The height-to-diameter ratio seen in these surface features is near 0.01–0.02, that is, the deposition of the 1.7 nm-thick film did not affect significantly the initial roughness of the GGG substrate surface. We can also note a pit-like structure between 75 and 175 nm of the scan-line coordinates in Figure 2(d). It is possible that the bottom of this feature contained an amorphized surface, or a contaminated surface part, which prohibited the crystallization of the garnet layer.

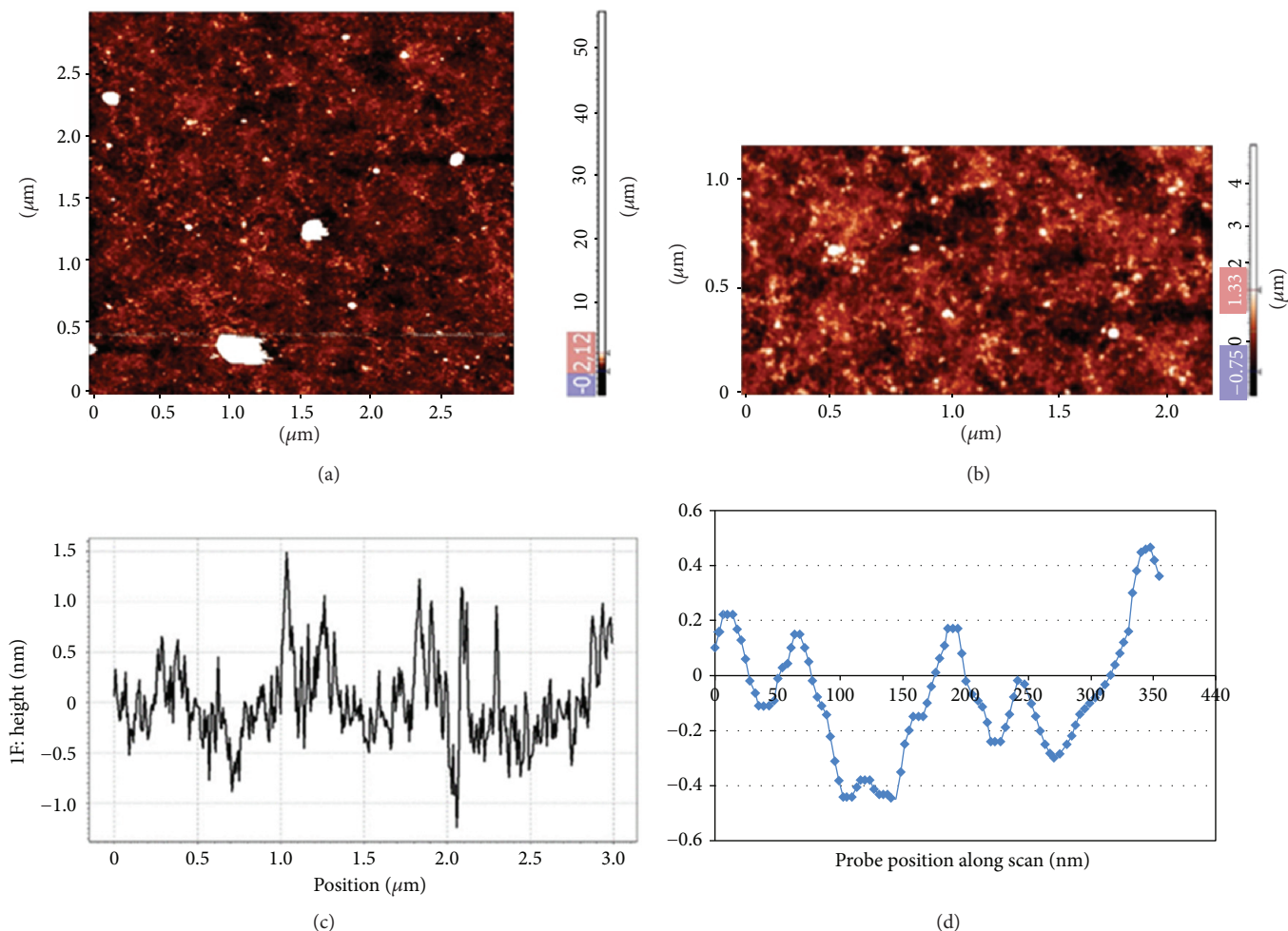


FIGURE 2: (a) AFM surface relief scan of an annealed ultrathin ferrite garnet film of nominal composition  $\text{Bi}_2\text{Dy}_1\text{Fe}_4\text{Ga}_1\text{O}_{12}$  and 1.7 nm thickness, deposited onto a GGG substrate. (b) Partial surface scan data from a flatter part of scan shown in (a). The larger nanocrystallites' height reaches 5 nm. (c) Surface relief profile measured along a scanned line in a garnet film of nominal composition  $\text{Bi}_2\text{Dy}_1\text{Fe}_4\text{Ga}_1\text{O}_{12}$  and 1.7 nm thickness and (d) starting 400 nm-long part of the line scan profile shown in (c).

Of special interest is the nature of larger nanocrystallite features of heights exceeding the nominal film thickness, which can be observed in Figure 2. It is possible that columnar growth morphology was present within some larger nanocrystallite islands which could have appeared due to adatoms merging within the growing ultrathin film. Details of the chemical composition and structure of these growth features within ultrathin garnet films remain to be investigated.

**3.2. X-Ray Diffraction Datasets of Thin Garnet Films of Nominal Composition  $\text{Bi}_2\text{Dy}_1\text{Fe}_4\text{Ga}_1\text{O}_{12}$ .** During the studies of ferrite garnet films of different composition types deposited onto substrates heated to  $300^\circ\text{C}$ , we clearly observed the X-ray diffraction peaks related to the presence of magnetite ( $\text{Fe}_3\text{O}_4$ ). Figure 3 shows XRD datasets for nanocrystalline films of nominal composition  $\text{Bi}_2\text{Dy}_1\text{Fe}_4\text{Ga}_1\text{O}_{12}$  and for several nanocomposite-type films containing up to the estimated 49 vol.% of excess cosputtered bismuth oxide. The crystalline microstructures of the annealed garnet-type thin films were determined by using a detector scan technique (at the near-grazing incidence source angle) using  $\text{CuK}\alpha_1$

radiation and covering the  $2\theta$  diffracted-beam angle range between  $10^\circ$  and  $80^\circ$ . A software-assisted peak listing option was used to determine the precise angular positions of the X-ray diffraction peaks and also to find the full-width half-maximum (FWHM) values for each peak. From these experimental data, we were able to calculate the lattice parameter and the average crystallite size of these garnet thin film materials. It is reasonable to conclude that magnetite nanocrystallites formed already during the sputtering deposition process; this can be confirmed by the presence of  $\text{Fe}_3\text{O}_4$ -related peaks in the XRD signal shown in the bottom trace of Figure 3, which were measured in an amorphous (as-deposited) film on a glass substrate.

At first glance, the presence of  $\text{Fe}_3\text{O}_4$  diffraction peaks in an amorphous-phase as-deposited sample is difficult to understand. However, the formation of magnetite nanocrystallites must have happened during the sputtering deposition process, since the substrate temperature ( $250^\circ\text{C}$ ) was sufficiently high for  $\text{Fe}_3\text{O}_4$  crystallization [11].

It is also possible to assume that during the annealing crystallization process at  $650^\circ\text{C}$ , a partial loss of bismuth

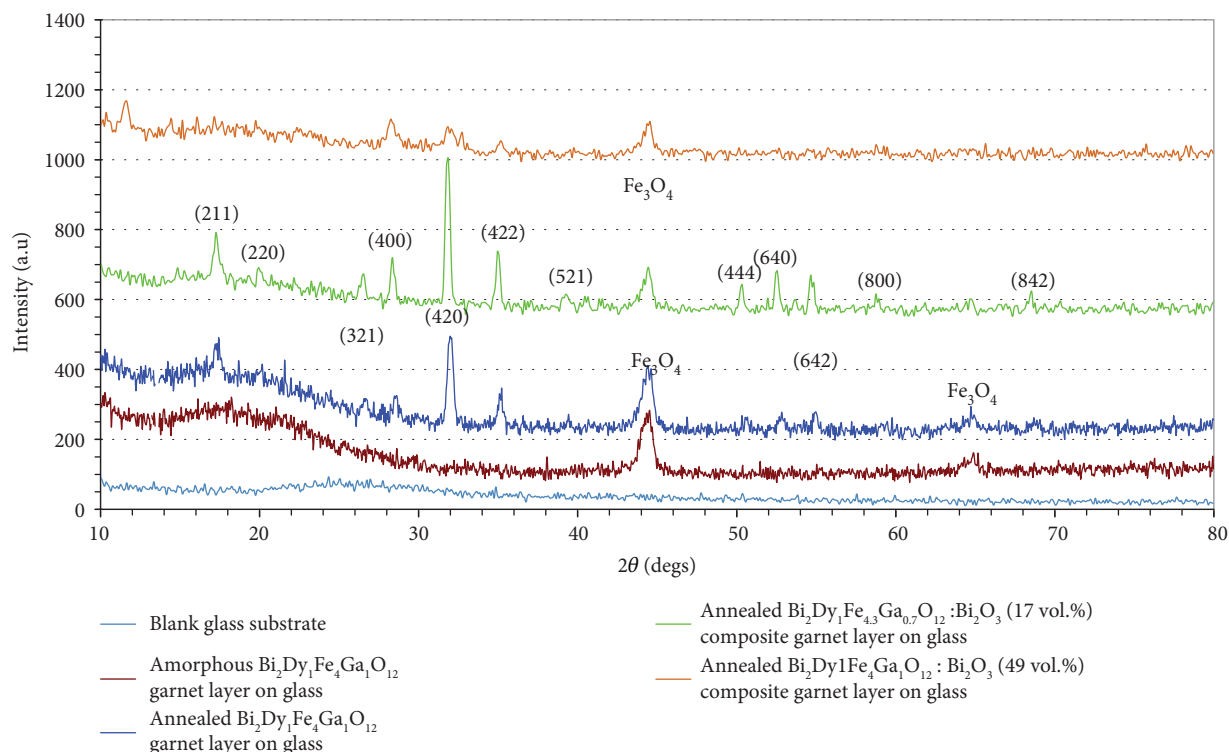


FIGURE 3: XRD datasets obtained from nanocrystalline thin garnet films of nominal composition  $\text{Bi}_2\text{Dy}_1\text{Fe}_4\text{Ga}_1\text{O}_{12}$  and several nanocomposite-type films containing up to 49 vol.% of excess cosputtered bismuth oxide. All films showed diffraction peaks characteristic of  $\text{Fe}_3\text{O}_4$  nanocrystallites.

content occurred. This, in turn, results in the formation of nanocrystallites of the various oxides of iron, for example,  $\text{Fe}_3\text{O}_4$  or  $\text{Fe}_2\text{O}_3$ . It is logical to expect that during the annealing crystallization, when the temperature is rising, starting from  $250^\circ\text{C}$ , the formation of  $\text{Fe}_3\text{O}_4$  nanocrystallites starts. According to the data of Figure 3, the crystallization of the garnet phase in thick (near 450 nm thickness) amorphous films of  $\text{Bi}_2\text{Dy}_1\text{Fe}_4\text{Ga}_1\text{O}_{12}$  is achieved across the film's bulk at  $620^\circ\text{C}$ .

Earlier, when studying the ferrite garnet films of  $\text{Bi}_2\text{Dy}_1\text{Fe}_4\text{Ga}_1\text{O}_{12}$  of thickness near 300 nm, we found that the film was composed of nanocrystallites of characteristic size between 20 and 40 nm, with the average size being 36 nm. Figure 4 shows the nanocrystalline structure of these garnet films. The imaging data were obtained using transmission electron microscopy (TEM). A focused ion beam (FIB) microscope (FEI XP200, FEI Company, Hillsboro, OR 97124, USA) was used to prepare the samples for TEM examination; a thin gold layer was also deposited onto the surface of the garnet sample to improve the imaging contrast. The procedures and the process parameters used to prepare the samples for TEM experiments together with the information on the imaging studies are described in [12].

#### 4. Magnetic Circular Dichroism (MCD) Studies of Ultrathin Iron Garnet Films

4.1. Measurements of MCD Spectra Conducted at Room Temperature. In this section, the results of an experimental

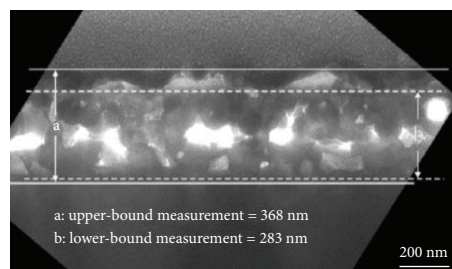


FIGURE 4: Transmission electron microscopy image of a crystallized garnet layer of nominal composition  $\text{Bi}_2\text{Dy}_1\text{Fe}_4\text{Ga}_1\text{O}_{12}$  studied and reported in [12].

study of the spectral dependencies of magnetic circular dichroism (MCD) in the wavelength range between 300 nm and 600 nm are reported, conducted with  $\text{Bi}_2\text{Dy}_1\text{Fe}_4\text{Ga}_1\text{O}_{12}$  iron garnet films of thicknesses 0.6 nm, 1.7 nm, 3.7 nm, 10.3 nm, and 100 nm at room temperature. MCD is a magneto-optic phenomenon manifesting as the difference in the optical absorption coefficients between the left hand and the right hand circularly polarized eigenmode constituents of a linearly polarized light wave.

The results obtained showed that the real morphological structure of the films was represented by the isolated or sometimes ingrown (merged) nanocrystallites forming flat-edged surface bumps of maximum heights not exceeding two or three nominal film thicknesses. The mean diameter of these surface roughness bumps measured at midheight was

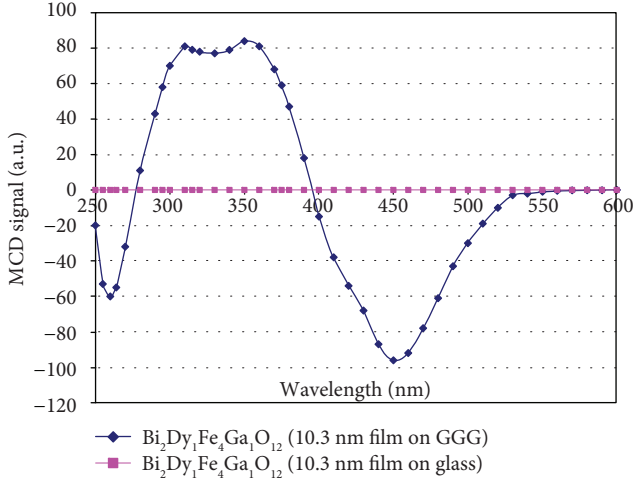


FIGURE 5: Spectral dependency of the MCD signal (blue diamond) measured in a 10.3 nm-thick iron garnet film of nominal composition  $\text{Bi}_2\text{Dy}_1\text{Fe}_4\text{Ga}_1\text{O}_{12}$  grown on a gadolinium gallium garnet (GGG) substrate. Films of the same thickness and composition grown on glass substrates did not show (pink square) any magneto-optical activity. The dichrograph sensitivity scale used was  $5 \times 10^{-6}$ .

near 100 nm, for the 3.7 nm-thick sample. Measurements of MCD spectra were performed using a dichrograph instrument (MARK-III by Jobin-Ivon). All room-temperature measurements were made in the wavelength interval between 300 nm and 800 nm. For films of thicknesses 10.3 nm and 50 nm measured at room temperature, MCD spectral dependencies typical of bismuth-substituted iron garnets of this composition type were seen. The spectral dependency of MCD signal obtained from a 10.3 nm-thick sample is shown in Figure 5.

The negative MCD signal peak at 450 nm and the positive peak at 360 nm are related to the presence of a large concentration of bismuth ions in the structure of ferrite garnet, which affects dramatically the MO properties of bismuth-substituted yttrium iron garnet material in the spectral interval between 330 nm and 2000 nm. It is important to note that the signs of both the Faraday effect and also MCD in the samples studied, across the UV and visible spectral ranges, were the opposite with respect to these measured typically in bismuth-substituted yttrium iron garnets. This can be attributed to the fact that, in bismuth-substituted yttrium iron garnets, the garnet's tetrahedral magnetic sublattice orients magnetically along the externally applied magnetic field, whereas in the samples studied (bismuth-substituted dysprosium gallium iron garnet), the magnetic moment of the octahedral sublattice orients itself along the external magnetic field. This is related to the strong dilution of the tetrahedral magnetic sublattice by nonmagnetic gallium ions and to the presence of a large number of dysprosium ions inside the dodecahedral magnetic sublattice.

At first glance, the spectral dependencies of the Faraday effect and MCD measured over the range from 330 nm to 800 nm are attributed to the fact that the introduction of bismuth into the iron garnet structure leads to the

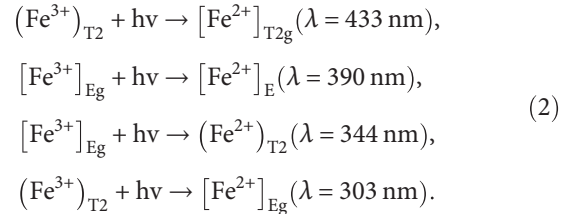
appearance of a magneto-optical peculiarities between 330 and 500 nm. More rigorous analysis has shown that new giant magneto-optical peculiarities near 90 nm in Bi-substituted iron garnets are related to at least four intensive absorption transitions with paramagnetic FR and MCD and to one transition with diamagnetic dispersion FR and MCD [13–20].

In reality, the situation is much more complex. Detailed analysis of the Faraday effect and MCD spectra measured at low temperatures together with the theoretical analysis of the MO properties in yttrium iron garnet leads us to conclude that the two peaks identified (at 450 nm and 360 nm) are in fact related to several optical transitions of both the paramagnetic and the diamagnetic type. These are typically observed in yttrium iron garnets (the transition at  $\lambda = 430$  nm of oscillator strength  $f = 2 \times 10^{-3}$ , the transition at  $\lambda = 390$  nm of oscillator strength  $f = 4 \times 10^{-3}$ , and the transition at  $\lambda = 365$  nm of oscillator strength  $f = 1 \times 10^{-2}$ ) [14–20].

The origins of these strong absorption bands may be related to double excitons [14], that is, the transitions where two  $\text{Fe}^{3+}$  ions within the same sublattice or different sublattices are simultaneously excited to the spin-quartet levels, for example,



Another model of the absorption mechanism for the spectral range below  $\lambda = 450$  nm is based on the assumption that intense absorption bands are related to iron–iron charge-transfer transitions between the octahedral and tetrahedral pairs, for example,



The oscillator strengths of some of the abovementioned optical transitions grow by about two orders in magnitude, when bismuth ions are introduced into the structure of iron garnet, up to the substitution level of three formula units. It should be noted here that films of the same thickness and composition grown on glass substrates did not show any magneto-optical activity in the entire spectral region.

The observed negative sign of the MCD effect near 450 nm reveals that in this thin film garnet material, the octahedral magnetic sublattice was orienting itself in the direction of the magnetic field applied externally, that is, the film investigated had a so-called compensation point at above the room temperature. At the optimum measurement conditions, the dichrograph registers reliably a signal of magnitude 5 (a.u.). Realistically, 5 a.u. of signal strength corresponds to 5 mm of space on the data curve recorded at the maximum sensitivity settings. Adjusting for the sample thickness 10.3 nm, we get  $480 \cdot 10^{-6}$  (a.u.) divided by 10.3 nm or 48 (a.u.)/(1 nm) in arbitrary units per nanometer of sample

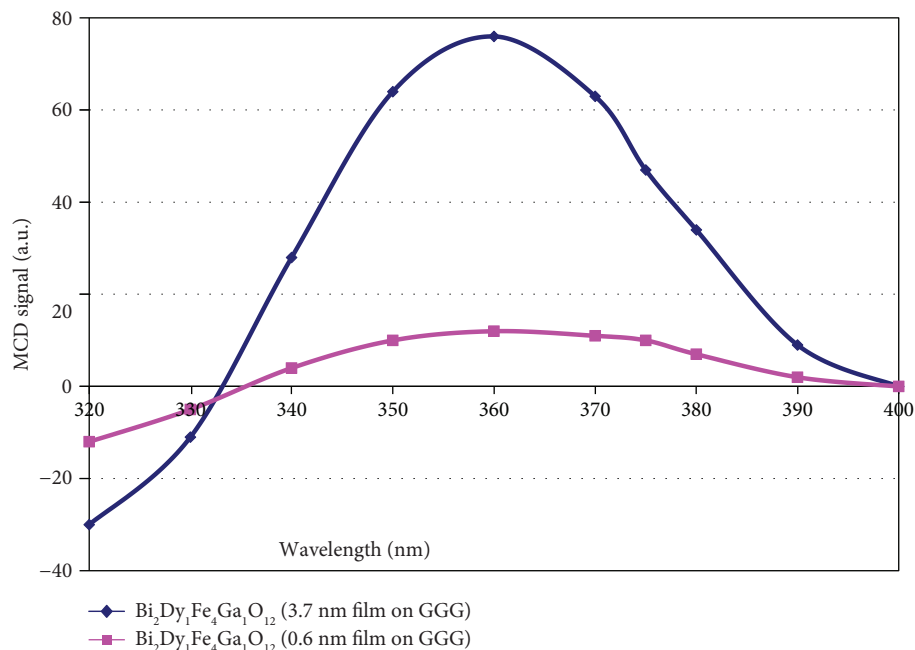


FIGURE 6: Room-temperature MCD spectra measured in films of thicknesses 0.6 nm (pink square) and 3.7 nm (blue diamond) deposited onto GGG substrates. Dichrograph sensitivity scale used was  $2 \times 10^{-6}$ .

thickness. A series of prior publications have shown that transitional garnet layers of 4–5 nm thickness did not possess magneto-optic activity at room temperature. Accounting for this thickness correction, the strength of MCD signal per unit (1 nm) of sample thickness will be twice higher for a 10.3 nm-thick sample. We can also conclude from the results obtained that, for the MO material under study, during the measurements of MCD at 450 nm wavelength, the dichrograph can register reliably the signal from film samples as thin as only 1 Å, if the film possesses magnetic ordering of iron ions. The only problem is the presence of magnetic ordering in bismuth-containing ferrite garnet films at the room temperature or at helium temperature.

The observed signs of MCD effect within different spectral regions point to the fact that in this thin film garnet material, the octahedral magnetic sublattice was orienting itself in the direction of the magnetic field applied externally. The measurements of the MCD spectra made at room temperature with film samples of thicknesses 0.6, 1.7, and 3.7 nm deposited onto GGG substrates did not exhibit the typical MCD spectra features characteristic of bismuth-substituted iron garnets. At the same time, near the signal-detection limits of dichrograph's sensitivity, it was possible to identify the presence of some very weak magneto-optic activity in the spectral interval between 300 nm and 400 nm. These measured spectral dependencies are shown in Figure 6.

The maximum MCD signal value at 360 nm reached 24 a.u. for the 0.6 nm-thick sample and 152 a.u. for the 3.7 nm-thick sample, at the sensitivity scale of  $1 \times 10^{-6}$ . The observed MCD signals may be attributed to the presence of magnetite nanocrystallites, which form as a result of bismuth ion losses occurring during the deposition process and during the subsequent high-temperature annealing of ultrathin films.

**4.2. Measurements of MCD Spectra Conducted at Low Temperatures.** In order to obtain additional information on the properties of ultrathin ferrite garnet films and to study the structure of any transition layers existing near the substrate-film boundary, as well as the compositional changes of films occurring with increasing thickness, we performed low-temperature spectral MCD measurements between 300 K and 8 K, for films of thicknesses 0.6, 1.7, and 3.7 nm. Measurement results are shown in Figures 7 and 8. The results of our present study reveal that even in films as thin as these, no complete loss of bismuth content occurs after annealing the layers at 650°C.

The maximum MCD signal value measured in this sample at 440 nm reached 890 a.u. at the  $1 \cdot 10^{-6}$  sensitivity scale. The presence of two MCD signal bands with extreme at 440 nm and 390 nm is characteristic of ferrite garnet films with high levels of gallium ion substitution within the iron ion sites of the tetrahedral sublattice of garnet. In this case, it can be expected that dilution of the tetrahedral lattice sites by gallium ions occurs, with these gallium ions supplied from the substrate composed of gadolinium gallium garnet. The spectral position of the first (long-wavelength) intense MCD signal peak near 440 nm is characteristic of bismuth-substituted iron garnets of lattice parameter close to  $a_f = 12.383 \text{ \AA}$ . With increasing bismuth substitution in a garnet structure, a red-shifting effect occurs for this MCD signal band, which in the films studied in the present work is near 440 nm. For iron garnets of composition  $\text{Bi}_{2.8}\text{Y}_{0.2}\text{Fe}_5\text{O}_{12}$ , the long-wave MCD peak is shifted towards 490 nm [21]. The spectral position of this MCD peak remains at 490 nm for all films of thickness between 15 and 160 nm.

The measured MCD spectra of the 1.7 nm-thick sample for different temperatures over the range 8 K to 200 K are

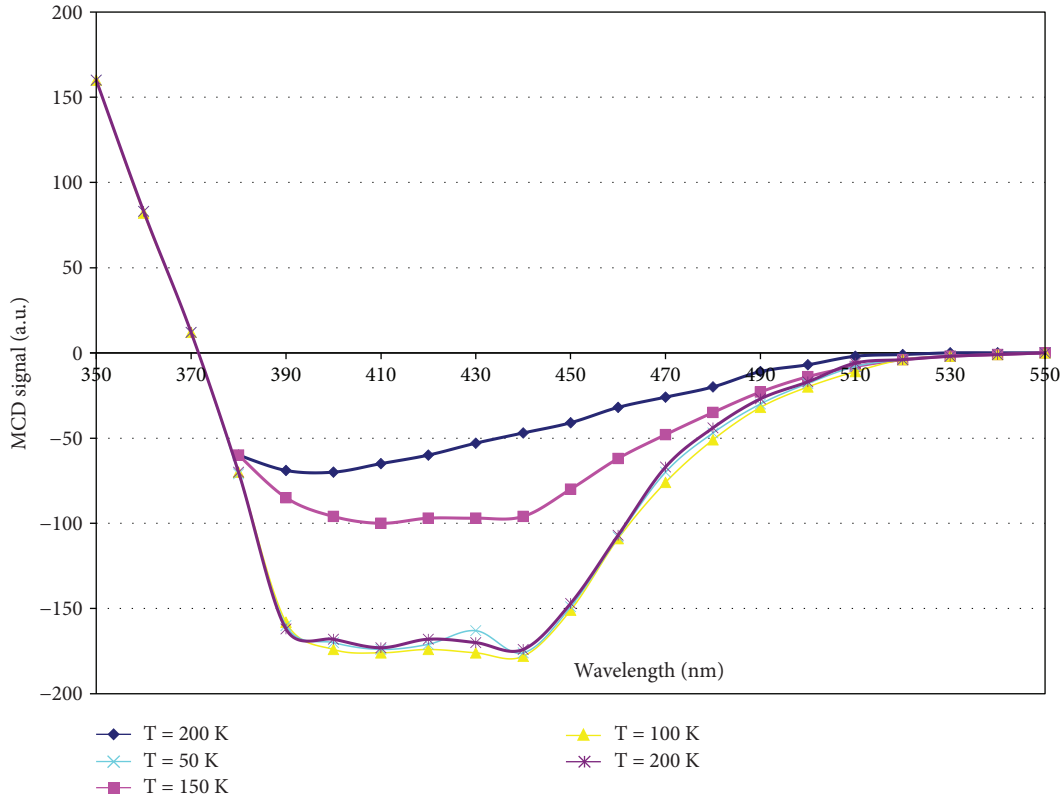


FIGURE 7: Spectral MCD signal dependencies measured in a 3.7 nm-thick sample of nominal composition  $\text{Bi}_2\text{Dy}_1\text{Fe}_4\text{Ga}_1\text{O}_{12}$  at different sample temperatures between 200 K and 8 K. (1) 200 K, (2) 150 K, (3) 100 K, (4) 50 K, (5) 8 K. Dichrograph sensitivity scale was  $5 \times 10^{-6}$ .

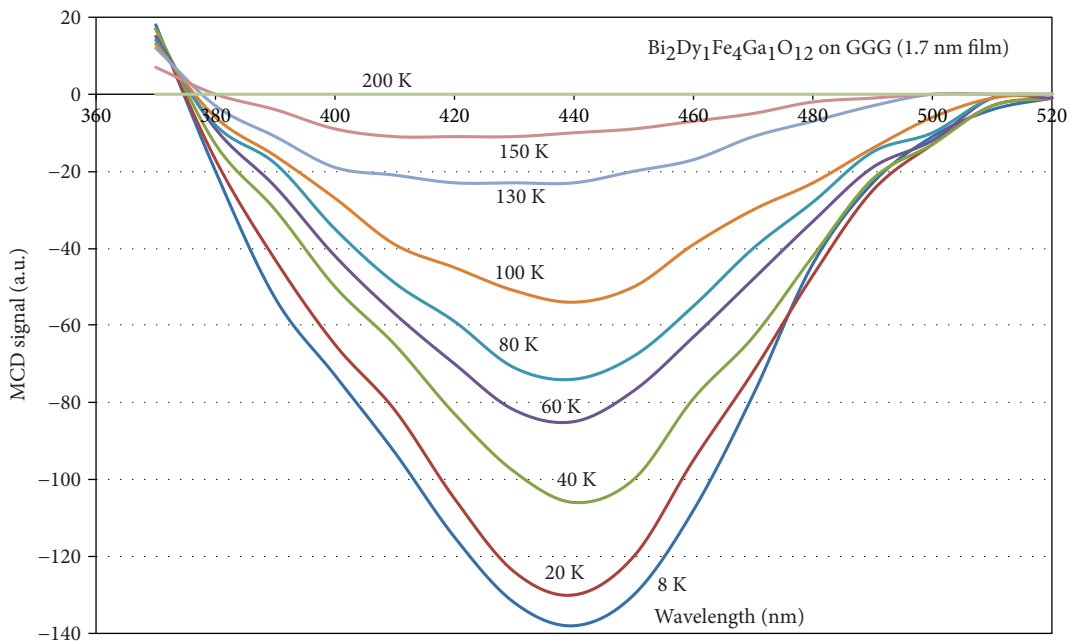


FIGURE 8: MCD spectral dependencies measured in a 1.7 nm-thick sample of iron garnet film between 200 K and 8 K (the signal was also at zero level at 300 K). The sensitivity of dichrograph scale was  $2 \times 10^{-6}$ .

shown in Figure 8. The signal strength at the peak of the MCD band at 440 nm reached 278 a.u. at sensitivity scale  $1 \times 10^{-6}$ . For the 3.7 nm-thick sample, the main difference

in MCD spectra was the significant reduction in the MCD strength over the 400 nm signal band compared to the reduction in the 440 nm band. As was already noted, the

negative sign of MCD signal in the spectral interval between 370 nm and 550 nm and the observed shapes of spectral dependencies at temperatures between 150 K and 8 K (MCD peak locations near 445 and 400 nm) are characteristic of bismuth-substituted iron garnets in which the iron sites within the tetrahedral sublattice are diluted heavily with  $\text{Ga}^{3+}$  ions. The fact that in the samples studied the MCD signal was negative between 375 nm and 550 nm confirms that the magnetic moment of the octahedral sublattice of garnet is oriented along the direction of the external magnetic field.

At the same time, a different explanation is required for the spectral MCD dependency observed at 200 K. The broad peak near 400 nm could be related to magnetite ( $\text{Fe}_3\text{O}_4$ ) nanocrystallites [11]. It is important to note that the shape of the MCD spectra observed at 150 K and at lower temperatures is characteristic of bismuth-substituted iron garnets. The location of the first MCD peak near 440 nm also points to the fact that the lattice parameter within the nanocrystallites of the films studied was near 12.383 Å. The available data allows the estimation of the lattice parameter within the quasi-2D nanocrystallites present within this 3.7 nm-thick film. Proposing that the blocked state temperature  $T_B = 215$  K is close to the Neel temperature, we can expect based on the literature data that the real composition of ferrite garnet nanocrystallites differs significantly from the nominal composition  $\text{Bi}_2\text{Dy}_1\text{Fe}_4\text{Ga}_1\text{O}_{12}$ . Neel temperature near 215 K in gallium-diluted iron garnets corresponds to the substitution level of the iron ions by the gallium ions close to 3 formula units [22].

At a nominal thickness of 3.7 nm in this iron garnet film, considering also the presence of an intermediate “dead layer” of a few nanometer thickness near the GGG substrate interface, the hypothesized high substitution of the iron ions by gallium within tetrahedral lattice sites appears quite likely. This can be explained as follows: during the initial stages of garnet film deposition, amorphization of substrate occurs during  $\text{Ar}^+$  ion bombardment, to depths between 1 and 2 nm. During the annealing process, as a result of accelerated diffusion within this region, there occurs some compositional equalization of the film’s contents within the amorphization region, and  $\text{Ga}^{3+}$  ion content reaches 2.5 formula units within this sublayer. This model is supported by the results of the MO property studies in ultrathin ferrite garnet films of nominal composition  $\text{Bi}_{2.8}\text{Y}_{0.2}\text{Fe}_5\text{O}_{12}$  and by the fine structure in transitional layers between the substrate and film which is observed in these films [21].

By varying the bismuth and dysprosium contents, based on the available data, we can estimate the actual composition of the film’s material. For the film of composition  $\text{Bi}_{0.4}\text{Dy}_{2.6}\text{Fe}_2\text{Ga}_3\text{O}_{12}$ , the calculated lattice parameter value is

$$a_f(\text{Å}) = 12,376(\text{Å}) + 0.4 * 0.0828(\text{Å}) + 2.6 * 0.0097(\text{Å}) - 3 * 0.0170(\text{Å}) = 12.383(\text{Å}). \quad (3)$$

Here, 12.376 Å is the lattice parameter of an iron garnet material of composition  $\text{Y}_3\text{Fe}_5\text{O}_{12}$ ,  $0.4 * 0.0828(\text{Å})$  is the

change in the lattice parameter occurring due to introduction of a 0.4 formula unit of the  $\text{Bi}^{3+}$  ion substitution into garnet structure,  $2.6 * 0.0097(\text{Å})$  is the corresponding lattice parameter change due to introducing 2.6 formula units of  $\text{Dy}^{3+}$  ion, and  $3 * 0.0170(\text{Å})$  corresponds to the effect of  $\text{Ga}^{3+}$  ion dilution at 3 formula units. The coefficients used in the above calculation are taken from [22]. Here, it is important to note that the spectral location of the long-wavelength peak in MCD spectra of bismuth-substituted ferrite garnets containing from 0.1 to 1.0 formula units of bismuth substitution is observed to be near 440 nm, provided that the film’s lattice parameter coincides with the substrate’s lattice parameter of GGG, which equals to  $a_s = 12.383 \text{ Å}$ .

Another unusual result follows from the practically unchanging values of MCD signal when the sample temperature was varied between 100 K and 8 K. Based on the analysis of the data shown in Figure 1(b), we can propose that Neel temperature of nanocrystalline ferrite garnet film of thickness 3.7 nm is near 215 K, if extrapolating the horizontal section of the temperature dependency graph of MCD between 100 K and 8 K using a standard temperature dependency of the specific Faraday effect, as obtained from bulk garnet samples. We can also expect that, accounting for all of the above factors, the actual composition of nanocrystallites present inside the film of 3.7 nm thickness, also accounting for our estimated temperature of magnetic ordering and the location of the first MCD peak of bismuth-substituted iron garnet near 440 nm, has the following chemistry— $\text{Bi}_1\text{Dy}_2\text{Fe}_{2.5}\text{Ga}_{2.5}\text{O}_{12}$ . From the coincident curve shapes in MCD curves measured at 100, 50, and 8 K, it follows that the fraction of the film’s volume which contributes to the MCD signal at 100 K and below has a constant chemical composition, and its Neel temperature is near 150 K.

#### 4.3. Temperature Dependencies of MCD Signals at 440 nm.

The most interesting result is found when analyzing the temperature dependency of the MCD signal strength near the region of 440 nm peak for film samples of thicknesses 3.7 nm and 1.7 nm. Figures 9 and 10 show the temperature dependency of MCD signal strength at 440 nm for 3.7 nm and 1.7 nm-thick film samples.

For the analysis of measured data, it makes sense to split the curve shown in Figure 5 into two temperature intervals. The first interval is between 8 K and 100 K. Within this temperature region, the MCD signal strength at 440 nm is practically unchanged (in reality, it is reduced by 1.5% with the temperature decreasing from 100 K to 8 K). A reduction in MCD signal within this exact interval has been observed previously (but notably to a much greater extent in the MCD signal strength reduction) in epitaxial-quality films of bismuth-substituted iron garnets grown by LPE [23]. The explanation for this effect, based on the molecular field theory, is given in 23, where a good agreement was reported between the theory predictions and experimental data.

At higher temperatures, in between 100 K and 215 K, linear reduction in the strength of MCD signal is observed.

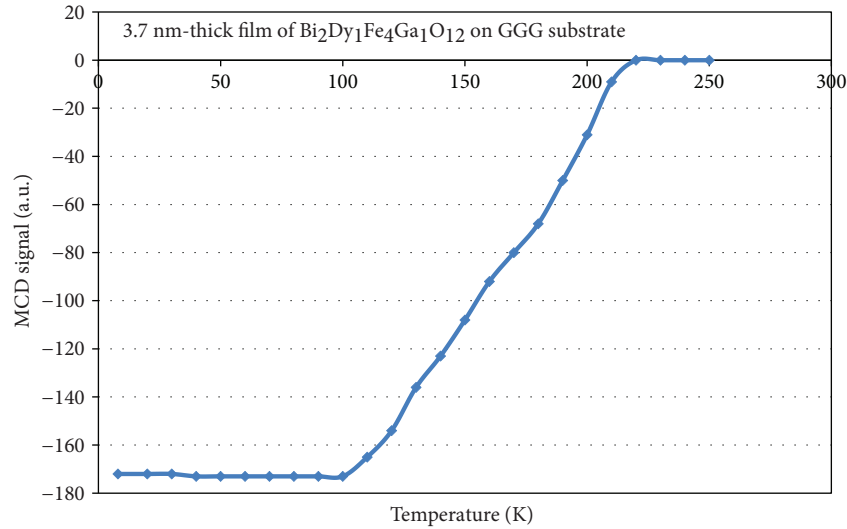


FIGURE 9: Temperature dependency of MCD signal strength near 440 nm peak measured in 3.7 nm-thick garnet sample. Dichrograph sensitivity scale was  $5 \times 10^{-6}$ .

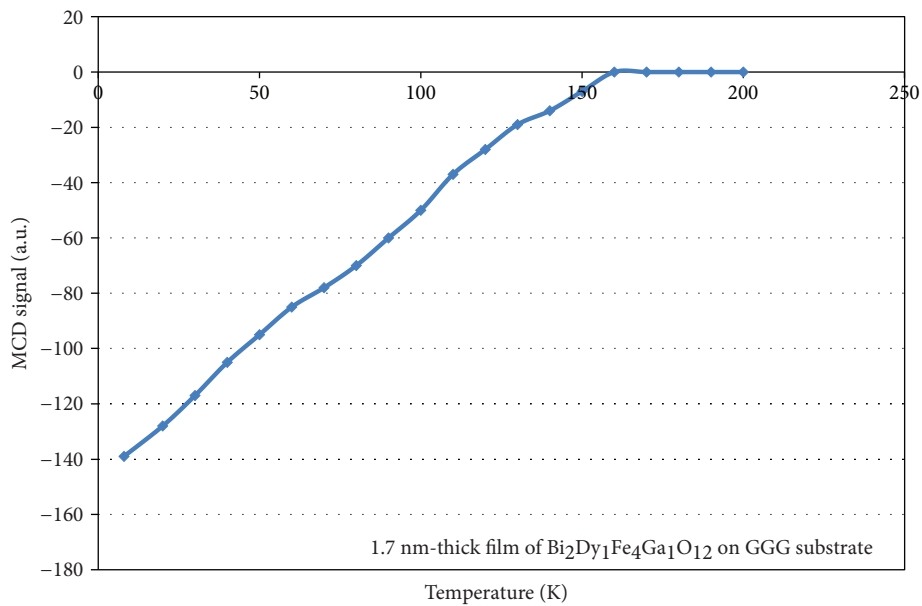


FIGURE 10: Temperature dependency of the MCD signal near 440 nm peak for 1.7 nm-thick film. Dichrograph sensitivity scale was  $1 \times 10^{-6}$ .

This region of temperature dependency points to a superparamagnetic behaviour of the object of study, with the blocking temperature being near 215 K. The appearance of a superparamagnetic region can be explained as follows: for a film of nominal thickness 3.7 nm, one can expect the appearance of quasi-2D nanocrystallite islands during the annealing crystallization process. These islands will be similar in their appearance to very flat bumps on the substrate surface. The studies of surface morphology made with thin garnet films of nominal composition  $\text{Bi}_{2.8}\text{Y}_{0.2}\text{Fe}_5\text{O}_{12}$  and thickness between 4 nm and 100 nm using scanning probe microscopy revealed that for a film thickness around 5 nm, flat bumps appear on the film surface, the heights of which exceed the nominal film thickness by several times [21].

Based on the magnitude of the MO effects observed, one can conclude that for a nominal film thickness greater than 12 nm, the film had a constant composition  $\text{Bi}_{2.8}\text{Y}_{0.2}\text{Fe}_5\text{O}_{12}$  throughout the thickness interval from about 12 nm up to its top-surface boundary. In [21], the maximum film thickness studied was 100 nm and the minimum 2.9 nm. Besides, no anomalies were observed with decreasing temperature, down to the material's Neel temperature. Therefore, it is possible to assume that the volume regions in between any larger-size nanocrystallites were filled with smaller ones. The mutual ingrowth between nanocrystallites enabled significant exchange coupling between all structural elements within the films. For the 3.7 nm-thick film sample studied in the present work, the nanocrystallite edges overlapped,

and for the thickness of the magnetic layer near the regions of overlap between neighboring quasi-2D nanocrystallites being around several nanometers, at low temperatures, all nanocrystallites together behaved as quasibulk material. At high temperatures, the system of nanocrystallites of larger size typically exhibits a superparamagnetic state.

The measured temperature dependency is essentially represented by a straight line, and through data extrapolation, the calculated blocking temperature is around 160 K. We believe that for this 1.7 nm-thick film sample, the results obtained can be interpreted as follows: a 1.7 nm-thick (ultrathin) sample comprises an ensemble of quasi-2D nanocrystallites (very flat surface bumps of 3–5 nm height and width at base between 10 and 100 nm), between the boundaries of which the exchange interaction is absent. As a result of this, the sample demonstrated superparamagnetic behaviour over the entire temperature interval. Since the thermal expansion coefficients of bismuth-substituted iron garnets exceed those of GGG substrate by about 10% and since the annealing processes are run at 650°C, at room temperature the nanocrystallites typically experience the state of an in-plane tensile stretching, hence possessing uniaxial magnetic anisotropy with a positive constant of uniaxial magnetic anisotropy. Because of the low-saturated magnetization in iron garnets of this composition type, the uniaxial magnetic anisotropy condition  $K_u > 2\pi M_s^2$  will be satisfied.

## 5. Conclusions

Studies of the magneto-optic properties of ultrathin bismuth-substituted iron garnet films have been performed for the first time for films of nominal thicknesses 0.6, 1.7, and 3.7 nm. The film samples have been prepared on gadolinium gallium garnet substrates by RF magnetron sputtering followed by annealing crystallization at 650°C. At room temperature, the spectral dependencies of magnetic circular dichroism have been measured in the spectral interval between 250 nm and 850 nm. At cryogenic temperatures down to 8 K, MCD dependencies have been measured between 300 nm and 850 nm. At room temperature in samples of thickness exceeding 5 nm, the MCD spectra typical of bismuth-substituted iron garnets have been measured. For ultrathin films of thicknesses 0.6, 1.7, and 3.7 nm, no magneto-optic effects linked to the presence of bismuth-substituted iron garnet nanocrystallites have been observed at room temperature. Experimental results have shown that, at temperatures below 160 K, for a film of 1.7 nm thickness, the observed MCD spectrum is mainly due to the presence of  $\text{Bi}_1\text{Dy}_2\text{Fe}_{2.5}\text{Ga}_{2.5}\text{O}_{12}$  nanocrystallites, whereas over the temperature range between 100 K and 8 K, the magneto-optic activity typical of  $\text{Bi}_1\text{Dy}_2\text{Fe}_{2.5}\text{Ga}_{2.5}\text{O}_{12}$  nanocrystallites is dominant. The gallium ion content has been estimated, based on the Neel temperature estimation. The bismuth substitution levels have been estimated based on the magnitudes of the specific MCD signal strength obtained from the measurements. Here, it is important to note that the theoretically calculated lattice parameter for a film of a given composition was  $a_f = 12.390 \text{ \AA}$ , which is very close to the GGG substrate lattice parameter ( $12.383 \text{ \AA}$ ).

## Conflicts of Interest

The authors declare no conflict of interest.

## Authors' Contributions

The Australian team (M. Nur-E-Alam, M. Vasiliev, and K. Alameh) fabricated the ultrathin film batches and provided their optical and also the X-ray diffractometry characterization; the Russian teams have provided a comprehensive scanning probe microscopy analyses and low-temperature characterization of the magnetic and MO properties. All authors construed to the analysis of the data and the write-up of the final manuscript.

## Acknowledgments

The samples of ferrite garnet films were fabricated by Edith Cowan University (Perth, Australia); the studies of their optical, magnetic, and magneto-optical properties (including low-temperature measurements) have been conducted by the V.A. Kotelnikov Institute of Radio Technology and Electronics of the Russian Academy of Sciences and at the Moscow Institute of Physics and Technology (MIPT), supported by grant from the Russian Science Foundation (Project code 14-22-00279). AFM measurements were conducted at MIPT (Moscow), supported by Russian Foundation for Basic Research grants 16-07-00734 and 16-07-00735.

## References

- [1] Y. Kajiwar, K. Harii, S. Takahashi et al., "Transmission of electrical signals by spin-wave interconversion in a magnetic insulator," *Nature*, vol. 464, no. 7286, pp. 262–266, 2010.
- [2] H. Kurebayashi, O. Dzyapko, V. E. Demidov, D. Fang, A. J. Ferguson, and S. O. Demokritov, "Controlled enhancement of spin-current emission by three-magnon splitting," *Nature Materials*, vol. 10, no. 9, pp. 660–664, 2011.
- [3] H. Wang, Y. Li, L. Sun et al., "Electrospun novel bifunctional magnetic-photoluminescent nanofibers based on  $\text{Fe}_2\text{O}_3$  nanoparticles and europium complex," *Journal of Colloid and Interface Science*, vol. 350, no. 2, pp. 396–401, 2010.
- [4] A. Brataas, A. D. Kent, and H. Ohno, "Current-induced torques in magnetic materials," *Nature Materials*, vol. 11, no. 5, pp. 372–381, 2012.
- [5] H. Dötsch, N. Bahlmann, O. Zhuromskyy et al., "Applications of magneto-optical waveguides in integrated optics: review," *Journal of the Optical Society of America B*, vol. 22, no. 1, pp. 240–253, 2005.
- [6] S. A. Manuilov, R. Fors, S. I. Khartsev, and A. M. Grishin, "Submicron  $\text{Y}_3\text{Fe}_5\text{O}_{12}$  film magnetostatic wave band pass filters," *Journal of Applied Physics*, vol. 105, no. 3, article 033917, 2009.
- [7] M. Nur-E-Alam, M. Vasiliev, K. Alameh, V. Kotov, V. Demidov, and D. Balabanov, "YIG:  $\text{Bi}_2\text{O}_3$  nanocomposite thin films for magneto-optic and microwave applications," *Journal of Nanomaterials*, vol. 2015, Article ID 182691, 6 pages, 2015.
- [8] S. Geller, H. J. Williams, G. P. Espinosa, R. C. Sherwood, and M. A. Gilleo, "Reduction of the preparation temperature of

- polycrystalline garnets by bismuth substitution,” *Applied Physics Letters*, vol. 3, no. 2, pp. 21-22, 1963.
- [9] Y. Sun, Y. Y. Song, H. Chang et al., “Growth and ferromagnetic resonance properties of nanometer-thick yttrium iron garnet films,” *Applied Physics Letters*, vol. 101, no. 15, article 152405, 2012.
- [10] V. A. Kotov, D. E. Balabanov, S. M. Grigorovich, V. I. Kozlov, and V. K. Nevolin, “Magnetic and magneto-optical properties of the transition layer in epitaxial bismuth-gallium iron garnet structures,” *Soviet Physics: Technical Physics*, vol. 31, pp. 544-548, 1986, [*J. Techn. Phys.* 56 (5), 897-903 (1986) (in Russian)].
- [11] S. Kale, S. M. Bhagat, S. E. Lofland et al., “Film thickness and temperature dependence of the magnetic properties of pulsed-laser-deposited  $\text{Fe}_3\text{O}_4$  films on different substrates,” *Physical Review B*, vol. 64, no. 20, 2001.
- [12] P. C. Wo, P. R. Munroe, M. Vasiliev, Z. H. Xie, K. Alameh, and V. Kotov, “A novel technique for microstructure characterization of garnet films,” *Optical Materials*, vol. 32, no. 2, pp. 315-322, 2009.
- [13] J. Suits, “Faraday and Kerr effects in magnetic compounds,” *IEEE Transactions on Magnetics*, vol. 8, no. 1, pp. 95-105, 1972.
- [14] G. B. Scott, D. E. Lacklison, and J. L. Page, “Absorption spectra of  $\text{Y}_3\text{Fe}_5\text{O}_{12}$  (YIG) and  $\text{Y}_3\text{Ga}_5\text{O}_{12}:\text{Fe}^{3+}$ ,” *Physical Review B*, vol. 10, no. 3, pp. 971-986, 1974.
- [15] K. W. Blazey, “Wavelength-modulated spectra of some  $\text{Fe}^{3+}$  oxides,” *Journal of Applied Physics*, vol. 45, no. 5, pp. 2273-2280, 1974.
- [16] S. Wittekoek, T. J. A. Popma, J. M. Robertson, and P. F. Bongers, “Magneto-optic spectra and the dielectric tensor elements of bismuth-substituted iron garnets at photon energies between 2.2-5.2 eV,” *Physical Review B*, vol. 12, no. 7, pp. 2777-2788, 1975.
- [17] G. B. Scott and J. L. Page, “Pb valence in iron garnets,” *Journal of Applied Physics*, vol. 48, no. 3, pp. 1342-1349, 1977.
- [18] G. B. Scott and J. L. Page, “The absorption spectra of  $\text{Y}_3\text{Fe}_5\text{O}_{12}$  and  $\text{Y}_3\text{Ga}_5\text{O}_{12}:\text{Fe}^{3+}$  to 5.5 eV,” *Physica Status Solidi*, vol. 79, no. 1, pp. 203-213, 1977.
- [19] A. V. Zenkov and A. S. Moskvina, “Bismuth-induced increase of the magneto-optical effects in iron garnets: a theoretical analysis,” *Journal of Physics: Condensed Matter*, vol. 14, pp. 6957-6968, 2002.
- [20] A. K. Zvezdin and V. A. Kotov, *Modern Magneto-optics and Magneto-optical Materials*, Institute of Physics Publishing, Bristol, UK, 1997.
- [21] A. N. Shaposhnikov, A. R. Prokopov, A. V. Karavainikov et al., “Modification of Bi: YIG film properties by substrate surface ion pre-treatment,” *Materials Research Bulletin*, vol. 55, pp. 19-25, 2014.
- [22] A. H. Eschenfelder, *Magnetic Bubble Technology*, Springer-Verlag, New York, NY, USA, 1981.
- [23] P. Hansen and J. P. Krumme, “Magnetic and magneto-optical properties of garnet films,” *Thin Solid Films*, vol. 114, no. 1-2, pp. 69-107, 1984.

## Research Article

# Overcoming Multidrug Resistance by On-Demand Intracellular Release of Doxorubicin and Verapamil

Jianwei Jiang <sup>1</sup>, Shaojuan Liu,<sup>2</sup> Chunlei Wang,<sup>1</sup> and Hongyan Zhang <sup>1</sup>

<sup>1</sup>Zhejiang Cancer Hospital, Hangzhou 310022, China

<sup>2</sup>The Third People's Hospital of Hangzhou, Hangzhou 310009, China

Correspondence should be addressed to Jianwei Jiang; [jiangjw@zjcc.org.cn](mailto:jiangjw@zjcc.org.cn)

Received 10 October 2017; Revised 2 January 2018; Accepted 29 April 2018; Published 31 May 2018

Academic Editor: Sabu Thomas

Copyright © 2018 Jianwei Jiang et al. This is an open access article distributed under the Creative Commons Attribution License, which permits unrestricted use, distribution, and reproduction in any medium, provided the original work is properly cited.

Multidrug resistance (MDR) is one of the major obstacles to the successful application of cancer chemotherapy. Herein, we developed light-responsive doxorubicin-and-verapamil-coencapsulated gold liposomes to overcome MDR. Upon ns-pulsed laser irradiation, the highly confined thermal effect increased the permeability of the phospholipid bilayer, triggering the release of doxorubicin and verapamil, leading to high concentrations in cells. Free verapamil efficiently inhibited the membrane multidrug resistance proteins (MRPs), while the high concentration of doxorubicin saturated MRPs, thus overcoming MDR. We showed that nanosecond- (ns-) pulsed laser- (532 nm, 6 ns) induced doxorubicin release from gold liposomes depended on laser fluence and pulse number. More than 58% of the doxorubicin was released with a 10-pulse irradiation (100 mJ/cm<sup>2</sup>). Furthermore, ns laser pulses also liberated doxorubicin from endocytosed gold liposomes into the cytosol in MDA-MB-231-R cancer cells. The cytotoxicity of doxorubicin coencapsulated with verapamil was significantly enhanced upon laser irradiation. This study suggested that light-triggered on-demand release of chemotherapeutic agents and MRP inhibitors could be used advantageously to overcome multidrug resistance.

## 1. Introduction

Cancer metastasis is one of the main challenges in cancer therapy, which leads to over 90% of cancer-related deaths [1]. To date, although there are several therapies for cancer metastasis treatment, for example, aggressive surgery, radiotherapy, and chemotherapy, only very limited curative effects in patients have been observed [2]. Chemotherapy is by far the most commonly used cancer treatment. Nanoparticles have successfully been used to carry chemotherapeutic agents and to enable other functions, such as long blood circulation and tumor targeting [3]. The encapsulation of toxic chemotherapeutic agents may reduce their nonspecific toxicity, but meanwhile limits drug release in the tumor sites. Enhancing drug release from endocytosed nanoparticles is of great significance since chemotherapeutic agents have to be released into the cytosol or nucleus to elicit their therapeutic effects. In recent years, controlled drug release has attracted increasing interests. Many controlled drug-release strategies have been reported, especially, the diffusion-based and

biologically-activated drug-release system. However, drug release based on these mechanisms are usually slow, cannot be precisely controlled, and do not amplify the selectivity of drug delivery [4]. Strategies that enable fast drug release upon activation is still highly desired to enhance intracellular cancer drug delivery [5].

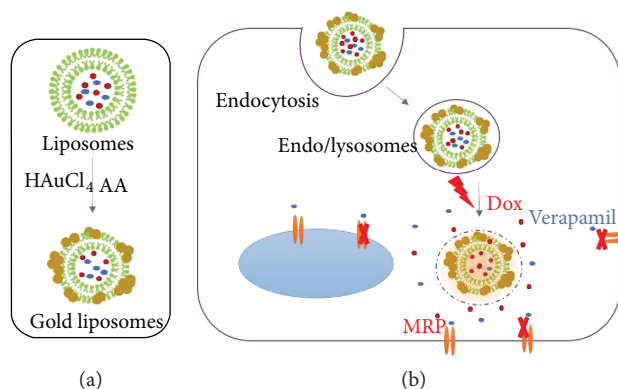
Liposomes, that is, spherically closed lipid bilayers, have been widely used in the biomedical field [6, 7]. Their hollow spherical structure and high loading capacity make them attractive packaging materials for the encapsulation and delivery of drugs, enzymes, and many other biomolecules [8, 9]. Multifunctional hybrid drug delivery systems, that is, polymer- or nanoparticle-modified liposomes, exhibiting the advantages of two or more delivery systems, have become one of the most popular delivery systems [10, 11]. Recently, gold nanoparticles have been incorporated into liposomes to enable the photosensitivity for photothermal therapy [12]. Gold nanoparticles convert light energy into heat for thermal ablation of cancer cells upon laser irradiation [13, 14]. However, an efficient photothermal therapy requires

continuous light irradiation [15, 16]. Besides, heat-induced damage to the bioactive molecules or normal tissues remains one of the main limitations. Although localized heating can be achieved by a ns-short pulsed laser [17], it requires high laser influence to induce substantial cell apoptosis. Recently, gold nanoparticles also have been conjugated with an antiangiogenic peptide to enhance angiogenesis arrest upon visible laser irradiation *in vivo* [18]. Another common biological application of gold nanoparticles is to trigger drug release by the photothermal effect, which only requires lower laser fluence compared to thermotherapy.

Multidrug resistance (MDR) is one of the major unsolved problems for successful cancer chemotherapy. A combination of chemotherapeutic agents with multidrug resistance protein (MRP) inhibitors, such as verapamil, has been shown to have an *in vivo* anticancer synergistic mechanism [19]. However, to effectively inhibit MRPs, a high concentration of MRP inhibitors are required, especially for small molecule inhibitors, which may induce unwanted toxicity to normal tissues. To overcome the current limitations, we coencapsulate doxorubicin and verapamil into gold liposomes and use a ns-pulsed laser to trigger fast intracellular drug release. High intracellular concentrations of doxorubicin and verapamil were achieved upon light irradiation, leading to the increased cytotoxicity of doxorubicin. Gold-nanoparticle-decorated liposomes, that is, gold liposomes were developed, and the light-triggered drug release was tested *in vitro* and in cells. Under light irradiation, gold nanoparticles generate a highly localized heat owing to the surface plasmon resonance [20], and the cargo was released due to the increased permeability of liposomes (Schematics 1). We demonstrated that the ns laser pulse (532 nm, 6 ns) liberated doxorubicin from gold liposomes into the cytosol in drug resistant MDA-MB-231-R cancer cells. Moreover, the cytotoxicity of doxorubicin coencapsulated with verapamil was significantly enhanced upon laser irradiation. This study showed that the photothermal-triggerable liposome is a promising strategy to overcome multidrug resistance and enhance therapeutic effects by on-demand release of chemotherapeutic agents and MRP inhibitors.

## 2. Results and Discussion

**2.1. Preparation and Characterization of Gold Liposomes.** Gold liposomes were developed by the reduction of gold chloride onto the 1,2-dipalmitoyl-sn-glycero-3-phosphocholine (DPPC) liposome surface following a previously reported method [21]. As shown in Table 1, gold liposomes showed a hydrodynamic size around 103 nm, and uncoated liposomes were around 92 nm. Transmission electron microscopy (TEM) observation showed that gold nanoparticles were distributed on the surface (Figure 1(a)). The structure of gold liposomes we observed was similar to the previously reported gold liposomes prepared by the same method [22]. UV-Vis spectra of gold liposomes exhibited an absorption peak at around 650 nm, while uncoated liposomes did not show any resonance peak in the wavelength range of 400–800 nm (Figure 2(b)). The results suggested that the gold nanoparticles have been successfully



SCHEMATICS 1: (a) Schematics for the formation of gold liposomes. (b) Nanosecond-pulsed laser-triggered on-demand intracellular release of verapamil and doxorubicin for overcoming multidrug resistance. AA, ascorbic acid; Dox, doxorubicin.

decorated onto the liposome surface. The gold liposomes that we developed showed high absorbance in the wavelength range of 500–750 nm, suggesting that these gold liposomes could be activated by light in the range of 500–750 nm.

**2.2. Thermal Effect and Nanosecond Laser Pulses Induced Doxorubicin Release.** As shown in Figure 2(a), for uncoated liposomes, when the bulk temperature was lower than 35°C, no obvious leakage was observed. Doxorubicin release sharply increased from 10% to 41% when the temperature reached 38°C. After 38°C, doxorubicin release became slowly increased. The thermal-effect-triggered release is due to the gel-to-liquid crystalline phase transition of the phospholipid bilayer. The pretransition temperature and major transition temperature of DPPC liposomes are 35°C and 41°C, respectively [23]. There was no significant difference between uncoated liposomes and gold liposomes, suggesting that the gold decoration did not significantly alter the phase transition temperature of the DPPC phospholipid bilayer.

Nanosecond-pulsed laser-triggered doxorubicin release was tested with different laser pulse numbers and influence (Figure 2(b)). As expected, doxorubicin release from gold liposomes was dependent on the laser pulse number and influence. With the same pulse influence (100 mJ/cm<sup>2</sup>), the doxorubicin release increased from 20.8% to 58.3% by increasing the pulse number from 1 to 10. A single pulse with a higher influence in the range of 50–200 mJ/cm<sup>2</sup> also led to a higher doxorubicin release. No temperature increase was observed under current experiment conditions, suggesting that a ns-pulsed laser-induced thermal effect was highly localized and no bulk heating was involved in our system. Nanosecond laser irradiation did not trigger any significant doxorubicin release from uncoated liposomes, suggesting that gold nanoparticle decoration was required for ns-pulsed laser activation.

To test whether there was a triggering effect in time, we investigated the kinetics of doxorubicin release upon ns-pulsed laser activation. The results showed that doxorubicin release reached the maximum within 1.0 min (Figure 2(c)), confirming that there was a triggering effect

TABLE 1: Hydrodynamic diameter and polydispersity of uncoated and gold liposomes. Dox, doxorubicin, Ver, verapamil.

Samples	Diameter (nm)	Polydispersity index (PDI)
Uncoated liposomes	$92.5 \pm 5.3$	$0.034 \pm 0.005$
Gold liposomes	$103.8 \pm 10.8$	$0.128 \pm 0.039$
Gold liposomes with laser irradiation	$101.5 \pm 13.7$	$0.157 \pm 0.051$
Dox/Ver loaded liposomes	$101.1 \pm 7.1$	$0.052 \pm 0.013$
Dox/Ver loaded gold liposomes	$115.2 \pm 12.5$	$0.171 \pm 0.045$

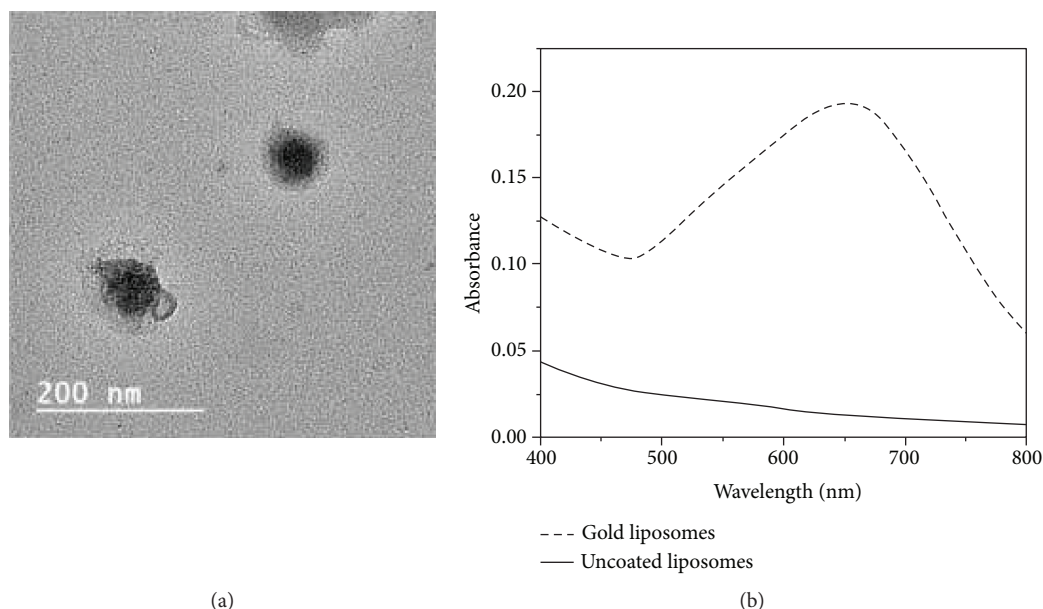


FIGURE 1: Characterization of gold liposomes. (a) Typical TEM image of gold liposomes; (b) UV-Vis spectra of uncoated and gold liposomes.

in cargo release upon light activation. The permeability of gold liposomes was characterized by carboxyfluorescein (CF) leakage studies following a previously reported method [24]. We observed acute CF leakage upon ns-pulsed laser activation and the CF leakage only lasted for 1 min, which was in the same time scale as doxorubicin release (Figure 2(d)). The enhanced membrane permeability and cargo release may happen in an even shorter time scale, unfortunately, limited by current experimental conditions, we cannot do real-time observation.

**2.3. Intracellular Doxorubicin Release.** The ns-pulsed laser-triggered intracellular doxorubicin release was observed by confocal scanning laser microscopy. The fluorescence of doxorubicin was quenched due to its self-association when loaded by the ammonium sulfate method [25]. The release of doxorubicin from liposomes and dilution by the surrounding medium dequench doxorubicin and increase its fluorescence intensity. As shown in Figure 3, ns laser pulses (532 nm, 5 pulses, and  $100 \text{ mJ}/\text{cm}^2$ ) triggered doxorubicin release from the gold liposomes into the cytosol, dramatically increasing the cytosol and nuclear fluorescence intensity. No significant difference was observed for cells treated with uncoated liposomes before and after laser pulse irradiation. The results again confirmed that

gold nanoparticles decorated on the liposome surfaces were required for light-induced release. Many nanocarriers were trapped in endolysosomes after endocytosis, and cannot efficiently liberate encapsulated active compounds, which significantly limits their therapeutic effects. This technique enables intracellular release of trapped therapeutic agents and is promising for enhancing the therapeutic effects. In a previous report, picosecond-pulsed laser-triggered cargo release from gold liposomes has been used to manipulate cell signaling [22]. We believe that our technique may also find many other biological applications where intracellular cargo release is required.

**2.4. Cytotoxicity of Doxorubicin-Loaded Liposomal Carriers.** To test the capability of on-demand release to enhance therapeutic effects, the cytotoxicity of doxorubicin coencapsulated with verapamil in liposomes was measured by MTT. The results showed that laser irradiation dramatically increased the cytotoxicity of doxorubicin loaded in gold liposomes with or without verapamil (Figure 4). The  $\text{IC}_{50}$  of doxorubicin decreased from  $29.5 \mu\text{M}$  to  $2.7 \mu\text{M}$  after incorporation into gold liposomes combined with laser activation. Based on *in vitro* doxorubicin-release studies, around 36% doxorubicin was liberated, which makes the concentration of free doxorubicin in cells treated with gold liposomes and

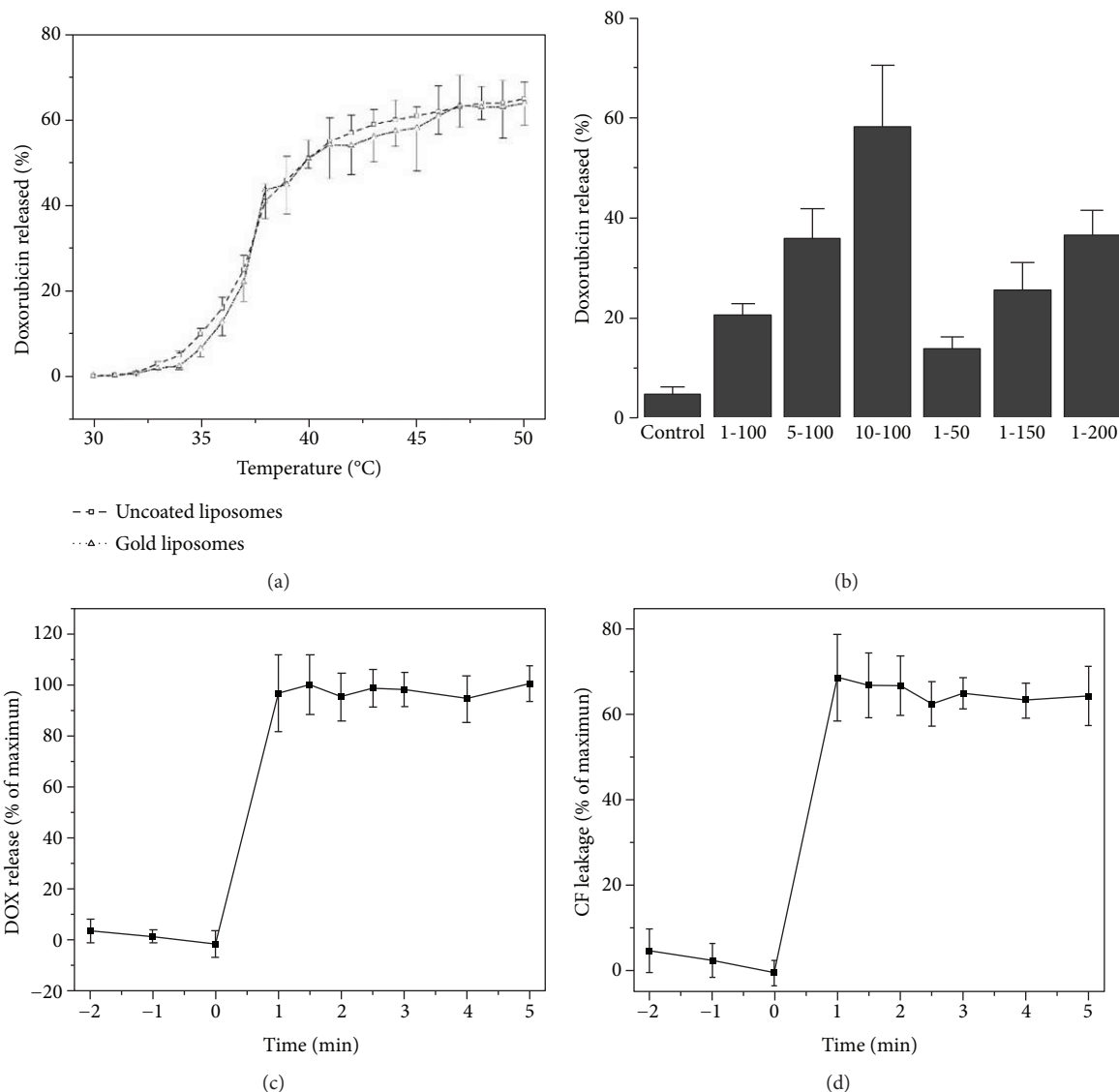


FIGURE 2: Characterization of *in vitro* release. (a) Thermal effect induced doxorubicin release from uncoated liposomes and gold liposomes under programmed bulk heating from 30 to 50°C; (b) nanosecond-pulsed laser-triggered doxorubicin release as a function of laser pulse number and influence; 1-100, 1 represents pulse number and 100 represents laser pulse influence ( $\text{mJ}/\text{cm}^2$ ); (c) kinetics of doxorubicin release upon ns-pulsed laser irradiation (10 pulses,  $100 \text{ mJ}/\text{cm}^2$ ); (d) gold liposome permeability characterized by carboxyfluorescein (CF) leakage studies (10 pulses,  $100 \text{ mJ}/\text{cm}^2$ ).

lasers much lower than those treated with free doxorubicin. However, the cytotoxicity of doxorubicin was enhanced more than 10-fold, which suggested that the triggering effect significantly contributed to enhanced cytotoxicity. Incorporation of verapamil into doxorubicin liposomes significantly increased cytotoxicity of doxorubicin. More importantly, the cytotoxicity of doxorubicin was further enhanced by laser irradiation and the  $\text{IC}_{50}$  decreased to  $1.5 \mu\text{M}$ . Under the current condition, laser irradiation alone did not induce substantial dead cells (Figure 5), suggesting that the enhanced cytotoxicity of doxorubicin by light irradiation was not because of the laser ablation of cancer cells. There are probably two main mechanisms contributing to the enhanced cytotoxicity. First, laser irradiation triggered doxorubicin release into the cytosol, which

provides more free doxorubicin to elicit its pharmacological activity. Second, instant high concentration of verapamil was achieved upon laser activation, which resulted in inhibition of MRPs and reducing doxorubicin efflux mediated by MRPs. However, for doxorubicin encapsulated in uncoated liposomes, no significant difference was observed after laser irradiation.

### 3. Materials and Method

**3.1. Materials.** 1,2-Dipalmitoyl-sn-glycero-3-phosphocholine (DPPC) and cholesterol were purchased from Avanti Polar Lipids. Gold (III) chloride trihydrate ( $\text{HAuCl}_4 \cdot 3\text{H}_2\text{O}$ ) and doxorubicin hydrochloride was purchased from Sigma-Aldrich. Ascorbic acid was from Fisher Scientific. DMEM

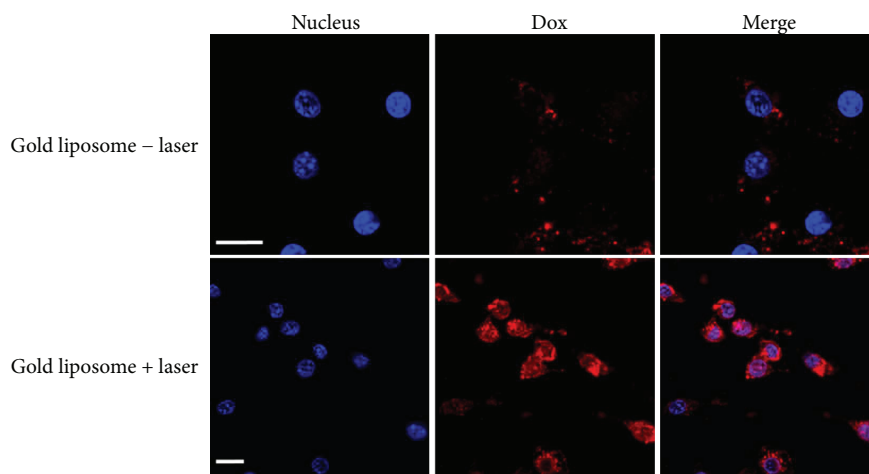


FIGURE 3: Nanosecond-pulsed laser- (532 nm, 5 pulses, and 100 mJ/cm<sup>2</sup>) triggered intracellular doxorubicin release from gold liposomes in MDA-MB-231-R cells. Blue represents nucleus; red represents doxorubicin; scale bar 20  $\mu$ m.

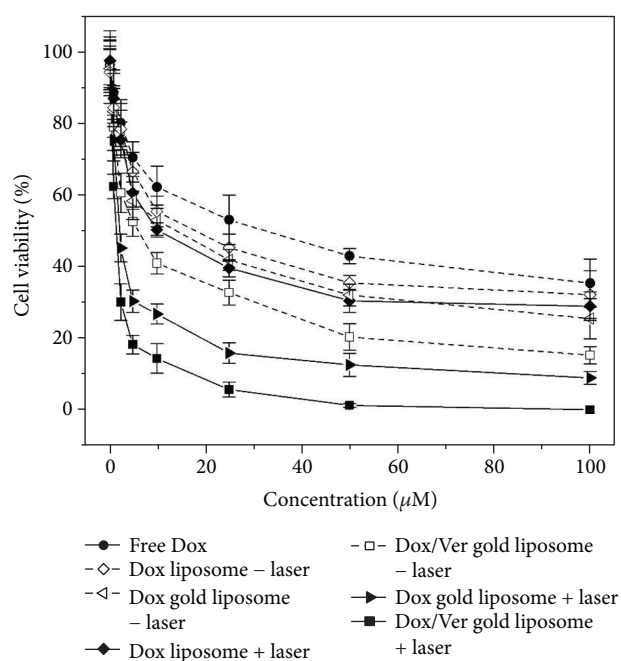


FIGURE 4: Cytotoxicity of doxorubicin encapsulated in different liposomal formulations with or without laser irradiation in MDA-MB-231-R cells. 532 nm, 5 pulses, and 100 mJ/cm<sup>2</sup>.

medium and fetal bovine serum were purchased from GIBCO. 4',6-Diamidino-2-phenylindole (DAPI) was purchased from Thermo Fisher Scientific. Doxorubicin sodium salt was purchased from Alfa Aesar. All other reagents were analytical grade and used without further purification.

**3.2. Preparation and Characterization of Gold Liposomes.** Liposomes were prepared with DPPC and cholesterol at a molar ratio of 70:30. Briefly, lipid powders were dissolved in chloroform and dried under a nitrogen stream, and then placed in a vacuum overnight to completely remove chloroform. The lipid film was hydrated with 300 mM ammonium sulfate (pH = 7.5) with or without 50  $\mu$ M verapamil, followed

by extrusion for 21 times through 100 nm polycarbonate membrane using an Avanti mini extruder. Empty liposomes were passed through the S1000 column preequilibrated with isotonic N-(2-hydroxyethyl)piperazine-N'-(2-ethanesulfonic acid) (HEPES) buffer (140 mM NaCl, 10 mM HEPES, pH = 7.4) to replace the extra ammonium sulfate solution. Subsequently, doxorubicin hydrochloride was added to the liposome suspension to achieve a drug to lipid ratio of 1/3 (mol/mol). The loading process was carried out at 37°C for 2 h. The free doxorubicin was removed by size exclusion chromatography (SEC) eluted with HEPES buffer. Gold was decorated onto the liposome surface following a previously reported method with minor modification [12]. Briefly, liposomes were diluted to 1 mM using the HEPES buffer. Gold chloride solution at a concentration of 20 mM was added and mixed with liposomes, followed by the addition of ascorbic acid solution (40 mM). Following reduction, gold liposomes were dialyzed against the HEPES buffer for 24 h under 4°C to remove unreacted gold chloride and ascorbic acid. The resulting liposomal samples were stored at 4°C until further use. Transmission electron microscopy (TEM) operating at the voltage of 200 kV was used to observe the morphology of gold liposomes. Gold liposomes were diluted with distilled water and dropped onto a carbon-film-coated copper grid. The samples were air-dried for 2 h at room temperature and then imaged. The hydrodynamic radius and polydispersity of liposomal vesicles were determined using dynamic laser light scattering (DLS). Each sample was measured at least 5 times. The UV-Vis spectra of gold liposomes in the range of 400 nm–800 nm was recorded using a spectrometer.

**3.3. Thermal- and Laser-Triggered Doxorubicin Release.** The thermal effect-induced doxorubicin release from gold liposomes were investigated under program-increasing temperature conditions following a previously reported method [23]. The measurements were performed on an F7000 fluorescence spectrometer equipped with a RE5 refrigerated circulating bath. The liposome suspensions were heated from 30 to 50°C in intervals of 1°C. The solution was allowed to

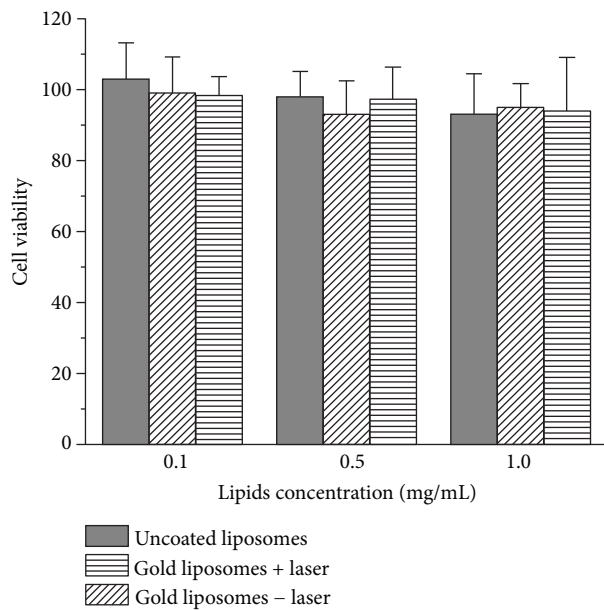


FIGURE 5: Cytotoxicity of plain uncoated liposomes and gold liposomes with or without laser irradiation (532 nm, 5 pulses, and 100 mJ/cm<sup>2</sup>) and in MDA-MB-231-R cells.

rest for 5 min to reach equilibrium before each measurement was taken. The leakage from uncoated liposomes and gold liposomes were measured according to the fluorescence of the leaked doxorubicin. The release of doxorubicin was calculated using (1):

$$R\% = \frac{F_x - F_0}{F_t - F_0}, \quad (1)$$

where  $F_x$  is the fluorescence of samples at each measurement,  $F_0$  is the initial fluorescence of samples before any heating, and  $F_t$  is the fluorescence of 100% release induced by 1% Triton X-100 treatment.

For the light-induced release measurements, uncoated and gold liposome suspensions were placed in transparent 96-well plates. A ns laser at 532 nm with a beam diameter of 5 mm was used to induce release. The samples were exposed to the laser beam at room temperature with different pulses (1, 5, and 10 pulses) and different laser influences (50, 100, 150, and 250 mJ/cm<sup>2</sup>). After laser treatment, the fluorescence of each sample was immediately measured, and the release percentage was calculated using (1). To understand the kinetics of doxorubicin release, the fluorescence intensity of laser-treated samples was monitored at 0, 1, 1.5, 2, 2.5, 3, 4, and 5 min after light irradiation. Carboxyfluorescein (CF) at a concentration of 50 mM was encapsulated into gold liposomes to study the permeability of gold liposomes. CF leakage upon laser irradiation (10 pulses, 100 mJ/cm<sup>2</sup>) was measured using the same protocol as doxorubicin release.

**3.4. Intracellular Doxorubicin Release.** To study the intracellular doxorubicin release triggered by laser irradiation. MDA-MB-231-R cells were cultured in 35 mm glass bottom dishes in DMEM medium for 24 h. The cells were washed

with PBS and replaced with fresh medium that contains doxorubicin-loaded gold liposomes. After 3 h of incubation, the cell nucleus was stained with 5 μg/mL DAPI for 5 min. Cells were then washed with PBS, and supplied with fresh cell media prior to laser irradiation. Nanosecond pulses (5 pulses, 100 mJ/cm<sup>2</sup>) was tested. To study the intracellular distribution of gold liposomes, cells with or without laser irradiation were immediately observed by a confocal laser microscope (Olympus FV 1000).

**3.5. Cytotoxicity Study.** Cytotoxicity studies were done using an MTT (3-(4,5-dimethylthiazol-2-yl)-2,5-diphenyltetrazolium bromide) tetrazolium reduction assay. MDA-MB-231-R cells were cultured overnight in 96-well plates at a density of 1 × 10<sup>4</sup>/well. The control group was free doxorubicin-treated cells, and the treatment groups are doxorubicin-encapsulated uncoated liposomes with or without laser irradiation, doxorubicin-encapsulated gold liposomes with or without laser irradiation, and doxorubicin/verapamil-coencapsulated gold liposomes with or without laser irradiation. The cells were washed with PBS and replaced with fresh medium that contains doxorubicin encapsulated in different gold liposomes. After 3 h of incubation, the cells were washed with PBS for 3 times, and the laser treatment groups were irradiated with a ns laser pulse (532 nm, 5 pulses, and 100 mJ/cm<sup>2</sup>), followed by supplementation with fresh DMEM medium and placed in the incubator for the next 24 h. Subsequently, the cell viability was determined by the MTT assay.

## 4. Conclusion

In conclusion, we developed doxorubicin-and-verapamil-coencapsulated gold liposomes. Mild ns-pulsed laser exposure induced cargo release from gold liposomes without bulk heating. Ns laser pulses (532 nm, 6 ns) induced doxorubicin release from gold liposomes in a laser pulse- and influence-dependent pattern. In MDA-MB-231-R cancer cells, ns laser pulses (100 mJ/cm<sup>2</sup>, 5 pulses) also liberated doxorubicin from endocytosed gold liposomes into the cytosol. Furthermore, laser irradiation significantly increased the cytotoxicity of doxorubicin-and-verapamil-coencapsulated gold liposomes in MDA-MB-231-R cells. The results suggested that ns-pulsed laser-triggered on-demand release of chemotherapeutic agents and MRP inhibitors is promising to overcome multi-drug resistance and enhance therapeutic efficiency.

## Conflicts of Interest

The authors declare that they have no conflicts of interest.

## Acknowledgments

The authors would like to thank William Tsung for English language revision. This work was supported by the Zhejiang Province Medical and Health Technology Program (2016KYA052).

## References

- [1] L. Zou, H. Wang, B. He et al., "Current approaches of photothermal therapy in treating cancer metastasis with nanotherapeutics," *Theranostics*, vol. 6, no. 6, pp. 762–772, 2016.
- [2] E. Y. Lukianova-Hleb, X. Ren, R. R. Sawant, X. Wu, V. P. Torchilin, and D. O. Lapotko, "On-demand intracellular amplification of chemoradiation with cancer-specific plasmonic nanobubbles," *Nature Medicine*, vol. 20, no. 7, pp. 778–784, 2014.
- [3] F. H. Meng, R. Cheng, C. Deng, and Z. Y. Zhong, "Intracellular drug release nanosystems," *Materials Today*, vol. 15, no. 10, pp. 436–442, 2012.
- [4] L. J. E. Anderson, E. Hansen, E. Y. Lukianova-Hleb, J. H. Hafner, and D. O. Lapotko, "Optically guided controlled release from liposomes with tunable plasmonic nanobubbles," *Journal of Controlled Release*, vol. 144, no. 2, pp. 151–158, 2010.
- [5] Z. Chen, N. Li, L. Chen, J. Lee, and J. J. Gassensmith, "Dual functionalized bacteriophage Q $\beta$  as a photocaged drug carrier," *Small*, vol. 12, no. 33, pp. 4563–4571, 2016.
- [6] D. Chen, D. N. Xia, X. Y. Li et al., "Comparative study of Pluronic<sup>®</sup> F127-modified liposomes and chitosan-modified liposomes for mucus penetration and oral absorption of cyclosporine A in rats," *International Journal of Pharmaceutics*, vol. 449, no. 1–2, pp. 1–9, 2013.
- [7] X. Li, D. Chen, C. Le et al., "Novel mucus-penetrating liposomes as a potential oral drug delivery system: preparation, in vitro characterization, and enhanced cellular uptake," *International Journal of Nanomedicine*, vol. 6, pp. 3151–3162, 2011.
- [8] A. S. Jain, V. V. Dhawan, B. Sarmiento, and M. S. Nagarsenker, "In vitro and ex vivo evaluations of lipid anti-cancer nanoformulations: insights and assessment of bioavailability enhancement," *AAPS PharmSciTech*, vol. 17, no. 3, pp. 553–571, 2016.
- [9] Q. L. Zhu, X. Y. Li, D. N. Xia et al., "Lipid-based formulations for oral drug delivery: effects on drug absorption and metabolism," *Current Drug Metabolism*, vol. 16, no. 3, pp. 200–210, 2015.
- [10] X. Y. Li, S. Y. Guo, C. L. Zhu et al., "Intestinal mucosa permeability following oral insulin delivery using core shell corona nanolipoparticles," *Biomaterials*, vol. 34, no. 37, pp. 9678–9687, 2013.
- [11] V. J. Mohanraj, T. J. Barnes, and C. A. Prestidge, "Silica nanoparticle coated liposomes: a new type of hybrid nanocapsule for proteins," *International Journal of Pharmaceutics*, vol. 392, no. 1–2, pp. 285–293, 2010.
- [12] A. K. Rengan, A. B. Bukhari, A. Pradhan et al., "In vivo analysis of biodegradable liposome gold nanoparticles as efficient agents for photothermal therapy of cancer," *Nano Letters*, vol. 15, no. 2, pp. 842–848, 2015.
- [13] R. Mendes, P. Pedrosa, J. C. Lima, A. R. Fernandes, and P. V. Baptista, "Photothermal enhancement of chemotherapy in breast cancer by visible irradiation of gold nanoparticles," *Scientific Reports*, vol. 7, no. 1, article 10872, 2017.
- [14] D. Bartczak, O. L. Muskens, T. M. Millar, T. Sanchez-Elsner, and A. G. Kanaras, "Laser-induced damage and recovery of plasmonically targeted human endothelial cells," *Nano Letters*, vol. 11, no. 3, pp. 1358–1363, 2011.
- [15] R. Huschka, O. Neumann, A. Barhoumi, and N. J. Halas, "Visualizing light-triggered release of molecules inside living cells," *Nano Letters*, vol. 10, no. 10, pp. 4117–4122, 2010.
- [16] E. S. Levy, D. P. Morales, J. V. Garcia, N. O. Reich, and P. C. Ford, "Near-IR mediated intracellular uncaging of NO from cell targeted hollow gold nanoparticles," *Chemical Communications*, vol. 51, no. 100, pp. 17692–17695, 2015.
- [17] C. Jack, A. S. Karimullah, R. Tullius et al., "Spatial control of chemical processes on nanostructures through nano-localized water heating," *Nature Communications*, vol. 7, article 10946, 2016.
- [18] P. Pedrosa, A. Heuer-Jungemann, A. G. Kanaras, A. R. Fernandes, and P. V. Baptista, "Potentiating angiogenesis arrest in vivo via laser irradiation of peptide functionalised gold nanoparticles," *Journal of Nanobiotechnology*, vol. 15, no. 1, p. 85, 2017.
- [19] M. McCarthy, G. Auda, S. Agrawal et al., "In vivo anticancer synergy mechanism of doxorubicin and verapamil combination treatment is impaired in BALB/c mice with metastatic breast cancer," *Experimental and Molecular Pathology*, vol. 97, no. 1, pp. 6–15, 2014.
- [20] K. Jiang, D. A. Smith, and A. Pinchuk, "Size-dependent photothermal conversion efficiencies of plasmonically heated gold nanoparticles," *The Journal of Physical Chemistry C*, vol. 117, no. 51, pp. 27073–27080, 2013.
- [21] S. J. Leung, X. M. Kachur, M. C. Bobnick, and M. Romanowski, "Wavelength-selective light-induced release from plasmon resonant liposomes," *Advanced Functional Materials*, vol. 21, no. 6, pp. 1113–1121, 2011.
- [22] X. Y. Li, Z. F. Che, K. Mazhar, T. J. Price, and Z. P. Qin, "Ultrafast near-infrared light-triggered intracellular uncaging to probe cell signaling," *Advanced Functional Materials*, vol. 27, no. 11, 2017.
- [23] Y. Q. Xia, S. Qi, X. L. Zhang et al., "Construction of thermal- and light-responsive liposomes noncovalently decorated with gold nanoparticles," *RSC Advances*, vol. 4, no. 84, pp. 44568–44574, 2014.
- [24] L. Clary, G. Verderone, C. Santaella, and P. Vierling, "Membrane permeability and stability of liposomes made from highly fluorinated double-chain phosphocholines derived from diaminoopropanol, serine or ethanolamine," *Biochimica et Biophysica Acta (BBA) - Biomembranes*, vol. 1328, no. 1, pp. 55–64, 1997.
- [25] T. Ishida, M. J. Kirchmeier, E. H. Moase, S. Zalipsky, and T. M. Allen, "Targeted delivery and triggered release of liposomal doxorubicin enhances cytotoxicity against human B lymphoma cells," *Biochimica et Biophysica Acta (BBA) - Biomembranes*, vol. 1515, no. 2, pp. 144–158, 2001.

## Research Article

# Nano-(Ta, Zr)C Precipitates at Multigrain Conjunctions in TaC Ceramic with 10 mol% ZrC and 5 mol% Cu as Sintering Aid

Lianbing Zhong,<sup>1</sup> Guihong Geng,<sup>2</sup> Yujin Wang,<sup>1</sup> Feng Ye,<sup>1</sup> and Limeng Liu <sup>1,2</sup>

<sup>1</sup>School of Materials Science and Engineering, Harbin Institute of Technology, Xidazhi Street 91, Harbin 150001, China

<sup>2</sup>School of Materials Science and Engineering, North Minzu University, Wenchangbei Street 204, Yinchuan 750021, China

Correspondence should be addressed to Limeng Liu; [llm681@sina.com](mailto:llm681@sina.com)

Received 4 September 2017; Accepted 24 December 2017; Published 24 January 2018

Academic Editor: Leszek A. Dobrzański

Copyright © 2018 Lianbing Zhong et al. This is an open access article distributed under the Creative Commons Attribution License, which permits unrestricted use, distribution, and reproduction in any medium, provided the original work is properly cited.

A fully dense TaC ceramic was prepared by hot pressing using 10 mol% ZrC plus 5 mol% Cu as a sintering aid. Formation of (Ta, Zr)C solid solution (ss) by reaction between TaC and ZrC facilitated densification. Addition of Cu refined the microstructure and consequently improved flexural strength of the TaC ceramics. TEM investigation found ubiquitous precipitation of nanocrystallites at multigrain conjunctions. The nanocrystallites were (Ta, Zr)C solid solution with uniform dispersion in an oxygen-rich glassy matrix. Although formation of nanoprecipitates may not much affect the mechanical properties of the TaC ceramic, the structure suggested a new type of nanoceramic worth further research.

## 1. Introduction

Tantalum carbide (TaC) is one of the ultrahigh temperature ceramics (UHTC) [1] as it has high melting point (~3983°C), good electrical and thermal conductivity, and relatively good mechanical properties. Because TaC ceramics are extremely hard to densify [2], sintering aids such as C [3–6], Si [7, 8], B<sub>4</sub>C [9, 10], SiC [11, 12], TaSi<sub>2</sub> [13, 14], MoSi<sub>2</sub> [13, 15], TaB<sub>2</sub> [9, 10, 16], and Si<sub>3</sub>N<sub>4</sub> [17] were used to increase densification. In a previous work, TaC ceramics were hot pressed with ZrC plus Cu as sintering aids [18]. Herein, secondary phases in the TaC ceramics were detailed by transmission electron microscopy (TEM) and high resolution transmission electron microscopy (HRTEM) to show precipitation of nanocrystallites in a continuous glassy phase at multigrain conjunctions. The structure at the multigrain conjunction was very similar to a glass ceramic in terms of precipitation of crystallites in a glass matrix. Considering the good physiochemical properties of the TaC and the ZrC compound, the intergranular composition of the TaC ceramics may suggest a new type of nano-(Ta, Zr)C ceramic of good electrical and thermal conductivities.

## 2. Experimental

TaC (Ningxia Orient Tantalum Industry, Yinchuan, China), ZrC (Aladdin Reagent Company, Shanghai, China), and Cu (Aladdin Reagent Company, Shanghai, China) powders were used as starting materials. A powder mixture with a TaC:ZrC:Cu molar ratio of 1.00:0.10:0.05 was homogenized and was hot pressed in a graphite furnace (15 t Hot Press Furnace, Materials Research Furnaces, Inc., USA) at 1900°C for 30 min under 30 MPa pressure in an Ar flux with a flowing rate of 2.0 L/min. Density was measured and relative density was calculated. Crystalline phases were detected by XRD (X-ray diffraction, XRD-6000, Shimadzu, Japan). Polished-and-thermally etched surfaces parallel to the hot pressing direction were observed by SEM (Electron Scanning Microscopy, SSX-500, Shimadzu, Japan). A thin piece was sliced along diameter of the sample, followed by manual thinning and ion milling to prepare foil for TEM observation (Tecnai G2 F30, FEI Co., Oregon, USA). Chemical compositions of interested areas were detected by Energy Dispersive Spectroscopy (EDS, Bruker Nano GmbH, Berlin, Germany) operating at an excitation voltage of 200 kV.

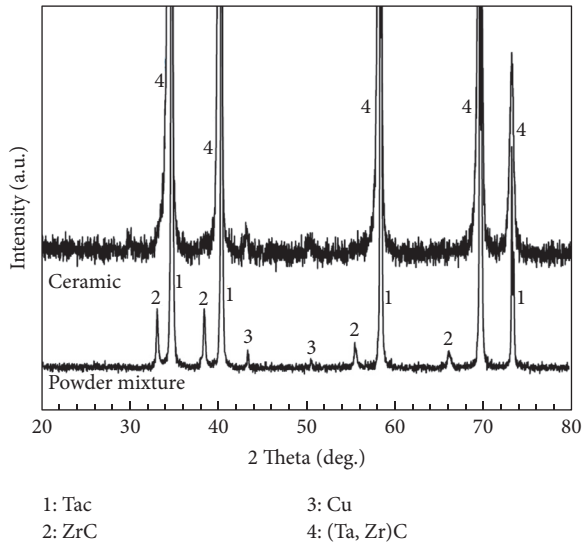


FIGURE 1: XRD pattern of the TaC-20 mol% ZrC-5 mol% Cu powder mixture and the consolidated ceramic.

Selected area electron diffraction (SAED) was performed to identify the phases.

### 3. Results and Discussion

**3.1. General Observation.** The consolidated TaC ceramic reached a relative density value of 97.6% to give good flexural strength of  $589 \pm 47$  MPa and fracture toughness of  $5.0 \text{ MPa}\cdot\text{m}^{1/2}$ . In comparison, pure TaC without using any sintering aid showed low values of relative density and mechanical properties [2, 17]. The enhanced densification of the investigated composition relative to pure TaC was due to mutual diffusion of  $\text{Zr}^{4+}$  and  $\text{Ta}^{4+}$  cations to form (Ta, Zr)C solid solution (ss). Metallic Cu also helped increase densification of the TaC ceramic. XRD patterns for both the powder mixture and the consolidated ceramic are shown in Figure 1. Diffractions of Cu were barely observable, while ZrC phase was absent in the consolidated ceramic. The dominant XRD peaks from the consolidated ceramic were indexed by TaC with significant broadening and shift towards lower  $2\theta$  positions, indicating formation of a (Ta, Zr)C ss [18, 19]. SEM of the polished-and-thermally etched surface (not shown) revealed uniform equiaxed grains having an average diameter from  $\sim 0.9$  to  $6.4 \mu\text{m}$ .

**3.2. Formation of Nano-(Ta, Zr)C at Multigrain Junctions.** A typical TEM micrograph of the ceramic is shown in Figure 2(a). SAED of the predominant phase (Figure 2(d)) was consistent with (Ta, Zr)C ss. EDS (Figure 2(e)) revealed Zr in addition to Ta and C, which is in agreement with formation of (Ta, Zr)C ss as revealed by XRD. Mo and Cr signals occasionally detected by EDS were due to effects of the TEM sample holder, not belonging to any phase in the

ceramic. Neither O nor Cu was detected in the (Ta, Zr)C ss grains.

Pockets containing secondary phases existed at multigrain junctions. A SAED pattern of the phase at a multigrain junction is shown in Figure 2(c). The continuous ring diffraction pattern (DP, Figure 2(c)) indicated nanocrystallites. HRTEM image (Figure 2(b)) of the same area evidenced nanocrystallites with average grain size less than 10 nm. Interplanar spacings of the nanocrystals (i.e.,  $d_{hkl}$  values) were calculated by the ring DP to be in agreement with TaC, with slightly larger  $d_{hkl}$  relative to pure TaC, which could be explained by incorporation of Zr into TaC lattice to form (Ta, Zr)C ss.

EDS result of the nanocrystallites (Figure 2(e)) showed predominant Ta, Zr, and C, consistent with (Ta, Zr)C ss. Significant amount of O was also detected, indicating other phases rich in O in equilibrium with the (Ta, Zr)C ss. In the HRTEM image, Figure 2(b), completely disordered regions were presented in neighbor of the nano-(Ta, Zr)C crystallites. The TaC and ZrC powder contained O impurity to estimate 1.23 wt%  $\text{Ta}_2\text{O}_5$  and 0.388 wt%  $\text{ZrO}_2$ , respectively, in the TaC + ZrC + Cu powder compact. The glassy phase was formed by eutectic reaction between  $\text{Ta}_2\text{O}_5$  and  $\text{ZrO}_2$  at the sintering temperature of  $1900^\circ\text{C}$ , because eutectic temperature is less than  $1887^\circ\text{C}$  in the  $\text{Ta}_2\text{O}_5$ - $\text{ZrO}_2$  system. TaC and ZrC presumably dissolved in the eutectic liquid at high temperatures and subsequently precipitated nano-(Ta, Zr)C upon cooling, while the eutectic liquid was quenched to form the glassy matrix.

Formation of nano-(Ta, Zr)C at multigrain junctions in the TaC ceramic was ubiquitous. Analysis for another intergranular pocket is shown in Figure 3. Chemistry and SAED (Figures 3(b) and 3(d)) both evidenced nano-(Ta, Zr)C ss, the same as shown in Figure 2. Metallic Cu was identified here and there by SAD (Figure 3(c)) and EDS (Figure 3(b)). Small concentrations of C, O, Ta, and Zr were also detected in combination with Cu due to effect of the neighboring (Ta, Zr)C grains. Cu did not react with either  $\text{Ta}_2\text{O}_5$  or  $\text{ZrO}_2$  from room temperature to  $2000^\circ\text{C}$ , according to thermodynamics calculation. The intergranular metallic Cu may form a liquid at high temperature to facilitate nano-(Ta, Zr)C formation.

**3.3. Brief Discussion on the Nanoprecipitates.** In summary, nano-(Ta, Zr)C was ubiquitously observed for the first time at multigrain junctions in the TaC ceramic with 10 mol% ZrC plus 5 mol% Cu as the sintering aid. Formation of nanoprecipitates may not much affect room-temperature mechanical properties of the TaC ceramic [17], while thermal-physical properties such as thermal shock resistance could shift due to possible changes in thermal conductivity and interfacial structure, though investigation of such thermal-physical properties was out of the scope of this paper. Nevertheless, this observation may suggest a composition possibly for a new nanoceramic with a uniform dispersion of (Ta, Zr)C nanoparticles less than 10 nm in size in a continuous O-rich glassy matrix. Polycrystalline nanomaterials are expected

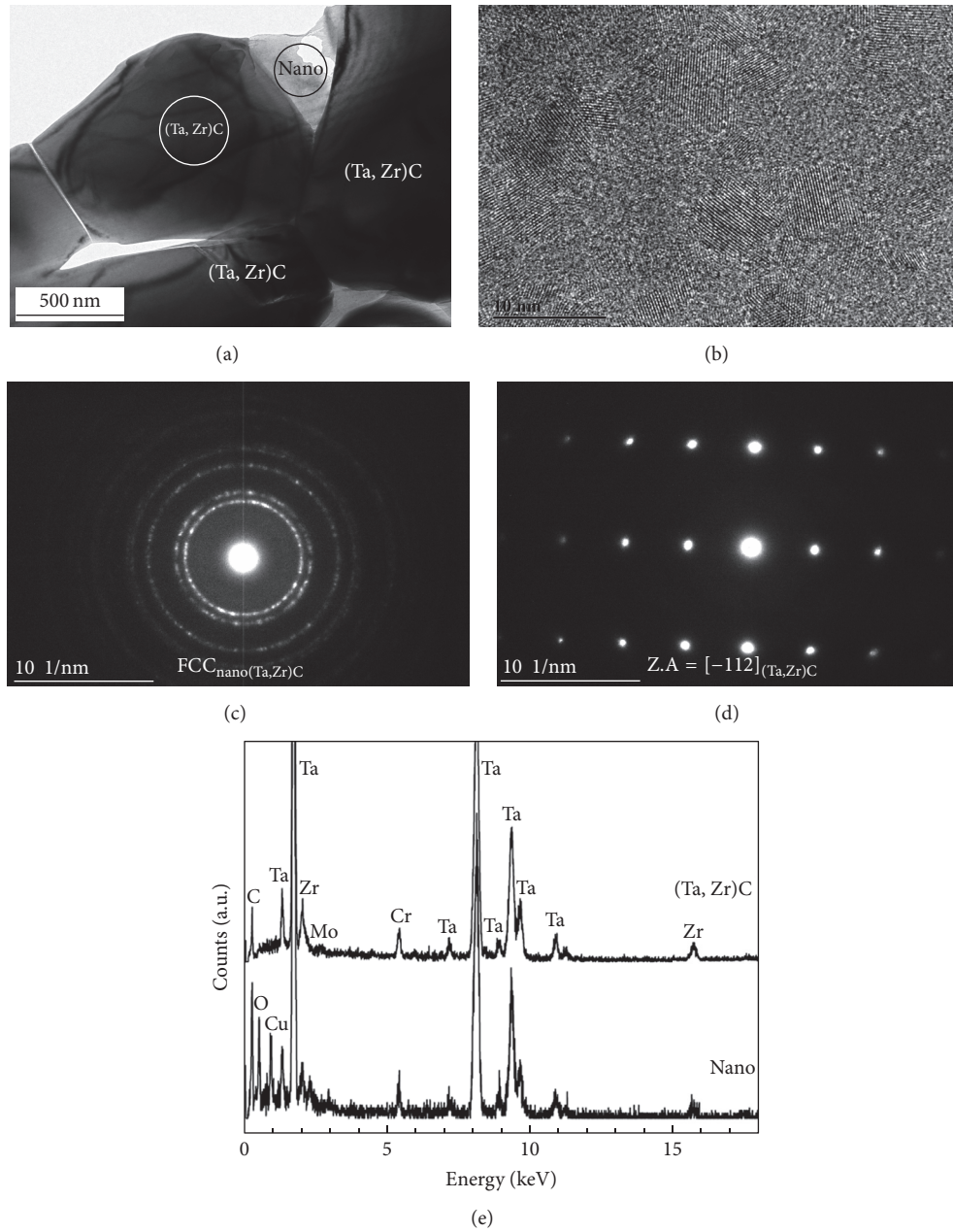


FIGURE 2: TEM of the consolidated TaC ceramic with 10 mol% ZrC plus 5 mol% Cu as sintering aid (a). HRTEM (b) and ring DP (c) of the circled area at multigrain junction evidenced formation of polycrystalline nano-(Ta, Zr)C. (d) DP of the circled (Ta, Zr)C grain, and (e) EDS of the circled area at multigrain junction and the (Ta, Zr)C grain.

to show extraordinary properties but are extremely hard to synthesize. One possible route to fabricate nanoceramics is via controlled crystallization of glass ceramics. Dispersion of nano-(Ta, Zr)C crystallites in the glassy phase at multigrain junctions in the TaC ceramic indicated such a glass ceramic system, though further works on optimizing the composition and the processing parameters are needed in order to successfully develop such a conceptual (Ta, Zr)C nanoceramic.

#### 4. Conclusion

Microstructure of the TaC ceramic with 10 mol% ZrC plus 5 mol% Cu as a sintering aid was investigated by means of TEM, HRTEM, SAED, and DES. TaC and ZrC reacted to form a (Ta, Zr)C solid solution, while metallic Cu remained at multigrain junctions. Uniform dispersion of nano-(Ta, Zr)C crystallites less than 10 nm in size in a continuous O-rich glassy matrix was observed ubiquitously at multigrain

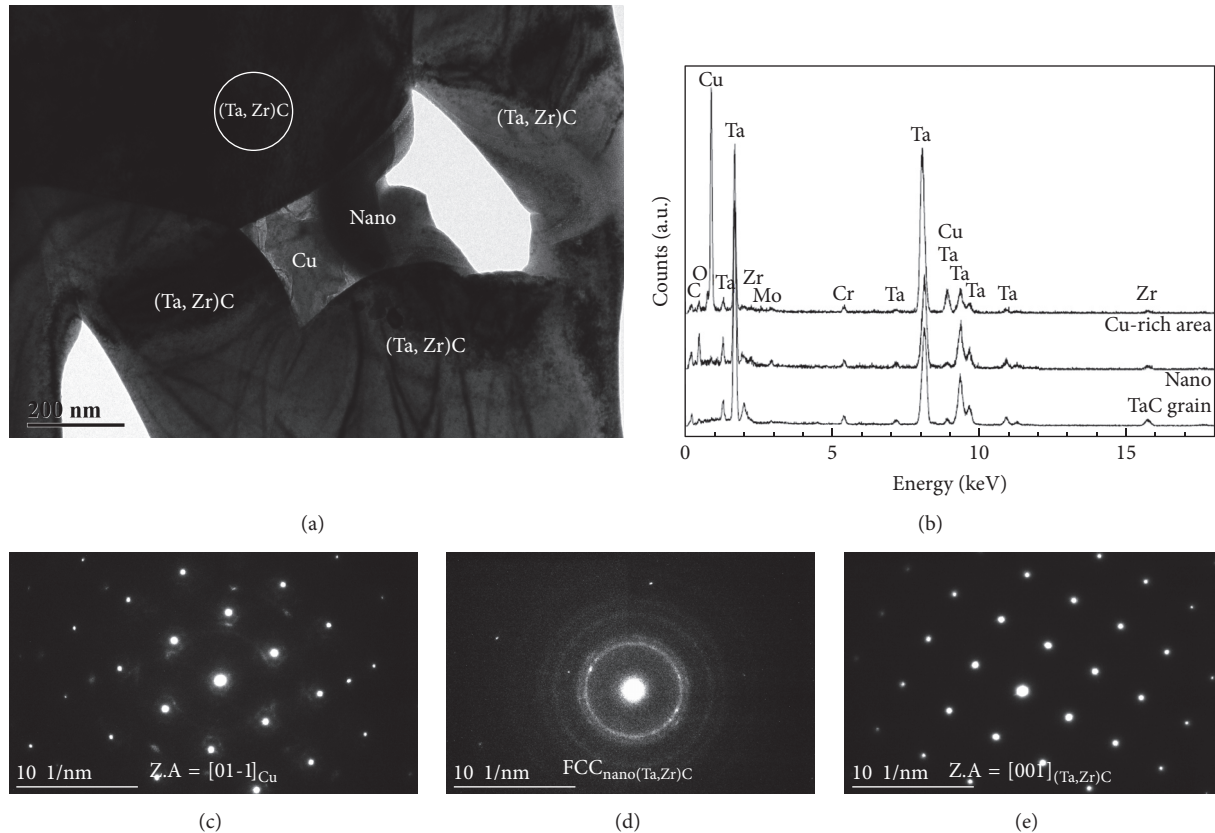


FIGURE 3: TEM of the consolidated TaC ceramic with 10 mol% ZrC plus 5 mol% Cu as sintering aid (a). EDS (b) and DP (c) evidenced metallic Cu. And again (d) ring DP showed polycrystalline nano-(Ta, Zr)C in neighbor of Cu and (e) DP of the circled (Ta, Zr)C grain.

conjunctions. Effects of such nanoprecipitates on properties of the TaC ceramic are not clear yet.

## Conflicts of Interest

The authors declare that they have no conflicts of interest.

## Acknowledgments

This work was supported by the National Natural Science Foundation of China under Grant no. 51662001.

## References

- [1] K. Hackett, S. Verhoef, R. A. Cutler, and D. K. Shetty, "Phase constitution and mechanical properties of carbides in the Ta-C system," *Journal of the American Ceramic Society*, vol. 92, no. 10, pp. 2404–2407, 2009.
- [2] J. P. Kelly and O. A. Graeve, "Mechanisms of pore formation in high-temperature carbides: case study of TaC prepared by spark plasma sintering," *Acta Materialia*, vol. 84, no. 4, pp. 472–483, 2015.
- [3] X. H. Zhang, G. E. Hilmas, W. G. Fahrenholtz, and D. M. Deason, "Hot pressing of tantalum carbide with and without sintering additives," *Journal of the American Ceramic Society*, vol. 90, no. 2, pp. 393–401, 2007.
- [4] D. Lahiri, E. Khaleghi, S. R. Bakshi, W. Li, E. A. Olevisky, and A. Agarwal, "Graphene-induced strengthening in spark plasma sintered tantalum carbide-nanotube composite," *Scripta Materialia*, vol. 68, no. 5, pp. 285–288, 2013.
- [5] A. Nieto, D. Lahiri, and A. Agarwal, "Graphene NanoPlatelets reinforced tantalum carbide consolidated by spark plasma sintering," *Materials Science and Engineering: A Structural Materials: Properties, Microstructure and Processing*, vol. 582, pp. 338–346, 2013.
- [6] A. Nieto, D. Lahiri, and A. Agarwal, "Nanodynamic mechanical behavior of graphene nanoplatelet-reinforced tantalum carbide," *Scripta Materialia*, vol. 69, no. 9, pp. 678–681, 2013.
- [7] L. Zhong, L. Liu, C. Worsch, J. Gonzalez, A. Springer, and F. Ye, "Transient liquid phase sintering of tantalum carbide ceramics by using silicon as the sintering aid and its effects on microstructure and mechanical properties," *Materials Chemistry and Physics*, vol. 149, pp. 505–511, 2015.
- [8] G. H. Geng, L. M. Liu, Y. J. Wang et al., *Ceram. Soc*, vol. 100, pp. 2461–2470, 2017.
- [9] I. G. Talmy, J. A. Zaykoski, and M. M. Opeka, "Synthesis, processing and properties of TaC-TaB<sub>2</sub>-C ceramics," *Journal of the European Ceramic Society*, vol. 30, no. 11, pp. 2253–2263, 2010.
- [10] X. H. Zhang, G. E. Hilmas, and W. G. Fahrenholtz, "Densification, mechanical properties, and oxidation resistance of TaC-TaB<sub>2</sub> ceramics," *Journal of the American Ceramic Society*, vol. 91, no. 12, pp. 4129–4132, 2008.

- [11] H. Liu, L. Liu, F. Ye, Z. Zhang, and Y. Zhou, "Microstructure and mechanical properties of the spark plasma sintered TaC/SiC composites: Effects of sintering temperatures," *Journal of the European Ceramic Society*, vol. 32, no. 13, pp. 3617–3625, 2012.
- [12] L. M. Liu, F. Ye, Z. G. Zhang, and Y. Zhou, "Microstructure and mechanical properties of the spark plasma sintered TaC/SiC composites," *Materials Science and Engineering A*, vol. 529, pp. 479–484, 2011.
- [13] D. Sciti, L. Silvestroni, S. Guicciardi, D. D. Fabbri, and A. Bellosi, "Processing, mechanical properties and oxidation behavior of TaC and HfC composites containing 15 vol% TaSi<sub>2</sub> or MoSi<sub>2</sub>," *Journal of Materials Research*, vol. 24, no. 6, pp. 2056–2065, 2009.
- [14] L. Silvestroni and D. Sciti, "Transmission electron microscopy on Hf- and Ta-carbides sintered with TaSi<sub>2</sub>," *Journal of the European Ceramic Society*, vol. 31, no. 15, pp. 3033–3043, 2011.
- [15] S. A. Ghaffari, M. A. Faghihi-Sani, F. Golestani-Fard, and H. Mandal, "Spark plasma sintering of TaC-HfC UHTC via disilicides sintering aids," *Journal of the European Ceramic Society*, vol. 33, no. 8, pp. 1479–1484, 2013.
- [16] D. Demirskyi and Y. Sakka, "High-temperature reaction consolidation of TaC–TiB<sub>2</sub> ceramic composites by spark-plasma sintering," *Journal of the European Ceramic Society*, vol. 35, no. 1, pp. 405–410, 2015.
- [17] L. M. Liu, G. Geng, Y. Jiang et al., "Microstructure and mechanical properties of tantalum carbide ceramics: Effects of Si<sub>3</sub>N<sub>4</sub> as sintering aid," *Ceramics International*, vol. 43, no. 6, pp. 5136–5144, 2017.
- [18] L. M. Liu, G. Geng, W. Hai, Y. Chen, and L. Wu, "Effects of adding 5–20 mol% ZrC plus 5 mol% Cu as a sintering aid on microstructure and mechanical properties of the TaC ceramics," *Ceramics International*, vol. 42, no. 14, pp. 16248–16254, 2016.
- [19] O. Cedillos-Barraza, S. Grasso, N. A. Nasiri, D. D. Jayaseelan, M. J. Reece, and W. E. Lee, "Sintering behaviour, solid solution formation and characterisation of TaC, HfC and TaC-HfC fabricated by spark plasma sintering," *Journal of the European Ceramic Society*, vol. 36, no. 7, pp. 1539–1548, 2016.

## Research Article

# Influence of Milling Time on Structural and Microstructural Parameters of Ni<sub>50</sub>Ti<sub>50</sub> Prepared by Mechanical Alloying Using Rietveld Analysis

E. Sakher <sup>1,2</sup>, N. Loudjani,<sup>3</sup> M. Benchiheb,<sup>2</sup> and M. Bououdina <sup>4</sup>

<sup>1</sup>Laboratoire de Physique des Solides, Department of Physics, Faculty of Science, University Badji Mokhtar, Annaba, Algeria

<sup>2</sup>Laboratoire d'Elaboration et d'Analyse des Matériaux LEAM, Department of Physics, Faculty of Science, University Badji Mokhtar, Annaba, Algeria

<sup>3</sup>Laboratoire de Microstructures et Defauts, Department of Physics, Faculty of Science, University of Mentouri, Constantine, Algeria

<sup>4</sup>Department of Physics, College of Science, University of Bahrain, P.O. Box 32038, Manama, Bahrain

Correspondence should be addressed to E. Sakher; [elfahem.sakher@univ-annaba.org](mailto:elfahem.sakher@univ-annaba.org)

Received 16 September 2017; Accepted 5 December 2017; Published 14 January 2018

Academic Editor: Leszek A. Dobrzański

Copyright © 2018 E. Sakher et al. This is an open access article distributed under the Creative Commons Attribution License, which permits unrestricted use, distribution, and reproduction in any medium, provided the original work is properly cited.

Nanostructured Ni<sub>50</sub>Ti<sub>50</sub> powders were prepared by mechanical alloying from elemental Ni and Ti micrometer-sized powders, using a planetary ball mill type Fritsch Pulverisette 7. In this study, the effect of milling time on the evolution of structural and microstructural parameters is investigated. Through Rietveld refinements of X-ray diffraction patterns, phase composition and structural/microstructural parameters such as lattice parameters, average crystallite size  $\langle L \rangle$ , microstrain  $\langle \epsilon^2 \rangle^{1/2}$ , and stacking faults probability (SFP) in the frame of MAUD software have been obtained. For prolonged milling time, a mixture of amorphous phase, NiTi-martensite (B19'), and NiTi-austenite (B2) phases, in addition to FCC-Ni(Ti) and HCP-Ti(Ni) solid solutions, is formed. The crystallite size decreases to the nanometer scale while the internal strain increases. It is observed that, for longer milling time, plastic deformations introduce a large amount of stacking faults in HCP-Ti(Ni) rather than in FCC-Ni(Ti), which are mainly responsible for the observed large amount of the amorphous phase.

## 1. Introduction

NiTi-based shape memory alloys have attracted great scientific and technological interests, due to their remarkable mechanical and chemical properties, such as superelasticity, shape memory behavior, good corrosion resistance [1, 2], hydrogen storage ability, and good biocompatibility [3, 4]; thereby they are very appropriate for biomedical and dentistry applications [5, 6]. The observed shape memory effect in NiTi alloy is mainly caused by the existence of NiTi-austenite (B2) and NiTi-martensite (B19') phases [7].

Numerous methods have been used to synthesize nanocrystalline shape memory alloys (NSMAs), including ion-milling deposition [8], melt-spinning [9], high-pressure torsion [10], and sol-gel technique [11]. Meanwhile, physical techniques for producing NiTi intermetallic compound using

elemental Ni and Ti powders [12] have been reported such as conventional powder metallurgy [13], self-propagating high temperature synthesis [14], explosive shock-wave compression [15], and mechanical alloying (MA) [16].

Among the above-cited methods, mechanical alloying (MA) was found to be very effective in the synthesis of Ni<sub>50</sub>Ti<sub>50</sub>-based nanocrystalline alloys or nanostructured powders. Through this technique, a large variety of materials are produced such as intermetallics, extended solid solutions, quasicrystals, and amorphous phases [17]. Moreover, in this process, the reduction of particle size is observed, resulting in ultra-fine grained or nanocrystalline materials. Because of the very fine grain size, nanocrystalline materials exhibit diverse and interesting properties, which are different and often considerably improved in comparison with conventional coarse-grained polycrystalline materials [18]. MA of Ni<sub>50</sub>Ti<sub>50</sub>

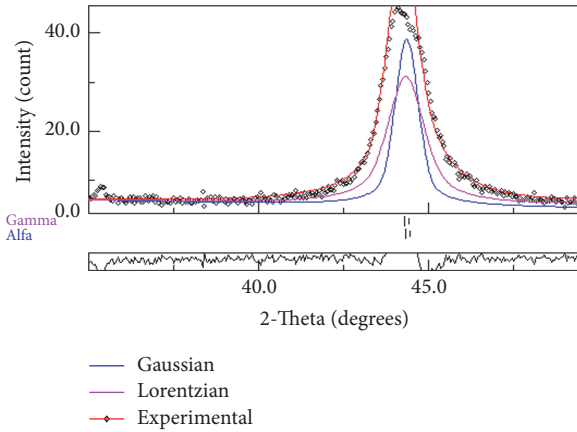


FIGURE 1: The illustration of Gaussian and Lorentzian peak-shape functions.

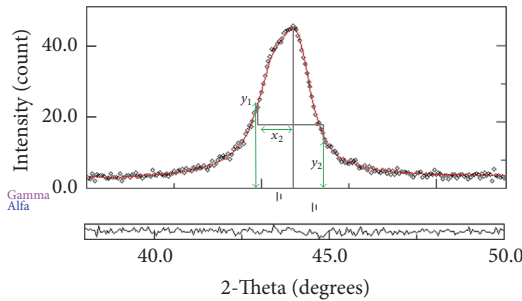


FIGURE 2: The schematic illustration of the asymmetric diffraction peak.

elemental powders mixture can lead to amorphous phase, nanocrystalline solid solution [12], NiTi-austenite (B2), and NiTi-martensite (B19') phase [19].

Moreover, it is very important to characterize the powders obtained by MA in terms of phase composition in addition to structural and microstructural features. The crystallite size and microstrain in powdered particles can be determined through X-ray diffraction peak broadening. Herein, it is worth mentioning that the shape of peak can be described as a combination of two functions: Gaussian associated with microstrain and Lorentzian associated with crystallite size (Figures 1, 2, and 3) [20, 21]. Meanwhile, instrumental parameters have to be taken into consideration. Numerous models, like Williamson-Hall [22], Halder-Wagner [23], Warren-Averbach [24], and Rietveld method [25], have been widely used for the determination of structural and microstructural parameters.

The Rietveld analysis, a full-pattern fitting of X-ray diffraction patterns, has been reported as a powerful method for structural and microstructural characterization [26], including qualitative and quantitative phase analyses of multiphase nanocrystalline materials containing significant number of overlapping reflections [27]. In the literature, Rietveld's method was successfully adopted for the determination of microstructural parameters of various systems [28–30].

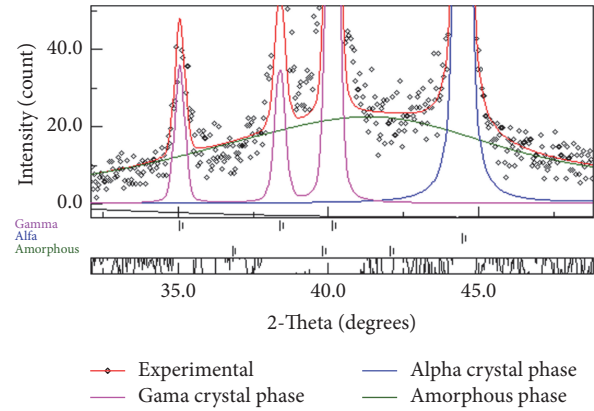


FIGURE 3: Contribution of crystalline and amorphous phases to an XRD pattern.

The aim of this research work is devoted to the investigation of milling time on structural and microstructural modifications occurring in mechanically alloyed Ni<sub>50</sub>Ti<sub>50</sub> powder mixture. In-depth analysis using the Rietveld method of X-ray data is carried out, in terms of phase composition, crystallite size, microstrain, lattice parameter, and lattice defects such as dislocation density and stacking faults.

## 2. Experimental Part

**2.1. Mechanical Alloying of Ni<sub>50</sub>Ti<sub>50</sub> Powder Mixture.** High purity elemental Ti (~150 μm, 99.97%) and Ni (~45 μm, 99.99%) powders (Aldrich) were mixed in appropriate proportions in order to obtain the Ni<sub>50</sub>Ti<sub>50</sub> (at.%) composition. MA was performed under argon atmosphere using Fritsch Pulverisette 7 planetary ball mill equipped with hardened steel vial (80 mL) and balls (15 mm diameter). The disk speed rotation was  $\Omega = 400$  rpm. The ball-to-powder mass ratio was 23 : 1. To avoid excessive temperature increase, a milling time pause of 30 min was applied after each hour of milling. The powders were milled for several periods of time, that is, 0, 1, 3, 6, 24, 48, and 72 h.

**2.2. Characterization.** The milled powders were examined by X-ray diffraction (XRD) method, using X-ray Philips X, Pert diffractometer equipped with Cu-K<sub>α</sub> radiation source ( $\lambda_{Cu} = 0.15418$  nm). The phase analysis was performed by using ICDD (PDF-2, 2012) files. Both structural and microstructural parameters were determined from the refinements of XRD patterns using MAUD program (version 2.55) based on the Rietveld method [31].

Using the Rietveld refinement and Warren-Averbach method [24, 25] in the frame of MAUD software [31], a detailed analysis of XRD profiles can be performed leading to the determination of phase composition in addition to structural and microstructural parameters for each phase, such as lattice parameters ( $a, b, c$ ), the average crystallite size  $\langle L \rangle$ , microstrain  $\langle \epsilon^2 \rangle^{1/2}$ , and stacking fault probabilities (SFP).

The Rietveld method consists of simulating a pattern from simulated crystallographic model that is as close as possible to the measured pattern, which depends on analytical functions in order to characterize the microstructure of powders and determine  $\langle L \rangle$ ,  $\langle \epsilon^2 \rangle^{1/2}$ , and SFP.

The structural refinement method uses the minimization technique of least squares making it possible to approach the experimental pattern from a starting structural model. The minimized function, or residue, is written:

$$M = \sum_i w_i \cdot (y_i - y_{ic})^2, \quad (1)$$

where  $y_i$  and  $y_{ic}$  are, respectively, the observed and calculated intensities;  $w_i$  is the weight associated with the intensity  $y_i$ . For refinements by least square method,  $w_i$  is taken equal to  $1/y_i$ .

From a structural model, each contribution  $y_{ci}$  is obtained by the combination of different Bragg contributions and continuous background:

$$y_{ci} = y_{bi} + \sum_k I_k \phi_k, \quad (2)$$

where  $I_k$  is the integrated intensity of the reflection,  $\phi_k$  is the profile shape function, and  $y_{bi}$  a polynomial function fitting the background.

The integrated intensity of the reflection is calculated according to certain structural and geometric parameters:

$$I = S_c |F_k|^2 m_k \frac{(L_p)}{(V_c)^2}, \quad (3)$$

where  $S_c$  is the scale factor,  $F_k$  is the structure factor inclusive of Debye-Waller factor and site occupancy,  $m_k$  is the multiplicity of  $(hkl)$  reflection,  $L_p$  is the usual Lorentz-polarization factor, and  $V_c$  is the cell volume.

The profile shape function is the result of the convolution of instrumental and sample broadenings:

$$\phi_k = \phi^S \otimes \phi^I, \quad (4)$$

where  $\phi^S$  is the sample broadening and  $\phi^I$  is the instrumental broadening. The latter can be written as follows:

$$\phi^I = S \otimes A, \quad (5)$$

where  $S$  and  $A$  are, respectively, the symmetric and asymmetric components of the instrumental profile, determined for particular geometry of the diffractometer. The asymmetric component is given by

$$A = \exp[-a_s |2\theta - 2\theta_0| \tan(2\theta_0)], \quad (6)$$

where  $a_s$  is the asymmetry parameter and  $\theta_0$  is the Bragg angle of  $K_{\alpha 1}$  peak.

The Pseudo-Voigt function is defined as the contribution of a pure Lorentzian and a pure Gaussian (which will be corrected for the asymmetry of the peaks):

$$pV(2\theta_i) = \sum I_{nt} [\eta L(2\theta_i) + (1 - \eta) G(2\theta_i)], \quad (7)$$

where  $I_{nt}$  is the scale parameter of the  $pV$  function,  $\eta$  is the Gaussianity of X-ray peaks, and  $L(2\theta_i)$  and  $G(2\theta_i)$  are Gaussian and Lorentzian components, respectively:

$$G(2\theta_i) = I_0 \exp \left[ -\ln 2 \left( \frac{2\theta - 2\theta_0}{\text{FWHM}} \right)^2 \right], \quad (8)$$

$$L(2\theta_i) = I_0 \left[ 1 + \left( \frac{2\theta - 2\theta_0}{\text{FWHM}} \right)^2 \right]^{-n} \quad n = 1; 1.5; 2,$$

where  $2\theta_0$  is peak position,  $I_0$  is the peak intensity, and FWHM is the full-width at half-maximum of reflections.

The FWHM is given by the Caglioti formula [32]:

$$\text{FWHM} = \sqrt{U \cdot \tan^2 \theta + V \cdot \tan \theta + W} \quad (9)$$

where  $U$ ,  $V$ , and  $W$  are coefficients of quadratic polynomial or the coefficients of Caglioti.

The sample broadening  $\phi^S$  is the convolution of broadening due to the finite size of crystallites  $\langle L \rangle$ , the r.m.s microstrain  $\langle \epsilon^2 \rangle^{1/2}$ , and planar defects expressed in terms of stacking faults probability (SFP):

$$\text{SFP} = [1.5(\alpha' + \alpha'') + \beta], \quad (10)$$

where  $\alpha'$ ,  $\alpha''$  are the intrinsic and extrinsic deformation faults, respectively, and  $\beta$  is the twin faults.

The Delft model for sample broadening gives the integral breadths for the Gaussian and Lorentzian components:

$$\beta_G = 4 \langle \epsilon^2 \rangle^{1/2} \tan \theta \quad (11)$$

$$\beta_L = \frac{\lambda}{L_{\text{eff}} \cos \theta}.$$

$L_{\text{eff}}$  is an effective size computed from the crystallite size  $\langle L \rangle$  and  $\lambda$  is the radiation wavelength.

The MAUD software is based on the Rietveld method combined with a Fourier analysis. The detailed analysis was performed considering Fourier coefficients  $A_L$ ; after Stoke's corrections the size coefficients  $A_L^S$  and distortion coefficients  $A_L^D$ , which are related to  $A_L$  in the following equation:

$$A_L = A_L^D A_L^S, \quad (12)$$

were separated from the log plot of  $A_L$  with the square root of the quadratic sum of the Miller indices  $h_0^2$  where [33]

$$h_0^2 = h^2 + k^2 + l^2. \quad (13)$$

The reflections affected by stacking faults correspond to peaks satisfying the conditions:

$$h + k + l \neq 3n \quad (n \text{ is an integer}) \text{ for FCC structure} \quad (14)$$

$$h - k \neq 3n \quad (l \text{ even or odd}) \text{ for HCP structure.}$$

The microstructural parameters like effective size,  $L_{\text{eff}}$ , and the r.m.s. microstrain  $\langle \epsilon^2 \rangle^{1/2}$  are related, respectively, to the initial slope of  $A_L^S$  with  $L$  and slope of  $\log A_L$  with  $h_0^2$ :

$$-\left(\frac{dA_L^S}{dL}\right)_{L \rightarrow 0} = \frac{1}{L_{\text{eff}}}, \quad (15)$$

$$A_L^D = \exp\left(\frac{-2\pi^2 L^2 \langle \epsilon^2 \rangle^{1/2} h_0^2}{a^2}\right),$$

where  $L$  denotes a normal length to the reflecting planes.

The SFP like intrinsic  $\alpha'$ , extrinsic  $\alpha''$ , and deformation twin fault probability  $\beta$  were evaluated through the following relation:

$$\frac{1}{L_{\text{eff}}} = \frac{1}{L} + \frac{1.5(\alpha' + \alpha'') + \beta}{ah_0(u+b)} \sum_b |\pm L_0|, \quad (16)$$

where  $a$  is the lattice parameter,  $u$  is unbroadened by faulting,  $b$  is the number of reflections broadened, and  $L_0$  is the third coordinate replacing  $(hkl)$  indices ( $L_0 = h + k + l$ ) [33].

Peak asymmetry is obtained by measuring the intensity value on either side of the peak at two positions which are equidistant from the peak center ( $y_1$  and  $y_2$ ) and derived from the extrinsic deformation and twin faulting probabilities. The mathematical expression for asymmetry is evaluated as follows:

$$y_2 - y_1 = \frac{2A(4.5\alpha'' + \beta)}{c_2 x_2 \sqrt{3}\pi(u+b)} \sum (\pm) \frac{L_0}{|L_0|}, \quad (17)$$

where the coefficient  $c_2$  depends on the peak  $2\theta_0$  position:

$$c_2 = 1 + \left\{ \frac{\lambda}{4\pi L_{\text{eff}} [\sin(\theta_0 - x_2) - \sin\theta_0]} \right\}^2, \quad (18)$$

where  $A$  is the area of the peak,  $y_1$  is the peak intensity in the diffraction angle  $(\theta_0 + x_2)$ , and  $\theta_0$  is the completely symmetrical profile center [31].

The peak shift can be written, in terms of intrinsic and extrinsic deformation faulting probability, as follows [33]:

$$\Delta(2\theta)^\circ = \frac{90\sqrt{3}(\alpha' + \alpha'') \tan\theta}{\pi^2 h_0^2 (u+b)} \sum_b (\pm L_0). \quad (19)$$

From the values of lattice parameters, crystallite size, and microstrain, the dislocations density ( $\rho$ ) can be calculated using the following formula:

$$\rho = 2\sqrt{3} \frac{\langle \epsilon^2 \rangle^{1/2}}{\langle L \rangle B_v}, \quad (20)$$

where  $B_v$  is Burgers vector, which is equal to  $a\sqrt{6}/3$  for the hexagonal close-packed (HCP) structure and  $a\sqrt{2}/2$  for the face-centered cubic (FCC) structure.

The calculated profile yields scaling factors for each phase to fit the intensity of the observed pattern. These scale factors

are related to the respective relative weight fractions by the following equation [34]:

$$W_i = \frac{S_i (ZMV)_i}{\sum_{k=1}^n S_k (ZMV)_k}, \quad (21)$$

where  $Z$  is the number of formula units in the unit cell,  $M$  is the molecular mass of the formula unit,  $V$  is the unit cell volume,  $S$  is the Rietveld scale factor, and  $W_i$  is the weight fraction of phase  $i$ : the index “ $k$ ” in the summation covering all phases that are included in the model [34].

The standard procedure is to determine the amorphous fraction by the internal standard method. The amount of the amorphous phase is obtained as the complement to one of the total amounts of crystalline phases [31]. The weight percentage of the amorphous phase in a sample can be given by the following relationship [35]:

$$W_a = \frac{1}{1 - \frac{W_S}{W_R}} \left(1 - \frac{W_S}{W_R}\right), \quad (22)$$

where  $W_a$  is the amorphous fraction,  $W_S$  is the weighted internal standard fraction, and  $W_R$  is the refined fraction of the internal standard.

After adjusting the parameters of the instrument, the peak positions are corrected by successive refinements to eliminate systematic errors by taking into account the errors of the angular offset ( $\Delta 2\theta$ ) and the displacement of the sample. The background is adjusted by a polynomial of degree (2 to 5), for the first milling time. On the other hand, for longer milling times, the increase in the intensity of the background requires the use of higher degree polynomials. Then, the parameters of the crystal structure are refined, namely, the crystal parameters, the atomic positions, the Debye-Waller factor, and the percentage of phases. In the last step, we proceed to the refinement of crystallite size  $\langle L \rangle$ , microstrain  $\langle \epsilon^2 \rangle^{1/2}$ , and the probability of all three types of planes defects  $\alpha'$ ,  $\alpha''$ , and  $\beta$ .

To evaluate the refinement, several factors have been introduced in order to know the agreement between calculated and observed models [34].

The minimization was carried out by using the reliability index parameter,  $R_{wp}$  (weighted residual error), and  $R_{\text{exp}}$  (the expected error) defined as follows [27]:

$$R_{wp} = \left[ \frac{\sum_{i=1}^N (y_i - y_{ic})^2}{\sum_{i=1}^N y_i (2\theta_i)} \right]^{1/2}, \quad (23)$$

$$R_{\text{exp}} = \left[ \frac{N - P}{\sum_{i=1}^N y_i (2\theta_i)} \right]^{1/2},$$

where  $N$  and  $P$  are the number of experimental points and the number of fitting parameters, respectively.

It is possible to calculate a statistical parameter, which must tend towards the unity for a successful refinement; the goodness of fit “ $\chi^2$ ” is defined as the ratio between  $R_{wp}$  and  $R_{\text{exp}}$ :

$$\chi^2 = \frac{R_{wp}}{R_{\text{exp}}}. \quad (24)$$

The profile refinements continue until convergence is reached; the value of the quality factor  $\chi^2$  (GOF) is approaching one.

### 3. Results and Discussion

**3.1. Structural Analysis.** The X-ray diffraction (XRD) patterns of  $\text{Ni}_{50}\text{Ti}_{50}$  powders (0, 1, 3, 6, 12, 24, 48, and 72 h), shown in Figure 4, clearly indicate that MA introduces significant changes. There is a gradual peaks' broadening with a decrease in peaks' intensity as a function of the milling time, demonstrating the great impact of milling on the crushed starting elemental Ni and Ti starting powders, which can be associated with several processes occurring progressively [36]:

- (i) particles (grains) refinement (reduction of crystallite size);
- (ii) introduction of crystalline defects (interstices, dislocations, and grain boundaries);
- (iii) increase in the rate of microdeformations (large amount of energy);
- (iv) fragmentation of crystallites and/or effect of atomic disorder.

The as-mentioned phenomena result from welding and disordering effects, occurring because of repeated collisions (ball-powder-ball and ball-powder-wall of bowl).

The overlapping of XRD reflections arising from different phases results in an enlargement of peaks' width accompanied with a slight shift towards lower angles, indicating a slight increase in interatomic distances leading to unit cell expansion.

After few hours of milling, one can see the appearance of halo around  $35\text{--}50^\circ$ , which overlaps with reflections belonging to HCP-Ti and FCC-Ni. This can be attributed to the formation of an amorphous phase, which is explained by the significant structural disorder induced by the severe plastic deformations occurring during milling process.

Figure 5 shows the refined XRD patterns for elemental Ni and Ti powders, based on initial structural models: (i) face-centered cubic (FCC) for Ni with lattice parameter  $a = 0.3524$  nm; (ii) hexagonal close-packed (HCP) for Ti with lattice parameters  $a = 0.2952$  nm and  $c = 0.4686$  nm. All the results are reported in Table 1.

The best Rietveld refinements of XRD patterns (1, 3, and 6 h) were obtained with three components: FCC-Ni, HCP-Ti, and an amorphous phase (Figures 6(a), 6(b), and 6(c)). The nanometer scaled diffusion couples are produced by high energy mechanical milling which involves fracture and cold-welding of milled powders. Thus, the atomic diffusivity is improved through the creation of a large amount of structural defects. As a result, metastable phases may form at early stage of the milling by solid-state reaction (SSR) process.

After 12 h of milling, the diffraction peaks of elemental FCC-Ni, HCP-Ti, and the amorphous phase remain while new diffraction peaks related to NiTi-martensitic (Figure 6(d)) emerge.

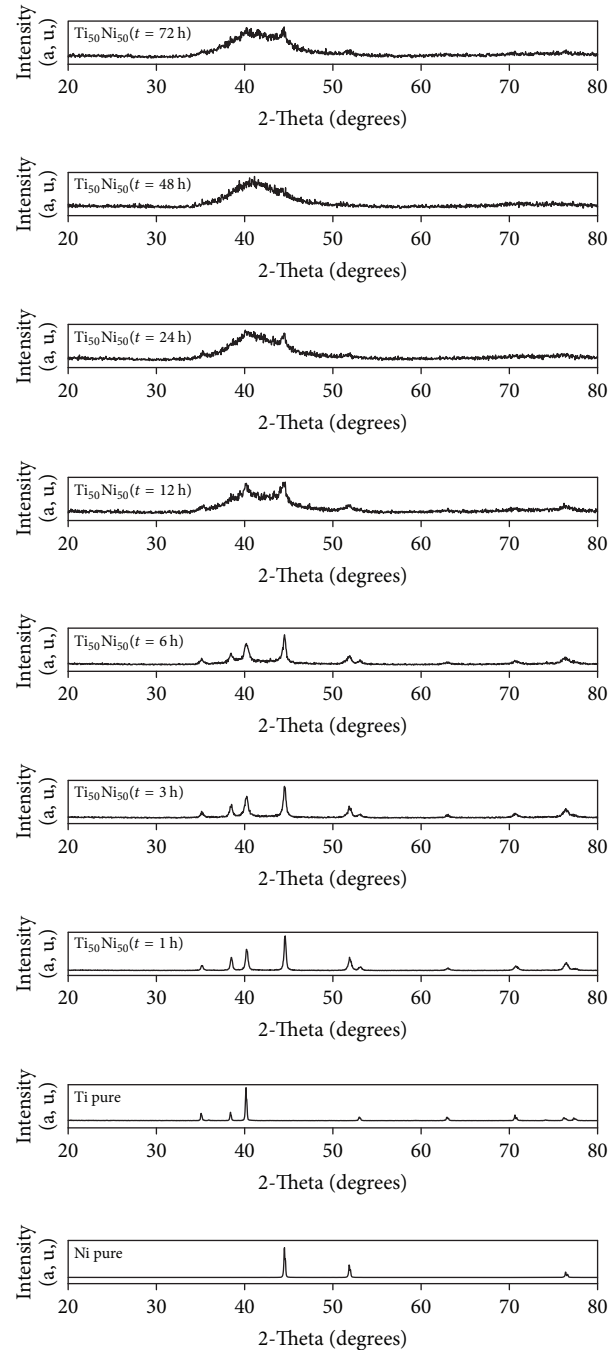
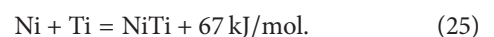


FIGURE 4: XRD patterns of the  $\text{Ni}_{50}\text{Ti}_{50}$  powders at different milling time.

Further milling up to (24 h), leads to a complete disappearance of HCP-Ti peaks associated with the formation of NiTi-austenitic (Figure 6(e)), while Ni-SS remains present with small amount (15.38%). Furthermore, it is well-known that the crystallite size decreases with the increase of negative mixing enthalpy ( $\Delta H$ ) [36]. In addition, NiTi phase could be the product of the reaction between Ni and Ti due to their negative mixing enthalpy ( $\Delta H = -67$  kJ/mol) [37, 38]:



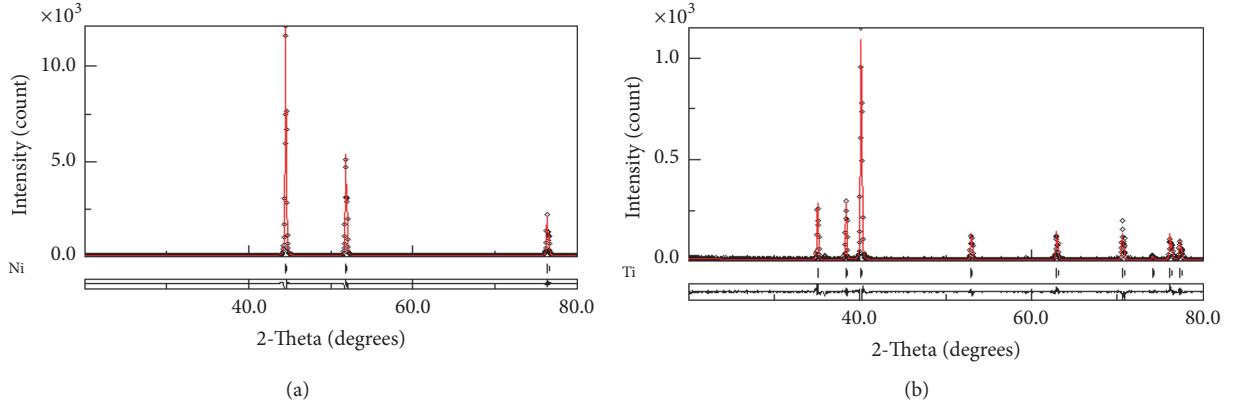


FIGURE 5: Rietveld refinements for XRD pattern of (a) Ni (GOF = 1.54) and (b) Ti (GOF = 1.11).

TABLE 1: Structural and microstructural properties of unmilled Ni and Ti using the Rietveld refinements.

Microstructural properties	Element	
	Nickel (Ni)	Titanium (Ti)
Crystal structure	FCC	HCP
Space group	Fm-3m	P63/mmc
Cell parameters (nm)	$a = 0.3524$	$a = 0.2952$ $b = 0.4686$
Atom positions	$x: 3.65141 \cdot 10^{-4}$ $y: -8.8563 \cdot 10^{-5}$ $z: -5.9118 \cdot 10^{-5}$	$x: 0.3333$ $y: 0.6667$ $z: 0.2500$
Occupancy	1.0001	1.0000
Crystallite size (nm)	318.4175	241.2283
Microstrain (%)	$3.1758 \cdot 10^{-4}$	$4.5954 \cdot 10^{-4}$
Stacking faults probability (SFP) (%)	$1.5832 \cdot 10^{-4}$	0.1744
Dislocations density ( $\times 10^{16} \text{ m}^{-2}$ )	0.0014	0.0027

Beyond 48 h of milling, XRD patterns reveal the same phases, NiTi-austenite (B2) and NiTi-martensite (B19'), but with the dominance of the amorphous phase (Figures 6(f) and 6(g)) having a relative proportion of about 89.24%.

In order to investigate the phase's stabilities during mechanical milling, we calculated the phase proportions of the identified phases as a function of milling time. The results obtained are shown in Figure 7. Accordingly, the milling process was divided into four main stages (I, II, III, and IV) as shown in Figure 7.

In the first stage I (0-1 h), a decrease in the proportions of Ti and Ni was observed, which may be due to the mutual diffusion and to the formation of amorphous phase and solid solutions FCC-Ni (Ti) and HCP-Ti (Ni).

During the second stage II (1-12 h), which represents a postformation of amorphous phase, we note that Ti-SS and Ni-SS ratios decrease inversely to the proportion of the amorphous phase.

Then, in the third stage III (12-24 h), the percentage of initial Ni-SS continues to decrease, meanwhile Ti-SS has disappeared completely, thus leading to the continuous increase in the amount of the amorphous phase and the formation of martensitic phase. The formation of martensitic phase may

be due to the negative mixing enthalpy [37]. The complete transformation of the severely deformed phases into an amorphous structure is achieved upon further milling, through the mechanically enhanced solid-state amorphisation, which requires the existence of chemical disordering, point defects, vacancies, interstitials, lattice defects, and dislocations.

The fourth and final stage IV (24-72 h) is characterized by the emergence of new NiTi-austenite phase, while the initial Ni-SS entirely disappears favoring also to the formation of NiTi-austenite. The continuous increase in the proportion of the amorphous phase can be explained evidently along with the reduction in the amount of NiTi-martensite.

After 48 h, the fraction of the amorphous phase decreases due to its crystallization into more stable crystalline phases (NiTi-austenite and NiTi-martensite), which may be attributed to strain energy and the temperature increase during MA due to severe plastic deformations as reported by Amini et al. [19]. However, the amorphous phase is predominant with a relative proportion of about 89.23%.

Indeed, the heavily plastic deformations induce strong distortion of the unit cell structures hence becoming less crystalline. The powdered particles are subjected to continuous defects that lead to a gradual change in the free energy

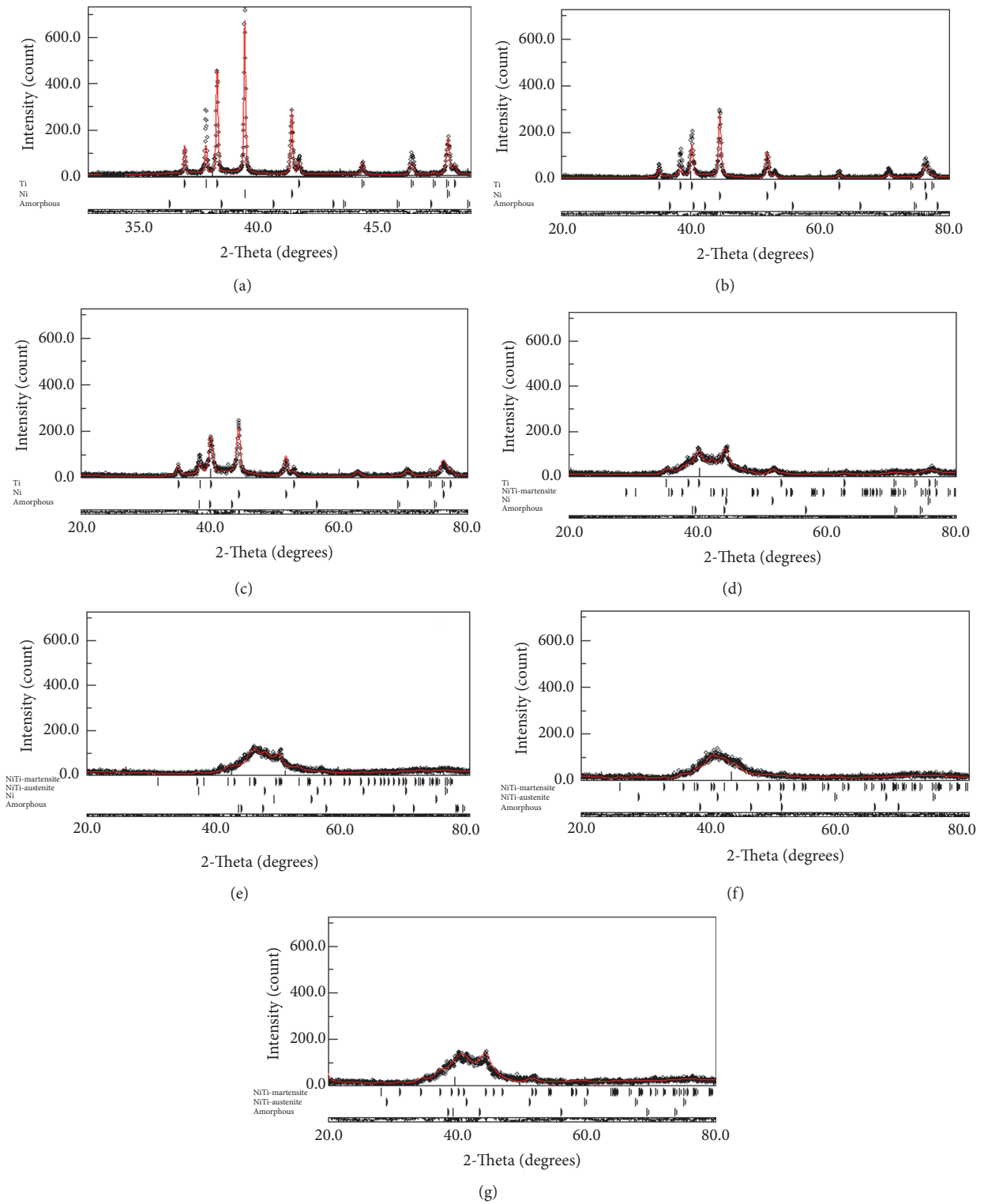


FIGURE 6: Rietveld refinements of XRD patterns of the milled powders for (a) 1 h (GOF = 1.41), (b) 3 h (GOF = 1.45), (c) 6 h (GOF = 1.43), (d) 12 h (GOF = 1.22), (e) 24 h (GOF = 1.20), (f) 48 h (GOF = 1.19), and (g) 72 h (GOF = 1.23).

TABLE 2: Lattice parameters of Ni, Ti, NiTi-austenite, and NiTi-martensite as function of milling time.

Milling time (h)	Ni		Ti		NiTi-austenite		NiTi-martensite	
	<i>a</i> (nm)	<i>a</i> (nm)	<i>b</i> (nm)	<i>a</i> (nm)	<i>a</i> (nm)	<i>b</i> (nm)	<i>c</i> (nm)	
0	0.3524	0.2952	0.4686	/	/	/	/	
1	0.3519	0.2947	0.4677	/	/	/	/	
3	0.3527	0.2953	0.4687	/	/	/	/	
6	0.3534	0.2956	0.4687	/	/	/	/	
12	0.3560	0.2979	0.4708	/	0.4780	0.4225	0.2978	
24	0.3574	/	/	0.3045	0.4134	0.4576	0.2953	
48	/	/	/	0.3155	0.4858	0.5110	0.2798	
72	/	/	/	0.3134	0.4687	0.4238	0.2942	

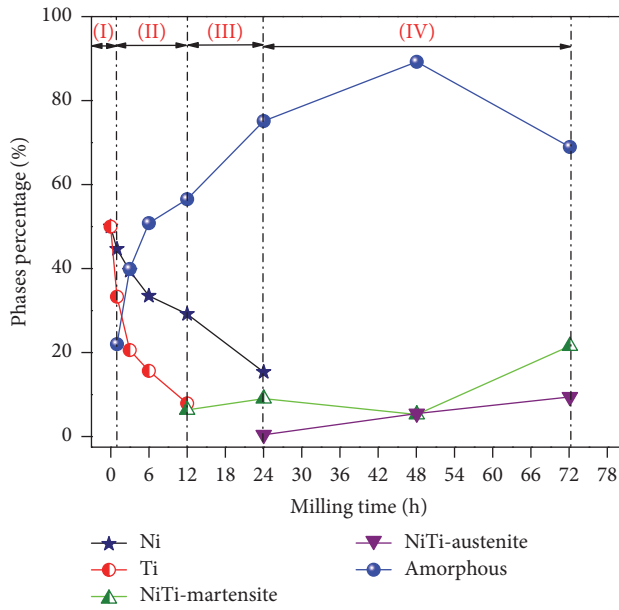


FIGURE 7: Evolution of the proportions of the identified phases as a function of milling time.

of the crystalline phases compared to the amorphous phase resulting into disorder in atomic arrangement.

**3.2. Crystallite Size and Microstrain.** A diffraction peak broadening, observed with increasing milling time, is usually associated with grain size reduction and increase of internal strain. The variation in the average crystallite size  $\langle L \rangle$  and microstrain  $\langle \epsilon^2 \rangle^{1/2}$  obtained from Rietveld refinements is plotted as a function of milling time in Figure 8.

In the early stage of milling, one can observe an important decrease of the crystallite size reaching 7 nm (24 h) and 29 nm (12 h) for Ni-SS and Ti-SS, respectively. It is also evident that the reduction in Ni-SS crystallite size is faster than Ti-SS, which is probably related to its smaller initial particle size of Ni ( $<45 \mu\text{m}$ ) compared to Ti ( $<150 \mu\text{m}$ ) [38].

But in the second stage, after 24 h, the crystallite size becomes less dependent on the milling time. This can be explained by the fact that mechanical energy delivered during milling is not sufficient to plastically deform the two phases

NiTi-austenite and NiTi-martensite. The average crystallite size of NiTi-martensite after 72 h is of about 19 nm while that of NiTi-austenite reaches 42 nm (Figure 8(a)). The reduction in crystallite size is mainly due to severe deformations of powders during the milling, as well as the increase in probability of nucleation sites during crystallization, provided by higher defects density [36].

The as-obtained values of the crystallite size are in good agreement with the values previously reported on binary alloys prepared by MA [20, 28, 29].

From Figure 8(b), it is clear that the internal microstrain  $\langle \epsilon^2 \rangle^{1/2}$  increases with increasing milling time. Thus during the first stage of milling,  $\langle \epsilon^2 \rangle^{1/2}$  of Ni-SS and Ti-SS reaches about 0.7% and 1.16% after 12 h, respectively. The increase of the microstrain can be due to the increase of dislocations density induced by severe plastic deformations [28]. For NiTi-martensite,  $\langle \epsilon^2 \rangle^{1/2}$  increases to about 0.9%, after 48 h, and then decreases; this behavior may be explained by the fact that, beyond this time, the crystallite size reaches a stationary value.

It is important to mention that NiTi-austenite is characterized by higher microstrain comparatively to NiTi-martensite, which may be due to a high concentration of stacking faults and a high dislocations density. In fact, actually, the austenite phase is metastable at room temperature and becomes unstable when an external mechanical or thermal energy is introduced. Generally, the values of microstrain achieved during milling for similar systems are around 1.5% [18].

**3.3. Lattice Parameters.** Table 2 shows the variation of lattice parameters of Ni, Ti, NiTi-austenite, and NiTi-martensite for each milling time as obtained from Rietveld analysis. The decrease of the lattice parameters of Ni and Ti after 1 h of milling is probably due to the compressive forces caused by collisions [27], and therefore reducing the distance between neighboring atoms. It can be noticed that Ni and Ti lattice parameters increase with milling time reaching 0.3574 nm, after 24 h, and  $a = 0.2979$  nm and  $b = 0.4708$  nm, after 12 h of milling, respectively. This can be attributed to the severe plastic deformations and accumulation of large amount of structural defects such as stacking faults, grain boundaries, and enhanced dislocations density during the milling process [23].

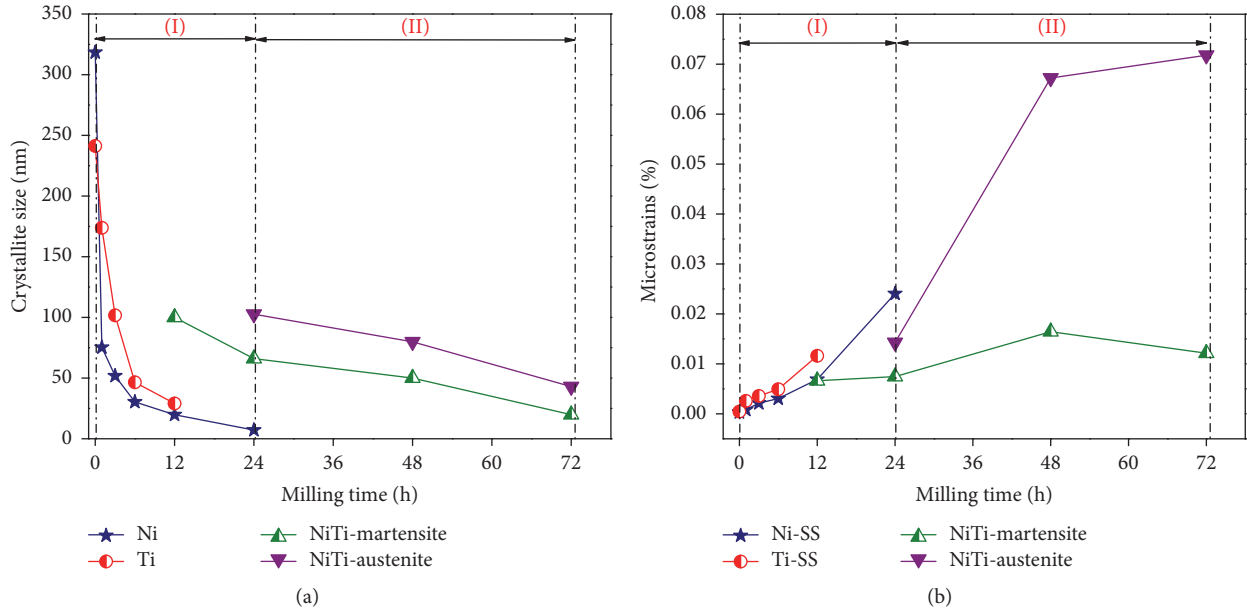


FIGURE 8: Evolution of (a) average crystallite size  $\langle L \rangle$  and (b) microstrain  $\langle \epsilon^2 \rangle^{1/2}$  as a function of milling time.

For the austenite phase, the lattice parameter increases up to 48 h and then remains nearly stationary until 72 h where it reaches a value of 0.3134 nm. The relative deviation of the lattice parameter ( $\Delta a/a_0$ ) of the austenite phase after 48 hours of milling is 3.96% which is high compared to the relative deviation of the lattice parameter of martensitic phase  $\Delta a/a_0 = 1.397\%$ ,  $\Delta b/b_0 = 0.663\%$ , and  $\Delta c/c_0 = 1.962\%$ . This relatively high value can be associated with the severe plastic deformations, which introduces different types of defects such as dislocations, grain boundaries, gaps, and stacking faults and it can be also explained by the formation of a nonstoichiometric composition of the austenite phase.

**3.4. Dislocations Density.** The variation of the dislocations density can be associated with the ball-to-powder mass ratio that characterizes the collision number, the energy impact, and the number of defects introduced within the lattice.

Figure 9 illustrates the evolution of dislocations density of Ni and Ti as a function of milling time and can be divided into two stages:  $\rho_I$  (0–12 h) and  $\rho_{II}$  (12–24 h). It is obvious that  $\rho$  increases slightly in the first stage  $\rho_I$  from about  $0.0014 \times 10^{16}$  to  $0.4791 \times 10^{16} \text{ m}^{-2}$  for Ni-SS and  $0.0027 \times 10^{16} \text{ m}^{-2}$  to  $0.5691 \times 10^{16} \text{ m}^{-2}$  for Ti-SS. The as-obtained  $\rho$  values are comparable to the values of dislocations density limit in metals achieved by plastic deformations ( $10^{13} \text{ m}^{-2}$  for screw dislocations and  $10^{16} \text{ m}^{-2}$  for edge dislocations) [39]. During the final stage  $\rho_{II}$ , for Ni-SS, the dislocations density increases considerably up to  $2.6851 \times 10^{16} \text{ m}^{-2}$  with the disappearance of Ti. This increase as compared to the first stage  $\rho_I$ , could be due to the formation of NiTi-martensite phase. Indeed, the Ti radius is slightly larger than that of Ni ( $R_{\text{Ti}} = 0.176 \text{ nm} > R_{\text{Ni}} = 0.149 \text{ nm}$ ), so the diffusion of Ti into Ni leads to the distortion of Ni crystal structure and hence further increase in the dislocations density. The as-obtained values of the

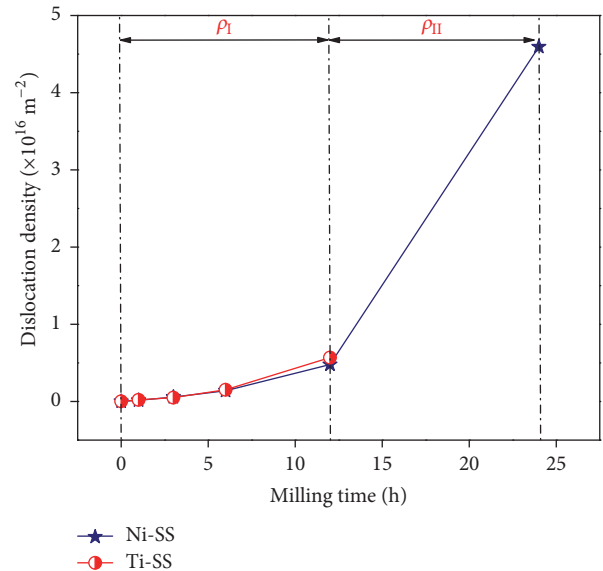


FIGURE 9: Evolution of dislocations density of Ni and Ti as a function of milling time.

dislocations density in the present work are comparable to the values observed in the binary  $\text{Co}_{50}\text{Ni}_{50}$  alloy synthesized by high energy ball milling [28].

**3.5. Stacking Faults.** Heavy deformations introduce stacking faults along (111) planes in FCC metals and alloys. Stacking faults can also be introduced in the basal (0001) or prismatic (10 $\bar{1}$ 0) planes of the hexagonal close backed alloys. These faults can cause anomalous ( $hkl$ ) dependent peak broadening in the X-ray diffraction patterns [18].

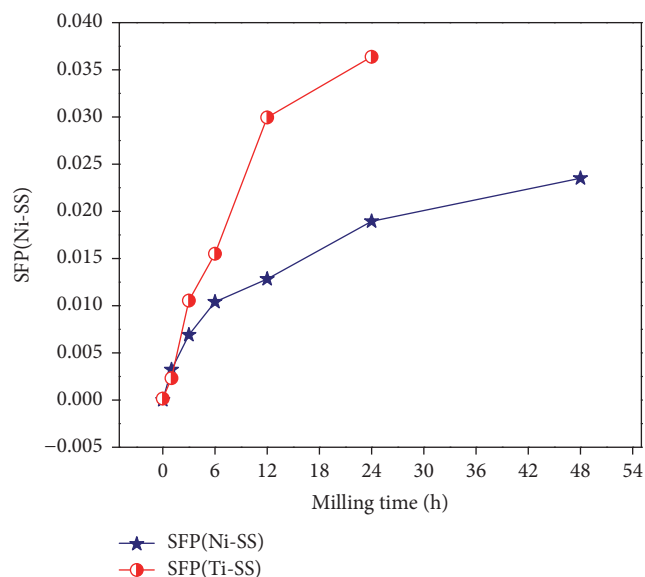


FIGURE 10: Evolution of stacking fault probability for Ni and Ti as a function of milling time.

Figure 10 shows the variation of stacking faults probability (SFP) of HCP-Ti and FCC-Ni as deduced from the Rietveld refinements of XRD patterns of Ni and Ti. In both Ni and Ti crystal structures, two different types of stacking faults can be found, namely, deformation and twin stacking faults. It can be noticed that, for both HCP-Ti and Ni-FCC, SFP increases with increasing milling time; reaching after 24 h a higher value of 0.0364 (HCP-Ti) compared to 0.0189 (FCC-Ni). The increase of SFP for both Ni and Ti with extensive milling time reflects an important increase in the dislocations density (Figure 9). It has been noticed that twinning and deformation stress depend on the initial crystallite size and milling intensity [18].

The parameter  $1/(sfp)$  indicates the average number of compacted layers between two stacking faults, either deformation or twin-type, according to Warren's formulae [40]. In fact, there are 27 and 43 ordered planes between the two consecutive stacking faults in HCP-Ti and FCC-Ni after 24 and 48 h of milling, respectively. As it is clear, the values of the average number of compacted layers between two stacking faults in HCP-Ti(Ni) are found to be higher compared to FCC-Ni(Ti) and thus can explain that Ti facilitates the formation of the amorphous phase more than Ni. Meanwhile, Ni contributes to the formation of martensitic and austenitic phases.

#### 4. Conclusion

A mixture of Ni and Ti elemental powders with a nominal composition  $Ni_{50}Ti_{50}$  was mechanically alloyed in a planetary ball mill under argon atmosphere. The final products were nanocrystalline NiTi-martensite (B19) and NiTi-austenite (B2) phases with an average crystallite size in the range of a few nanometers (19 nm~42 nm) with a large internal strain (1.02%~1.48%) and a dominant amorphous phase (89 wt.%).

The induced heavy plastic deformations lead to crystallite size refinement and accumulation of structural and point defects, resulting in a significant contribution of stacking faults (SFs) resulting in the destabilization of crystalline structures. As a consequence, we demonstrated that mechanical alloying is a nonequilibrium process, where phase composition and transformation of binary NiTi can be modified from that predicted using thermodynamic equilibrium phase diagram.

#### Conflicts of Interest

The authors declare that there are no conflicts of interest.

#### References

- [1] A. Tuissi, G. Rondelli, and P. Bassani, "Plasma Arc Melting (PAM) and Corrosion Resistance of Pure NiTi Shape Memory Alloys," *Shape Memory and Superelasticity*, vol. 1, no. 1, pp. 50–57, 2015.
- [2] J. Witkowska, J. Kaminski, T. P. Iocinski et al., "Corrosion resistance of NiTi shape memory alloy after hybrid surface treatment using low-temperature plasma," *Vacuum*, vol. 137, pp. 92–96, 2017.
- [3] C. H. Ng, R. Nanxi, W. C. Law et al., "Enhancing the cell proliferation performance of NiTi substrate by laser diffusion nitriding," *Surface Coatings Technology* 309, pp. 59–66, 2017.
- [4] J. Sevcikova and M. Pavkova Goldbergova, "Biocompatibility of NiTi alloys in the cell behaviour," *BioMetals*, vol. 30, no. 2, pp. 163–169, 2017.
- [5] R. Piquard, A. D'Acunto, P. Laheurte, and D. Dudzinski, "Micro-end milling of NiTi biomedical alloys, burr formation and phase transformation," *Precision Engineering*, vol. 38, no. 2, pp. 356–364, 2014.
- [6] S. A. Thompson, "An overview of nickel-titanium alloys used in dentistry," *International Endodontic Journal*, vol. 33, pp. 297–310, 2000.
- [7] T. Saito, T. Yokoyama, and A. Takasaki, "Hydrogenation of TiNi shape memory alloy produced by mechanical alloying," *Journal of Alloys and Compounds*, vol. 509, no. 2, pp. S779–S781, 2011.
- [8] L. A. L. Pavón, E. L. Cuellar, C. Ballesteros, A. T. Castro, A. M. De La Cruz, and C. J. De Araújo, "Nanoparticles from Cu-Zn-Al shape memory alloys physically synthesized by ion milling deposition," *Materials Research*, vol. 15, no. 3, pp. 341–346, 2012.
- [9] M. Izadinia and K. Dehghani, "Structure and properties of nanostructured Cu-13.2Al-5.1Ni shape memory alloy produced by melt spinning," *Transactions of Nonferrous Metals Society of China*, vol. 21, no. 9, pp. 2037–2043, 2011.
- [10] Q. Dai, M. Asif warsi, J. Q. Xiao, and S. Ren, "Solution processed MnBi-FeCo magnetic nanocomposites," *Nano Research*, vol. 9, no. 11, pp. 3222–3228, 2016.
- [11] K. Y. Chiu, M. H. Wong, F. T. Cheng, and H. C. Man, "Characterization and corrosion studies of titania-coated NiTi prepared by sol-gel technique and steam crystallization," *Applied Surface Science*, vol. 253, no. 16, pp. 6762–6768, 2007.
- [12] T. Mousavi, F. Karimzadeh, and M. H. Abbasi, "Synthesis and characterization of nanocrystalline NiTi intermetallic by mechanical alloying," *Materials Science and Engineering: A Structural Materials: Properties, Microstructure and Processing*, vol. 487, no. 1-2, pp. 46–51, 2008.

- [13] M. H. Elahinia, M. Hashemi, M. Tabesh, and S. B. Bhaduri, "Manufacturing and processing of NiTi implants: a review," *Progress in Materials Science*, vol. 57, no. 5, pp. 911–946, 2012.
- [14] M. Karlik, P. Haušild, M. Klementová et al., "TEM phase analysis of NiTi shape memory alloy prepared by self-propagating high-temperature synthesis," *Advances in Materials and Processing Technologies*, vol. 3, no. 1, pp. 58–69, 2016.
- [15] T. Kurita, H. Matsumoto, K. Sakamoto, and H. Abe, "Transformation behavior of shock-compressed Ni<sub>48</sub>Ti<sub>52</sub>," *Journal of Alloys and Compounds*, vol. 400, no. 1-2, pp. 92–95, 2005.
- [16] M. Akmal, A. Raza, M. M. Khan, M. I. Khan, and M. A. Hussain, "Effect of nano-hydroxyapatite reinforcement in mechanically alloyed NiTi composites for biomedical implant," *Materials Science and Engineering C: Materials for Biological Applications*, vol. 68, pp. 30–36, 2016.
- [17] M. Karolus and J. Panek, "Nanostructured Ni-Ti alloys obtained by mechanical synthesis and heat treatment," *Journal of Alloys and Compounds*, vol. 658, pp. 709–715, 2016.
- [18] C. Suryanarayana, "Structure and properties of ultrafine-grained MoSi<sub>2</sub> + Si<sub>3</sub>N<sub>4</sub> composites synthesized by mechanical alloying," *Materials Science and Engineering: A Structural Materials: Properties, Microstructure and Processing*, vol. 479, no. 1-2, pp. 23–30, 2008.
- [19] R. Amini, F. Alijani, M. Ghaffari, M. Alizadeh, and A. K. Okyay, "Formation of B19', B2, and amorphous phases during mechano-synthesis of nanocrystalline NiTi intermetallics," *Powder Technology*, vol. 253, pp. 797–802, 2014.
- [20] B. Avar, "Structural, thermal and magnetic characterization of nanocrystalline Co<sub>65</sub>Ti<sub>25</sub>W<sub>5</sub>B<sub>5</sub> powders prepared by mechanical alloying," *Journal of Non-Crystalline Solids*, vol. 432, pp. 246–253, 2016.
- [21] F. Hadeif, A. Otmani, A. Djekoun, and J. M. Grenèche, "Structural and microstructural study of nanostructured Fe<sub>50</sub>Al<sub>40</sub>Ni<sub>10</sub> powders produced by mechanical alloying," *Materials Characterization*, vol. 62, no. 8, pp. 751–759, 2011.
- [22] G. K. Williamson and W. H. Hall, "X-ray line broadening from filed aluminium and wolfram," *Acta Metallurgica et Materialia*, vol. 1, no. 1, pp. 22–31, 1953.
- [23] J. I. Langford, "The accuracy of cell dimensions determined by Cohen's method of least squares and the systematic indexing of powder data," *Journal of Applied Crystallography*, vol. 6, no. 3, pp. 190–196, 1973.
- [24] B. E. Warren and B. L. Averbach, "The Effect of Cold-Work Distortion on X-Ray Patterns," *Journal of Applied Physics*, vol. 21, no. 6, pp. 595–599, 1950.
- [25] H. M. Rietveld, "A profile refinement method for nuclear and magnetic structures," *Journal of Applied Crystallography*, vol. 2, pp. 65–71, 1969.
- [26] P. Pourghahramani, E. Altin, M. R. Mallebakam, W. Peukert, and E. Forssberg, "Microstructural characterization of hematite during wet and dry millings using Rietveld and XRD line profile analyses," *Powder Technology*, vol. 186, no. 1, pp. 9–21, 2008.
- [27] H. Dutta, A. Sen, J. Bhattacharjee, and S. K. Pradhan, "Preparation of ternary Ti<sub>0.9</sub>Ni<sub>0.1</sub>C cermets by mechanical alloying: Microstructure characterization by Rietveld method and electron microscopy," *Journal of Alloys and Compounds*, vol. 493, no. 1-2, pp. 666–671, 2010.
- [28] N. Loudjani, N. Bensebaa, L. Dekhil, S. Alleg, and J. J. Suñol, "Structural and magnetic properties of Co<sub>50</sub>Ni<sub>50</sub> powder mixtures," *Journal of Magnetism and Magnetic Materials*, vol. 323, no. 23, pp. 3063–3070, 2011.
- [29] N. Loudjani, M. Benchiheub, and M. Bououdina, "Structural, Thermal and Magnetic Properties of Nanocrystalline Co<sub>80</sub>Ni<sub>20</sub> Alloy Prepared by Mechanical Alloying," *Journal of Superconductivity and Novel Magnetism*, vol. 29, no. 11, pp. 2717–2726, 2016.
- [30] M. B. Makhlof, T. Bachaga, J. J. Sunol, M. Dammak, and M. Khitouni, "Synthesis and characterization of nanocrystalline Al-20 at. % Cu powders produced by mechanical alloying," *Metals*, vol. 6, no. 7, article no. 145, 2016.
- [31] M. Bortolotti, L. Lutterotti, and G. Pepponi, "Combining XRD and XRF analysis in one Rietveld-like fitting," *Powder Diffraction*, vol. 32, no. S1, pp. S225–S230, 2017.
- [32] G. Caglioti, A. Paoletti, and F. P. Ricci, "Choice of collimators for a crystal spectrometer for neutron diffraction," *Nuclear Instruments*, vol. 3, no. 4, pp. 223–228, 1958.
- [33] B. E. Warren and B. L. Averbach, "The effect of cold-work distortion on x-ray patterns," *Journal of Applied Physics*, vol. 21, no. 6, pp. 595–599, 1950.
- [34] R. J. Hill, "Expanded use of the rietveld method in studies of phase abundance in multiphase mixtures," *Powder Diffraction*, vol. 6, no. 2, pp. 74–77, 1991.
- [35] R. Amini, M. J. Hadianfard, E. Salahinejad, M. Marasi, and T. Sritharan, "Microstructural phase evaluation of high-nitrogen Fe-Cr-Mn alloy powders synthesized by the mechanical alloying process," *Journal of Materials Science*, vol. 44, no. 1, pp. 136–148, 2009.
- [36] C. Suryanarayana, "Mechanical alloying and milling," *Progress in Materials Science*, vol. 46, no. 1-2, pp. 1–184, 2001.
- [37] B.-Y. Li, L.-J. Rong, and Y.-Y. Li, "Stress-strain behavior of porous Ni-Ti shape memory intermetallics synthesized from powder sintering," *Intermetallics*, vol. 8, no. 5-6, pp. 643–646, 2000.
- [38] W. Maziarz, J. Dutkiewicz, J. Van Humbeeck, and T. Czeppe, "Mechanically alloyed and hot pressed Ni-49.7Ti alloy showing martensitic transformation," *Materials Science and Engineering: A Structural Materials: Properties, Microstructure and Processing*, vol. 375-377, no. 1-2, pp. 844–848, 2004.
- [39] T. Bachaga, R. Daly, L. Escoda, J. J. Suñol, and M. Khitouni, "Amorphization of Al<sub>50</sub>(Fe<sub>2</sub>B)<sub>30</sub>Nb<sub>20</sub> mixture by mechanical alloying," *Metallurgical and Materials Transactions A: Physical Metallurgy and Materials Science*, vol. 44, no. 10, pp. 4718–4724, 2013.
- [40] J. Sort, J. Nogués, S. Suriñach, J. S. Muñoz, and M. D. Baró, "Correlation between stacking fault formation, allotropic phase transformations and magnetic properties of ball-milled cobalt," *Materials Science and Engineering: A Structural Materials: Properties, Microstructure and Processing*, vol. 375-377, no. 1-2, pp. 869–873, 2004.

## Research Article

# Dynamic Infrared Thermography of Nanoheaters Embedded in Skin-Equivalent Phantoms

K. A. López-Varela <sup>1</sup>, N. Cayetano-Castro,<sup>2</sup> E. S. Kolosovas-Machuca,<sup>3</sup> F. J. González <sup>3</sup>,  
F. S. Chiwo,<sup>3</sup> and J. L. Rodríguez-López <sup>1</sup>

<sup>1</sup>*División de Materiales Avanzados, Instituto Potosino de Investigación Científica y Tecnológica, A.C., Camino Presa San José 2055, Lomas 4ª Secc., 78216 San Luis Potosí, SLP, Mexico*

<sup>2</sup>*Nanoscience, Micro and Nanotechnology Center, National Polytechnic Institute, Av. Luis Enrique Erro s/n, Zacatenco, 07738 Mexico City, Mexico*

<sup>3</sup>*Coordinación para la Innovación y la Aplicación de la Ciencia y la Tecnología, Universidad Autónoma de San Luis Potosí, San Luis Potosí, SLP, Mexico*

Correspondence should be addressed to K. A. López-Varela; [karla.lopez@ipicyt.edu.mx](mailto:karla.lopez@ipicyt.edu.mx) and J. L. Rodríguez-López; [jlrdez@ipicyt.edu.mx](mailto:jlrdez@ipicyt.edu.mx)

Received 13 July 2017; Revised 1 November 2017; Accepted 5 December 2017; Published 14 January 2018

Academic Editor: Leszek A. Dobrzański

Copyright © 2018 K. A. López-Varela et al. This is an open access article distributed under the Creative Commons Attribution License, which permits unrestricted use, distribution, and reproduction in any medium, provided the original work is properly cited.

Nanoheaters are promising tools for localized photothermal therapy (PTT) of malignant cells. The anisotropic AuNPs present tunable surface plasmon resonances (SPR) with ideal NIR optical response to be applied as theranostic agents. To this purpose, nanoparticles with branches are suitable because of the electromagnetic field concentrated at their vertices. We standardized a protocol to synthesize multibranched gold nanoparticles (MB-AuNPs) by the seed-growth method and found a size-seed dependence tunability on the hierarchy of branching. Once the optical response is evaluated, we tested the temporal stability as nanoheaters of the MB-AuNPs immersed in skin-equivalent phantoms by dynamic infrared thermography (DIRT). The most suited sample presents a concentration of  $5.2 \times 10^8$  MB-AuNPs/mL showing good thermal stability with  $\Delta T = 4.5^\circ\text{C}$ , during 3 cycles of 10 min at 785 nm laser irradiation with power of 0.15 W. According to these results, the MB-AuNPs are suitable nanoheaters to be tested for PTT in more complex models.

## 1. Introduction

The last twenty years' research reports on nanostructured materials clearly indicate their potential to develop new technologies for different specialized areas. The extensive investigation work in shape controlled synthesis of metal nanoparticles (NPs) has allowed the achievement of structures with complicated geometric forms and the use of nontoxic chemicals for their synthesis. Gold plays a particular and special role in this area of size and shape controlled synthesis, and because of their properties, those NPs are studied for technological applications in fields such as renewable energies, catalysis, medicine, and photonics. Because of the optical and low-reactive properties of gold nanoparticles (AuNPs), they

have been considered for medical applications as theranostic agents, which means that they can be simultaneously used for drug delivery [1], medical imaging [2–5], localized photothermal therapy (PTT) [6], and biological sensing [7, 8].

Nowadays, for some specific theranostic applications AuNPs are designed with anisotropic shapes, characteristic that tunes their surface plasmon resonance (SPR) from the visible to the near (NIR) and middle infrared (Mid-IR) regions of the spectra, also presenting local concentration of electromagnetic fields on the vertices [9]. The most common anisotropic AuNPs studied and used have been the gold nanorods (AuNRs) and stellated or spiky AuNPs, here termed multibranched gold nanoparticles (MB-AuNPs). The fact that NIR absorbance of MB-AuNPs fits the so-called therapeutic

window present in the human tissue (700–1200 nm) [10], a spectral region where maximum penetration of light occurs due to the minimal absorption of blood components, such as hemoglobin and water [11], is important for these applications.

With the goal to apply these gold nanoheaters on the PTT of cancer (localized heating for killing cancer cells) [12], we have to understand their thermal response under controlled conditions. Thermal response has been evaluated by dynamic thermography technique, as infrared imaging tool for real-time recording of the temperature increases ( $\Delta T$ ). Since the evaluation of nanosystems in real tissue samples presents many out-of-control factors, such as the complexity in the formation of protein corona on the nanoparticles and their interaction with the physiological cellular environment [13, 14], and besides the lack of the reproducibility of results due to the difficulty in finding identical specimens, we decided the use of gel phantoms as skin-equivalent model [12, 15–17] which emulates the dielectric properties of the human body surface. Previous reports had evaluated the thermal response of AuNRs [18] in agar phantoms with intralipid® (fat emulsion) as scattered agent [19] and suggested to be effective for tumor irradiation of 10 mm depth from the illuminated tissue surface. We use for the accurate analysis of MB-AuNPs nanoheaters an optimal agar phantom model, with permittivity close to that of the human skin in the 60 GHz band [20]. The skin-equivalent phantom uses polyethylene powder (PEP) to decrease the real and imaginary parts of the permittivity.

In this report we use the organic molecule HEPES, 2-[4-(2-hydroxyethyl)-1-piperazinyl]ethanesulfonic acid, as shape directing agent. HEPES is one of the good buffers used in cell culture [21] and is also used as reducing and shape directing agent [22, 23] in the synthesis of nanoparticles by wet-chemical [24–26] and hydrothermal methods [27]. The shape promoted by HEPES in nanoparticle formation is mostly multibranched, varying from few to several peaks.

Previously reported seeded-growth synthesis protocol, in which the HEPES act as directing agent and hydroxylamine ( $\text{NH}_2\text{OH}\cdot\text{HCl}$ ) [28–30], is used as reducing agent [31] over the seeds surface; the hydroxylamine has the role of avoiding new nucleation events during the peak growth stage. It has been also reported that hydroxylamine influences or promotes the growth of stellated gold nanoparticles [32]. Thus, we start from this method that involves two molecules, both with capping and direct-shaping properties. The function of the HEPES and hydroxylamine during the growing stage of peaks has been determined by our experimental design on concentrations of the reactants. The seed-growth method allows obtaining good monodispersity in the final product shape and size. We also had found a size-seed dependence tunability on the hierarchy of branching.

In this work, we evaluated the optical response of MB-AuNPs by UV-Vis spectroscopy, and their morphology by electronic microscopy (SEM and HRTEM). Particle density was determined by inductively coupled plasma spectrometry (ICP), and the temporal stability as nanoheaters was tested in skin-equivalent phantoms by dynamic infrared thermography (DIRT).

## 2. Materials and Methods

Deionized water was used for all experiments. The reagents used for NPs synthesis were obtained from Sigma-Aldrich:  $\text{HAuCl}_4\cdot 3\text{H}_2\text{O}$ , HEPES,  $\text{NH}_2\text{OH}\cdot\text{HCl}$ , and sodium citrate. For the preparation of skin-equivalent-phantom, polyethylene powder (PEP) was obtained from Baker, Agar from Sigma-Aldrich, and TX-151 from Oil Center, and all reagents were used as received without further treatment or purification. All glassware was cleaned with aqua regia ( $\text{HCl}:\text{HNO}_3$ , 3:1) and rinsed with plenty of deionized water. The samples were characterized with UV-Vis absorption spectroscopy, acquired on a Cary 60 UV-Vis-NIR spectrophotometer at room temperature. ICP elemental quantification was performed on Variant 730-ES spectrometer. The electron micrographs were acquired in a transmission electron microscope JEOL 2100, and scanning electron micrographs in a FEI-Helios Nanolab. The X-ray diffractograms were obtained in a Bruker DX-8 system at  $\text{CuK}\alpha$  source of wavelength 1.54056 Å. The dynamic thermographs were taken at a distance of 0.3 m from the skin-equivalent phantom [15, 33], using a high-resolution infrared camera with thermal sensitivity better than 40 mK and a 480×360 focal plane array of VOx microbolometers (FLIR T600, FLIR Systems Inc., Wilsonville, OR). The phantoms were evaluated with a 785 nm laser diode with a spot size of 3.5 mm and optical power of 0.15 W. Temperature measurements of the skin-like phantom were taken with and without MB-AuNPs. Data was analyzed with FLIR-IR Research software.

*2.1. Synthesis of Multibranched Gold Nanoparticles (MB-AuNPs) Using a Seed-Growth Method.* The 16 and 18 gold nanospheres (AuNSs) used as seeds were prepared by a reverse-modified Turkevich method [34] by citrate reduction of gold salt. Shortly, in a three-neck round-bottom flask with a condenser mounted, a citrate solution was brought to boiling by a heating mantle for 5 mins; then a gold solution of initial concentration of 25 mM was added, and after a light red ruby color appeared the system was left to react for half hour. For the synthesis of 16 nm AuNSs, the total concentration of sodium citrate and gold salt was 1.8 mM and 0.16 mM, respectively; and for 18 nm AuNSs were 0.75 mM and 0.25 mM. After the reaction was completed, the seeds solution was left to cool down at ambient temperature and used without modifications.

For the MB-AuNPs synthesis we used three concentrations of HEPES buffer [25, 50, 75 mM] as solution. Briefly, under slowly stirring within an ice bath ( $\sim 4^\circ\text{C}$ ) to 12.5 mL of HEPES 50  $\mu\text{L}$  of AuNSs (16 or 18 nm) was added, as well as 30, 60, or 120  $\mu\text{L}$  of hydroxylamine [0.1M], and finally the dropwise addition of gold salt solution with rate of 0.375 mL/min to a final concentration of 0.07 or 0.13 mM. For the reaction to be complete it is necessary to leave the sample to rest 8 h in the fridge. The samples were washed three times by centrifugation and a drop of the concentrated colloid was deposited on an aluminum pin for SEM and on a lacey carbon copper grid for HRTEM. For UV-Vis measurements, the samples were analyzed as synthesized. The samples for ICP quantification were centrifuged and the NPs concentrated was dissolved in aqua regia.

**2.2. Fabrication of Skin-Equivalent Phantom.** For the fabrication of the control phantom a previously reported protocol was used, and the reagents concentration was maintained [20]. The procedure is as follows: a Buchner flask with deionized water and agar was heated until  $\sim 80^\circ\text{C}$  under slow magnetic stirring and vacuum. Once the agar was dissolved and the boiling point was reached, the vacuum and heating were turned off, the TX-151 was added and mixed gently with a stirring rod until its complete incorporation, and then the PEP was added to decrease the real and imaginary parts of the permittivity. After complete PEP incorporation the vacuum was turned on for a moment to avoid bubbles in the final phantom. Finally, the mix was placed into a petri box ( $\phi = 55\text{ mm}$ ) and left to solidify at ambient temperature. When phantoms with nanoparticles were prepared, a 1x concentrated of prewashed MB-AuNPs colloid was added and completely incorporated before TX-151 addition. For comparison, other phantoms with AuNSs were prepared, at the same NPs concentration of MB-AuNPs.

### 3. Results

**3.1. Multibranching Gold Nanoparticles (MB-AuNPs).** In order to prepare monodisperse MB-AuNPs, presynthesized gold single-crystalline and multitwinned nanoparticles are used as seeds for the growth of peaks [28, 29], which grow along preferential crystallographic directions of the metallic core [35]. According to previous reports, the capping agents [36] have preferential adsorption by specific crystalline faces of the metal seeds [37]; and this promotes an accelerated growth rate along specific crystallographic directions [7, 32, 38–40].

The AuNSs, obtained by the reverse Turkevich method, were monodispersed in size (see Figures 1 and SI-1); by ICP spectroscopy was determined the concentration of  $2.39 \times 10^{11}$  and  $3.66 \times 10^{11}$  NPs/mL for 16 and 18 nm AuNSs, respectively. We will see later that the structural characteristics of the AuNSs will influence the growth process of peaks; as can be seen in Figure 1(a), the 16-AuNSs present more symmetrical shape and monocrystalline structure, being different from 18-AuNSs samples (Figure 1(a)) that show multitwinned structure and nonspherical multifaceted shapes. During the stage of peaks formation, the promotion of second-order branching (Figure 3) is up to the seed structure [41] and the stabilizer agent protection [7] at the nanoparticle surface, observed in the MB-AuNPs synthesized from 18 nm nanospheres (18 MB-AuNPs), with 0.13 mM of gold salt. Also, we observed that the growth mechanism of the MB-AuNPs is influenced by the chemical characteristics of the reagents present in the growth solution and by its molar ratio with respect to gold ions.

Therefore, both hydroxylamine and HEPES are dual agents, with reducing and shape capabilities. Manipulation of the role played by each reactive is made through experimental conditions such as temperature (e.g., to slow the HEPES reducing action) and concentration of hydroxylamine (using the necessary to reduce the gold ions). Within the molar rates used in this work, the hydroxylamine governs the reaction kinetics and the final shape of the peaks and the HEPES modulate the peaks growth. A simple way to know if the HEPES has been or not contributing as reducing agent is by

means of UV-Vis spectroscopy (see Figure SI-2), since the nitrogen species from degraded HEPES can be detected by its absorption at  $\sim 346\text{ nm}$  [22]. It is important to mention that, in the reaction where no hydroxylamine is used, the color changes of the colloid take place slowly, evidencing that HEPES is a slow reductor. Increasing the concentration of HEPES (from 25 to 50 mM), the growth of narrow peaks is promoted while the cores remain small. Then the addition of hydroxylamine is necessary to modulate the kinetics without excess of HEPES and will help to obtain better definition on the peaks and a monodisperse size and shape sample (see Figure SI-3). From the mechanism reduction of  $\text{Au}^{3+}$  by hydroxylamine proposed by Minati et al. [42], the molar ratio of  $\text{Au}^{3+}:\text{NH}_2\text{OH}$  (1:3) was used to synthesize the sample with 16 nm nanospheres (16 MB-AuNPs), in order to avoid the intervention of HEPES reducing action (see Figure SI-2). We observed that, when hydroxylamine is present and increases its molar rate, the change of colors gets faster indicating the necessary use of a mild reducing agent (hydroxylamine) simultaneously with a directing shape agent (HEPES) for better anisotropic growth. We also have determined that an excess of hydroxylamine promotes the second-order branching in 18 MB-AuNPs, which was synthesized with molar rate of  $\text{Au}^{3+}:\text{NH}_2\text{OH}$  of 1:6 (see Figure SI-4).

It had been reported that the size of the NPs used as seeds influences the shape of final products [30, 43]. In our results we observed that from 16-AuNSs, MB-AuNPs of 80 nm of diameter can be obtained, synthesized with 0.07 mM of gold salt (16 MB-AuNPs, see Figure SI-5), and the colloid presents a maximum absorbance at 728 nm (Figure 2). On the other hand, dendritic growth is only perceptible in 18 MB-AuNPs (Figure 3), even if the concentration of gold ions is increased in the samples synthesized from 16-AuNSs (see Figure SI-6). The increase in gold ions leads to bigger cores and smaller length of peaks, due to an addition of gold atoms between peaks for minimization of energy, instead of the growth of longer peaks [44, 45].

At this stage we have shown that both sets of samples (16 and 18 MB-AuNPs) present good optical response for being used as nanoheaters. The next criteria for choosing a sample is the critical size for being used in an in vitro or in vivo environment. Thus, we decided the use of 16 MB-AuNPs for being tested as nanoheaters; however, the optical response of 18 MB-AuNPs in the 830 nm (Figure 3) is suitable for applications in nanostructured system for SERS [46].

**3.2. Thermal Response of MB-AuNPs.** Infrared (IR) imaging is based on the fact that any object at a temperature above absolute zero ( $-273^\circ\text{C}$ ) will emit IR radiation, even if only weakly. The human body has a low thermal emittance, radiating in a wavelength range that starts at around  $3\ \mu\text{m}$  and peaks in the vicinity of  $10\ \mu\text{m}$  and trails off from this point into the extreme IR and, negligibly, beyond it. The emissivity of human skin has a constant value between wavelengths of 2 and  $14\ \mu\text{m}$  of  $0.98 \pm 0.01$  for black skin and  $0.97 \pm 0.02$  for white skin [47]; thus, human skin has a known and almost invariant emissivity in this wavelength region that makes IR imaging an ideal procedure to evaluate surface temperature of

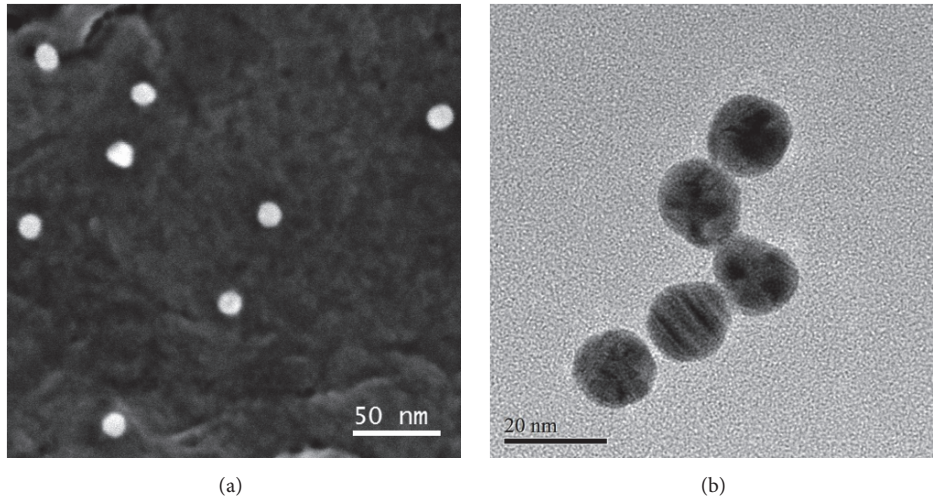


FIGURE 1: (a) SEM micrograph of  $16 \pm 1.69$  nm of spheres gold nanoparticles (16-AuNSs). (b) TEM micrograph of  $18.18 \pm 2.33$  nm sphere gold nanoparticles (18-AuNSs) used as seeds.

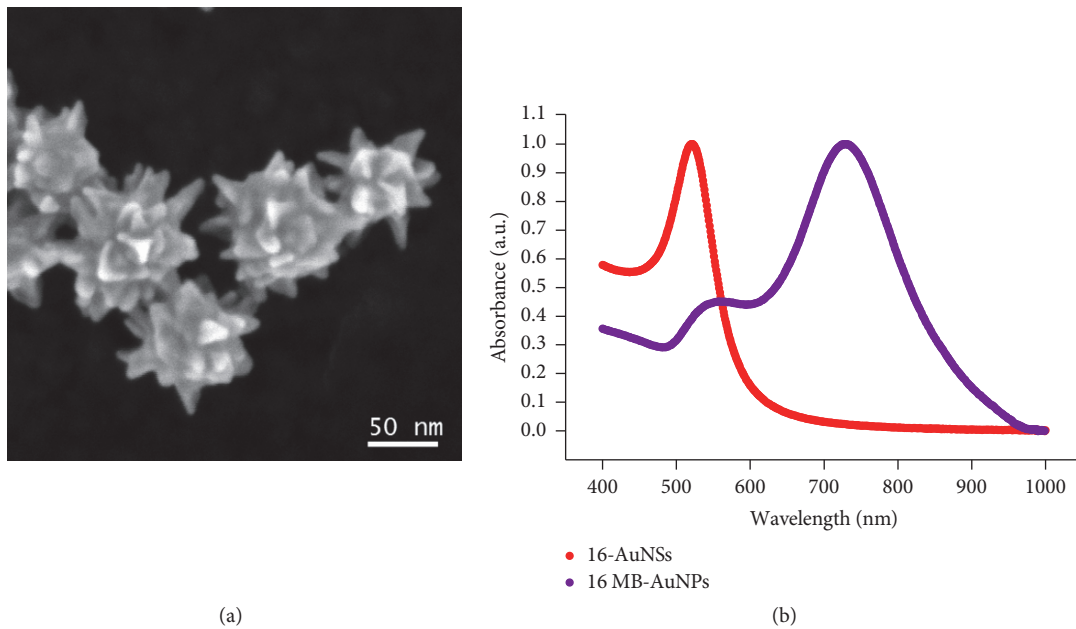


FIGURE 2: (a) SEM micrograph of 16 MB-AuNPs synthesized with 16-AuNSs. (b) UV-Vis spectra of 16-AuNSs and 16 MB-AuNPs with a band centered at 520 nm and 729 nm, respectively.

the human body [48, 49]. Because of the above arguments, the skin-equivalent phantoms with  $0.62 \pm 0.01$  reported emittance [17] is a well suited model for IR thermal evaluation.

The thermal response of 16-AuNSs and 16 MB-AuNPs was evaluated inside the skin-equivalent phantoms by dynamic thermography. The samples were irradiated at 0.15 W power laser by 3 cycles of 10 mins and recorded with an IR camera, and the thermographs shown at Figure 4 were extracted at 555 s using the FLIR-RIR software, which allows the analysis of single points, line profiles, and averages of circle/rectangular areas. The plot in Figure 4(a) shows data from a line profile analyzed at different times, and it clearly can be observed that not only the incident laser area has been heated

but also there is a radial propagation by diffusion of the generated heat; thus there is energy transmitted to the adjacent regions due to the immersed NPs. This effect is also observed in the control phantom analysis, but over a smaller area and with more uniform temperature as can be seen in Figure SI-7. Figure 4(b) reports the information on how fast the system absorbs the energy, achieving constant temperature at early irradiation times (60 s). This was also performed for evidence the continuity of the thermal response of immersed 16 MB-AuNPs in the phantom as a function of time.

The plot in Figure 5 corresponds to a dynamic thermal analysis, and from it we can appreciate the difference in the temperature reached by the three phantoms: the largest

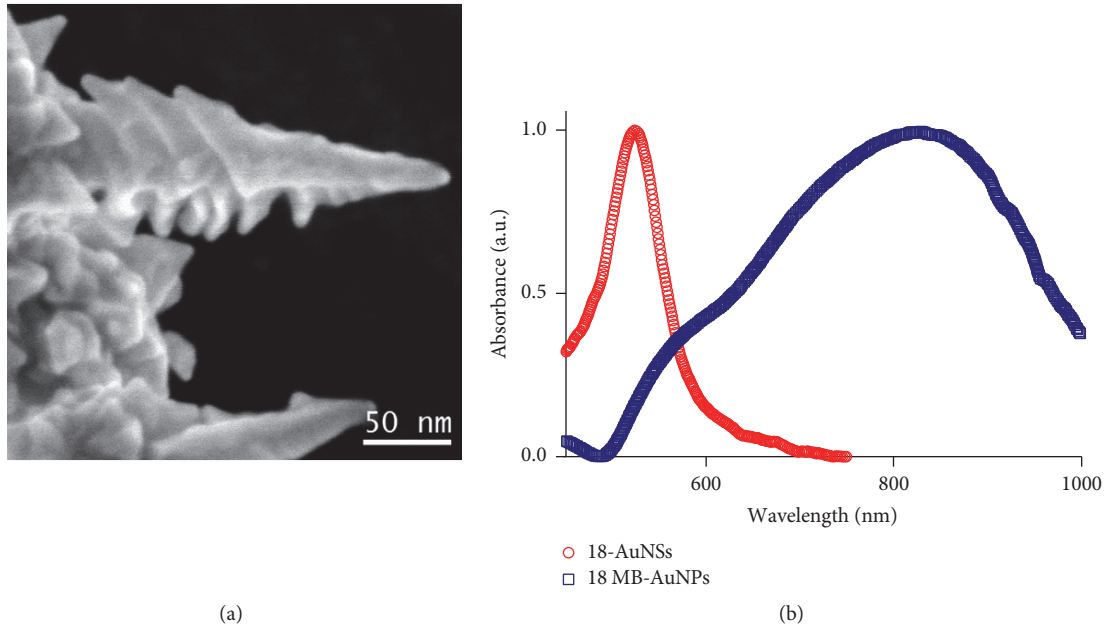


FIGURE 3: SEM micrographs (a) of 18 MB-AuNPs with second order branches and UV-Vis spectra (b) of 18-AuNSs and 18 MB-AuNPs; they have a band centered at 524 nm and 830 nm, respectively.

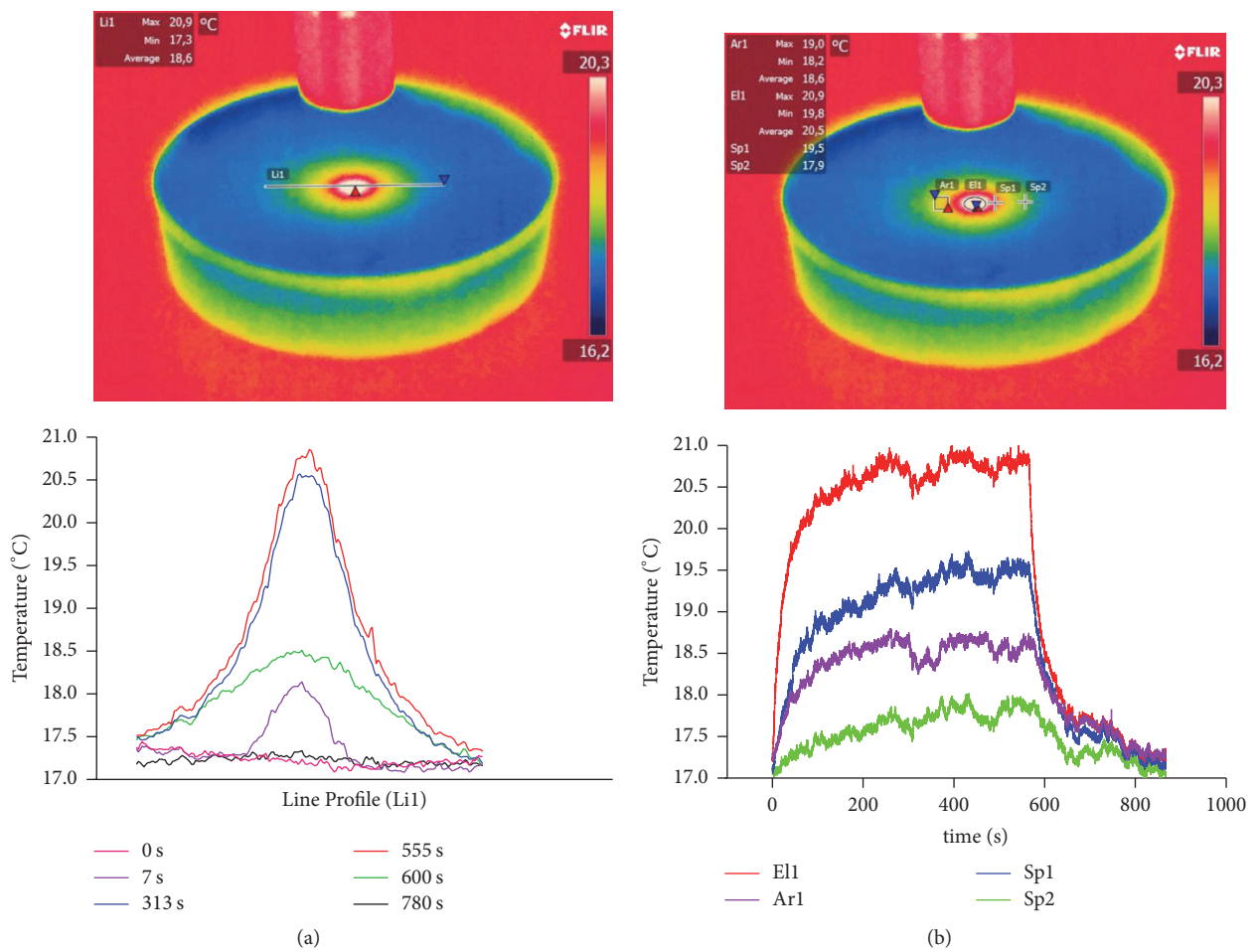


FIGURE 4: The thermography corresponds at the 555 s of laser irradiation. (a) Temperature profiles of the heating area at different times. The profile analyzed is designed as Line 1 (Li1) in the thermography. (b) Temporal analysis of temperature variations of different points and regions marked in the thermography as area (Ar1), elipsoide (E11), and singles points (Sp1, Sp2).

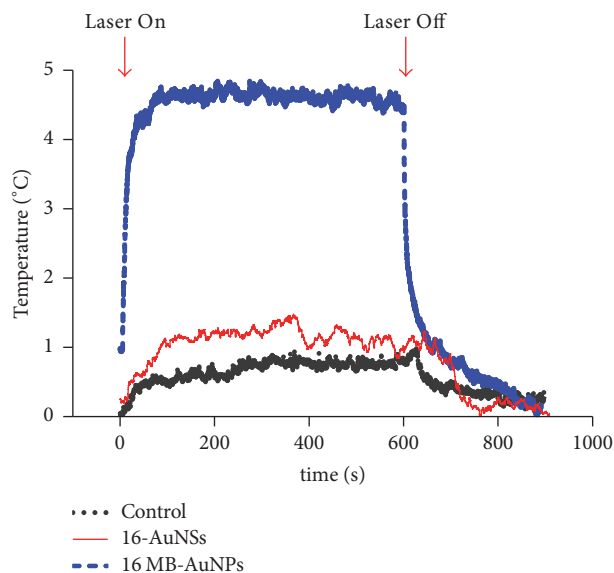


FIGURE 5: Thermal response of skin-equivalent phantoms with 16-AuNSs, 16 MB-AuNPs, and control.

increase of localized temperature is measured in the sample prepared with 16 MB-AuNPs, compared to the phantom with 16-AuNSs and the one without the addition of NPs, used as a control.

A red-shift of the LSPR is present for anisotropic MB-AuNPs compared with spheres (see Figure 1), and a substantial increase in the heating efficiency with respect the sphere is expected. In our results, the maximum temperature increment in 16 MB-AuNPs phantom was achieved in 60 s and maintained during all the laser irradiation. This temperature increment is  $\Delta T = 4.5^\circ\text{C}$  and when the light source is turned off, a fast decay is observed. The comparison between the AuNSs and MB-AuNPs at the same concentration shows the evident increase of thermal response due to the anisotropic shape of MB-AuNPs and the localized SPR's synergy, because the MB-AuNPs absorbs closer to the wavelength of laser irradiation. In the case of the phantom with 16-AuNSs, the increment in temperature can be described for the excitation of hot-spots created in the interaction among spherical NPs [50, 51]. The fact that there were not physical changes observed in the phantoms under laser irradiation, as leaking or deformation, even after the three cycles evaluation is important to mention.

#### 4. Discussion

We have shown that the control on the width, the length, the number of peaks, and the degree of dendritic growth gives rise to an easy tuning of the plasmon resonance spectra [6] and their corresponding higher transduction of light into heat, and therefore gold nanoheaters are good candidates for IR absorption for efficient photothermal therapy of malignant cancer cells.

The structural characteristics of the AuNSs influenced the degree of ramification of the nanoparticle tips, resulting in

second-order branches for MB-AuNPs synthesized from 18-AuNSs, which present crystalline defects promoting directed anisotropy. From 16-AuNSs we could obtain monodisperse samples. After analyzing the impact of HEPES and hydroxylamine on the final tips shape, we estimated that the optimal molar ratio of hydroxylamine: Au ions is 3:1, where this amount is enough to avoid the intervention of HEPES in the reduction. Even if an excess of hydroxylamine may result in a better definition of tips, it can also cause the agglomeration of MB-AuNPs, due to the resulting high ionic force of the solution, that could not be used for clinical applications, and the same argument is valid for higher concentration of HEPES (75 mM). On the other side, the increase on the molar concentration of Au ions (and necessary hydroxylamine) leads to bigger cores and smaller length of tips; thus it shifts the SPR to lower wavelengths making them not practical for PTT.

Regarding the dynamic thermography results for 16 MB-AuNPs, we found that not only the incident laser area is being heated, but also there is a radial propagation of the released heat, which means there is transmission of energy around the adjacent region of the spot due to the immersed NPs. Therefore, the addition of MB-AuNPs results in the production of more efficient centers for scattering and reemission of energy.

The temperature increment achieved by the nanoheaters in this work ( $\Delta T \sim 5^\circ\text{C}$ ) is good enough for effective and minimally harmful gold nanoparticles based photothermal therapy techniques [52]. This temperature increment from multibranch gold nanoparticles immersed in a phantom gel (as a model approach for the real environment in bioapplications) satisfies biomedical requirement for the treatment of superficial diseases (mycoses, fungal infections, and many different types of skin cancer) [53].

#### 5. Conclusions

A synthesis method that uses nonaggressive chemicals for obtaining multibranch gold nanoparticles and secondary growth branching by tuning the seed size is presented. Analysis of the UV-Vis spectra and SEM micrographs allows us to understand the role of each reactant in the final shape of the nanoparticles. The HEPES molecule mainly grow tips from seeds with a random order; and the hydroxylamine can act as a directing shape agent, but this role only follows after its reduction role has been finished in the reaction. A faster depletion of the reactants (by higher concentration of hydroxylamine) during the grow reaction promotes the growth of larger tips with second-order branches.

We have determined that the synthesized multibranch gold nanoparticles increase the temperature in a localized area irradiated with a 785 nm laser. The temperature increment recorded was  $\Delta T = 4.5^\circ\text{C}$ . The 16 MB-AuNPs embedded in the phantom gel is a system that rapidly absorbs the proper incident energy, achieving a plateau of constant temperature within 60 s which is recovered during at least three different cycles. This evaluation indicates MB-AuNPs as an interesting system for being tested as nanoheater in biological models. Furthermore, the evaluation of their photothermal behavior in cultured cells is necessary for their direct application in

medicine. We also propose to carry on the test with an irradiance lower than the ANSI regulation. Due to the experimental conditions reached in our phantoms, we expect that the transduction of light into thermal energy will be more effective, due to the limitation of MB-AuNPs reshaping.

## Conflicts of Interest

The authors declare that they have no conflicts of interest.

## Acknowledgments

The authors acknowledge Ph.D. CONACYT scholarship number 375630 and institutional support from IPICYT. The authors acknowledge Dra. Gladys Judith Labrada-Delgado for SEM and Dr. Hector Gabriel Silva-Pereyra for HRTEM analysis, as well as the infrastructure of the National Laboratory for Nanoscience and Nanotechnology (LINAN) at IPICYT. This work has been supported by CONACYT-Mexico Grants 106437 and 216315. F. J. González would like to acknowledge support from Project 32 of “Centro Mexicano de Innovación en Energía Solar” and by the National Laboratory Program from CONACYT through the Terahertz Science and Technology National Lab (LANCYTT).

## Supplementary Materials

Figure SI-1. Histograms of diameters and frequency distribution data of populations of (a) 200 AuNSs for 16-AuNSs and (b) 100 for 18-AuNSs. Figure SI-2. The increase of the molar concentration of HEPES promotes strong anisotropic formation of the MB-AuNPs. Figure SI-3. Scanning electron microscopy micrograph of 16 MB-AuNPs; the monodispersity and nonagglomeration of the NPs can be observed. Figure SI-4. Diagram of the concentrations of reactants used for the samples analyzed. Figure SI-5. Histograms of diameters and frequency distribution data of populations of 50 16 MB-AuNPs. Figure SI-6. SEM micrographs of MB-AuNPs synthesized in a medium of HEPES [50 mM], with a molar ratio Au<sup>3+</sup>/NH<sub>2</sub>OH of 1 : 3, with (a) 16-AuNSs and (b)-(c) 18-AuNSs. Figure SI-7. Thermography of skin-equivalent phantom used as control. (*Supplementary Materials*)

## References

- [1] T. Lajunen, L. Viitala, L.-S. Kontturi et al., “Light induced cytosolic drug delivery from liposomes with gold nanoparticles,” *Journal of Controlled Release*, vol. 203, pp. 85–98, 2015.
- [2] A. Guerrero-Martínez, S. Barbosa, I. Pastoriza-Santos, and L. M. Liz-Marzán, “Nanostars shine bright for you: colloidal synthesis, properties and applications of branched metallic nanoparticles,” *Current Opinion in Colloid & Interface Science*, vol. 16, no. 2, pp. 118–127, 2011.
- [3] Z. Fan and H. Zhang, “Template synthesis of noble metal nanocrystals with unusual crystal structures and their catalytic applications,” *Accounts of Chemical Research*, vol. 49, no. 12, pp. 2841–2850, 2016.
- [4] W. Park, S. Cho, X. Huang, A. C. Larson, and D. Kim, “Branched Gold Nanoparticle Coating of Clostridium novyi-NT Spores for CT-Guided Intratumoral Injection,” *Small*, vol. 13, no. 5, Article ID 1602722, 2017.
- [5] Y. Ponce De León, J. L. Pichardo-Molina, N. Alcalá Ochoa, and D. Luna-Moreno, “Contrast enhancement of optical coherence tomography images using branched gold nanoparticles,” *Journal of Nanomaterials*, vol. 2012, Article ID 571015, 9 pages, 2012.
- [6] A. Espinosa, A. K. A. Silva, A. Sánchez-Iglesias et al., “Cancer cell internalization of gold nanostars impacts their photothermal efficiency in vitro and in vivo: toward a plasmonic thermal fingerprint in tumoral environment,” *Advanced Healthcare Materials*, vol. 5, no. 9, pp. 1040–1048, 2016.
- [7] J. P. Xie, Q. B. Zhang, J. Y. Lee, and D. I. C. Wang, “The synthesis of SERS-active gold nanoflower tags for in vivo applications,” *ACS Nano*, vol. 2, no. 12, pp. 2473–2480, 2008.
- [8] M. Aioub and M. A. El-Sayed, “A Real-time surface enhanced raman spectroscopy study of plasmonic photothermal cell death using targeted gold nanoparticles,” *Journal of the American Chemical Society*, vol. 138, no. 4, pp. 1258–1264, 2016.
- [9] X.-L. Liu, J.-H. Wang, S. Liang et al., “Tuning plasmon resonance of gold nanostars for enhancements of nonlinear optical response and raman scattering,” *The Journal of Physical Chemistry C*, vol. 118, no. 18, pp. 9659–9664, 2014.
- [10] F. J. González, “Noninvasive detection of filaggrin molecules by raman spectroscopy,” in *Filaggrin*, pp. 93–101, Springer Berlin Heidelberg, Berlin, Germany, 2014.
- [11] H. Berlien and G. J. Müller, *Applied Laser Medicine*, Springer, Berlin, Heidelberg, Germany, 2003.
- [12] R. Ahmad, J. Fu, N. He, and S. Li, “Advanced Gold Nanomaterials for Photothermal Therapy of Cancer,” *Journal of Nanoscience and Nanotechnology*, vol. 16, no. 1, pp. 67–80, 2016.
- [13] P. Foroozandeh and A. A. Aziz, “Merging worlds of nanomaterials and biological environment: factors governing protein corona formation on nanoparticles and its biological consequences,” *Nanoscale Research Letters*, vol. 10, no. 1, p. 221, 2015.
- [14] D. Walczyk, F. B. Bombelli, M. P. Monopoli, I. Lynch, and K. A. Dawson, “What the cell “sees” in bionanoscience,” *Journal of the American Chemical Society*, vol. 132, no. 16, pp. 5761–5768, 2010.
- [15] G. P. Mazzara, R. W. Briggs, Z. Wu, and B. G. Steinbach, “Use of a modified polysaccharide gel in developing a realistic breast phantom for MRI,” *Magnetic Resonance Imaging*, vol. 14, no. 6, pp. 639–648, 1996.
- [16] M. N. Iizuka, M. D. Sherar, and I. A. Vitkin, “Optical phantom materials for near infrared laser photocoagulation studies,” *Lasers in Surgery and Medicine*, vol. 25, no. 2, pp. 159–169, 1999, <http://www.ncbi.nlm.nih.gov/pubmed/10455223>.
- [17] Y. Okano, K. Ito, I. Ida, and M. Takahashi, “The SAR evaluation method by a combination of thermographic experiments and biological,” *IEEE Trans. Microw. Theory Tech*, vol. 48, pp. 2094–2103, 2000.
- [18] N. R. Jana, L. Gearheart, and C. J. Murphy, “Wet chemical synthesis of high aspect ratio cylindrical gold nanorods,” *The Journal of Physical Chemistry B*, vol. 105, no. 19, pp. 4065–4067, 2001.
- [19] C. L. Didychuk, P. Ephrat, A. Chamson-Reig, S. L. Jacques, and J. J. L. Carson, “Depth of photothermal conversion of gold nanorods embedded in a tissue-like phantom,” *Nanotechnology*, vol. 20, no. 19, Article ID 195102, 2009.
- [20] N. Chahat, M. Zhadobov, S. Alekseev, and R. Sauleau, “Human skin-equivalent phantom for on-body antenna measurements in 60GHz band,” *IEEE Electronics Letters*, vol. 48, no. 2, pp. 67–68, 2012.

- [21] N. E. Good and S. Izawa, "Hydrogen Ion Buffers," *Methods in Enzymology*, vol. 24, no. C, pp. 53–68, 1972.
- [22] A. Habib, M. Tabata, and Y. G. Wu, "Formation of Gold Nanoparticles by Good's Buffers," *Bulletin of the Chemical Society of Japan*, vol. 78, no. 2, pp. 262–269, 2005.
- [23] J. Xie, J. Y. Lee, and D. I. C. Wang, "Seedless, surfactantless, high-yield synthesis of branched gold nanocrystals in HEPES buffer solution," *Chemistry of Materials*, vol. 19, no. 11, pp. 2823–2830, 2007.
- [24] R. Chen, J. Wu, H. Li, G. Cheng, Z. Lu, and C.-M. Che, "Fabrication of gold nanoparticles with different morphologies in HEPES buffer," *Rare Metals*, vol. 29, no. 2, pp. 180–186, 2010.
- [25] Y. Bao, H.-C. Yeh, C. Zhong et al., "Formation and stabilization of fluorescent gold nanoclusters using small molecules," *The Journal of Physical Chemistry C*, vol. 114, no. 38, pp. 15879–15882, 2010.
- [26] S. Chen, Q. Lei, W.-X. Qiu et al., "Mitochondria-targeting "Nanoheater" for enhanced photothermal/chemo-therapy," *Biomaterials*, vol. 117, pp. 92–104, 2017.
- [27] H. Li, Z. Lu, J. Wu, H. Yu, X. Yu, and R. Chen, "Hydrothermal synthesis of transition metal oxide nanomaterials in HEPES buffer solution," *Materials Letters*, vol. 64, no. 18, pp. 1939–1942, 2010.
- [28] G. Maiorano, L. Rizzello, M. A. Malvindi et al., "Monodispersed and size-controlled multibranching gold nanoparticles with nanoscale tuning of surface morphology," *Nanoscale*, vol. 3, no. 5, pp. 2227–2232, 2011.
- [29] G. Plascencia-Villa, D. Bahena, A. R. Rodríguez, A. Ponce, and M. José-Yacamán, "Advanced microscopy of star-shaped gold nanoparticles and their adsorption-uptake by macrophages," *Metallomics*, vol. 5, no. 3, pp. 29–32, 2013.
- [30] F. Tian, J. Conde, C. Bao, Y. Chen, J. Curtin, and D. Cui, "Gold nanostars for efficient in vitro and in vivo real-time SERS detection and drug delivery via plasmonic-tunable Raman/FTIR imaging," *Biomaterials*, vol. 106, pp. 87–97, 2016.
- [31] K. R. Brown and M. J. Natan, "Hydroxylamine seeding of colloidal Au nanoparticles in solution and on surfaces," *Langmuir*, vol. 14, no. 4, pp. 726–728, 1998.
- [32] L. Jiang, Y. Tang, C. Liow et al., "Synthesis of fivefold stellate polyhedral gold nanoparticles with 110-facets via a seed-mediated growth method," *Small*, vol. 9, no. 5, pp. 705–710, 2013.
- [33] K. Ito, K. Furuya, Y. Okano, and L. Hamada, "Development and Characteristics of a Biological Tissue-Equivalent Phantom for Microwaves," *Electron. Commun. Japan Part I Commun.*, vol. 84, pp. 67–77, 2001.
- [34] S. K. Sivaraman, S. Kumar, and V. Santhanam, "Monodisperse sub-10nm gold nanoparticles by reversing the order of addition in Turkevich method - The role of chloroauric acid," *Journal of Colloid and Interface Science*, vol. 361, no. 2, pp. 543–547, 2011.
- [35] M. Zhu, B. Lei, F. Ren et al., "Branched Au Nanostructures enriched with a uniform facet: facile synthesis and catalytic performances," *Scientific Reports*, vol. 4, no. 1, article 05259, 2015.
- [36] W. Ahmed, E. Stefan Kooij, A. Van Silfhout, and B. Poelsema, "Controlling the morphology of multi-branched gold nanoparticles," *Nanotechnology*, vol. 21, no. 12, Article ID 125605, 2010.
- [37] P. Senthil Kumar, I. Pastoriza-Santos, B. Rodríguez-González, F. Javier García De Abajo, and L. M. Liz-Marzán, "High-yield synthesis and optical response of gold nanostars," *Nanotechnology*, vol. 19, no. 1, Article ID 015606, 2008.
- [38] L. Zhao, X. Ji, X. Sun, J. Li, W. Yang, and X. Peng, "Formation and stability of gold nanoflowers by the seeding approach: the effect of intraparticle ripening," *The Journal of Physical Chemistry C*, vol. 113, no. 38, pp. 16645–16651, 2009.
- [39] D. H. M. Dam, J. H. Lee, P. N. Sisco et al., "Direct observation of nanoparticle-cancer cell nucleus interactions," *ACS Nano*, vol. 6, no. 4, pp. 3318–3326, 2012.
- [40] H. Yuan, M. Wanhong, C. Chen et al., "Shape and SPR evolution of thorny gold nanoparticles promoted by silver ions," *Chemistry of Materials*, vol. 19, no. 7, pp. 1592–1600, 2007.
- [41] O. Bibikova, A. Popov, A. Bykov et al., "Plasmon-resonant gold nanostars with variable size as contrast agents for imaging applications," *IEEE Journal of Selected Topics in Quantum Electronics*, vol. 22, no. 3, Article ID 2526602, pp. 13–20, 2016.
- [42] L. Minati, F. Benetti, A. Chiappini, and G. Speranza, "One-step synthesis of star-shaped gold nanoparticles," *Colloids and Surfaces A: Physicochemical and Engineering Aspects*, vol. 441, pp. 623–628, 2014.
- [43] A. Gole and C. J. Murphy, "Seed-mediated synthesis of gold nanorods: role of the size and nature of the seed," *Chemistry of Materials*, vol. 16, no. 19, pp. 3633–3640, 2004.
- [44] R. G. Weiner and S. E. Skrabalak, "Metal dendrimers: Synthesis of hierarchically stellated nanocrystals by sequential seed-Directed overgrowth," *Angewandte Chemie International Edition*, vol. 54, no. 4, pp. 1181–1184, 2015.
- [45] M. S. Bakshi, "How surfactants control crystal growth of nanomaterials," *Crystal Growth and Design*, vol. 16, no. 2, pp. 1104–1133, 2016.
- [46] A. Zoppi, S. Trigari, G. Margheri, M. Muniz-Miranda, and E. Giorgetti, "Gold nanostars as SERS-active substrates for FT-Raman spectroscopy," *RSC Advances*, vol. 5, no. 11, pp. 8523–8532, 2015.
- [47] B. F. Jones, "A reappraisal of the use of infrared thermal image analysis in medicine," *IEEE Transactions on Medical Imaging*, vol. 17, no. 6, pp. 1019–1027, 1998.
- [48] J. Teich, "Digital infrared imaging for medicine. Recent advances in I.R. focal plane array imaging technology," in *Proceedings of the 18th Annual International Conference of the IEEE Engineering in Medicine and Biology Society*, pp. 2079–2080, Amsterdam, Netherlands.
- [49] J. P. Gore and L. X. Xu, "Thermal imaging for biomedical and medical diagnostics," in *Biomedical Photonics Handbook*, T. Vo-Dinh, Ed., CRC Press, Boca Raton, FL, USA, 2003.
- [50] C. Farcau and S. Astilean, "Mapping the SERS efficiency and hot-spots localization on gold film over nanospheres substrates," *The Journal of Physical Chemistry C*, vol. 114, no. 27, pp. 11717–11722, 2010.
- [51] A. J. Pasquale, B. M. Reinhard, and L. Dal Negro, "Engineering photonic-plasmonic coupling in metal nanoparticle necklaces," *ACS Nano*, vol. 5, no. 8, pp. 6578–6585, 2011.
- [52] X. Zhu, W. Feng, J. Chang et al., "Temperature-feedback upconversion nanocomposite for accurate photothermal therapy at facile temperature," *Nature Communications*, vol. 7, Article ID 10437, 2016.
- [53] G. Chirico, P. Pallavicini, and M. Collini, "Gold nanostars for superficial diseases: A promising tool for localized hyperthermia?" *Nanomedicine*, vol. 9, no. 1, pp. 1–3, 2014.

## Research Article

# Antimicrobial Nanocomposites Prepared from Montmorillonite/Ag<sup>+</sup>/Quaternary Ammonium Nitrate

Lin Zhang,<sup>1,2,3</sup> Jienan Chen ,<sup>1,2,3,4</sup> Wenji Yu,<sup>5</sup> Qingfeng Zhao,<sup>1,2,3</sup> and Jin Liu<sup>1,2,3</sup>

<sup>1</sup>Ministry of Forestry Bioethanol Research Center, Changsha 410004, China

<sup>2</sup>Hunan Engineering Research Center for Woody Biomass Conversion, Changsha 410004, China

<sup>3</sup>Bioenvironmental Research Institute, Central South University of Forestry and Technology, Changsha 410004, China

<sup>4</sup>Transpoints Inc., P.O. Box 141742, Gainesville, FL 32614, USA

<sup>5</sup>Research Institute of Wood Industry, Chinese Academy of Forestry, Beijing 100091, China

Correspondence should be addressed to Jienan Chen; [chenjnx@163.com](mailto:chenjnx@163.com)

Received 22 September 2017; Accepted 5 December 2017; Published 1 January 2018

Academic Editor: Leszek A. Dobrzański

Copyright © 2018 Lin Zhang et al. This is an open access article distributed under the Creative Commons Attribution License, which permits unrestricted use, distribution, and reproduction in any medium, provided the original work is properly cited.

Nanocomposites of Ag with organic montmorillonite (Ag-OMMT), Ag with montmorillonite (Ag-MMT), and organic montmorillonite (OMMT) were successfully prepared via a one-step solution-intercalated method. Sodium MMT, silver nitrate, and dimethyl octadecyl hydroxy ethyl ammonium nitrate were used as precursors. X-ray diffraction, Fourier transform infrared spectroscopy, transmission electron microscopy, and energy dispersive spectroscopy analyses confirmed that the MMT layers were intercalated, and Ag<sup>+</sup> was partly reduced to silver nanoparticles with diameters within 10–20 nm in Ag-OMMT. The decomposition temperature of the organic cations in OMMT and Ag-OMMT increased to 220°C, as revealed by differential scanning calorimetry-thermogravimetric analysis. The antimicrobial activity of the nanocomposites was tested by measuring the minimum inhibitory concentration (MIC) and killing rate. The MICs of Ag-OMMT against *Staphylococcus aureus*, *Escherichia coli*, and *Candida albicans* were 0.313, 2.5, and 0.625 mg/mL, respectively. Because of the presence of quaternary ammonium nitrate, Ag-OMMT has a better MIC against Gram-positive bacteria compared to Gram-negative bacteria and fungi. OMMT did not show antimicrobial activity against *Escherichia coli* and *Candida albicans*. In 2 h, 0.0125 mg/mL Ag-OMMT could kill 100% of *S. aureus*, *E. coli*, and *C. albicans* in solution, and Ag-MMT could kill 99.995% of *S. aureus*, 90.15% of *E. coli*, and 93.68% of *C. albicans*. These antimicrobial functional nanocomposites have the potential for application in the area of surface decoration films.

## 1. Introduction

Montmorillonite (MMT), an all-purpose clay, is widely used in a range of applications because of its high cation exchange capacity, swelling capacity, high surface areas, and strong adsorption and absorption capacities [1–3]. In recent years, the synthesis and application of MMT-based antibacterial materials have attracted great interest due to global concerns regarding public health. Some researchers have reported modified MMT materials with antibacterial activity. For example, silver, copper, and zinc ions have been immobilized on MMT [4–9], and cetylpyridinium, cetyltrimethylammonium [10–12], tetradecyltrimethylammonium [13], chitosan [14, 15], and chlorhexidine acetate [16] have been intercalated into the MMT layers. In addition, pharmacology studies

have revealed that MMT can adsorb to bacteria such as *Escherichia coli* (*E. coli*), *Staphylococcus aureus* (*S. aureus*), and immobilized cell toxins [17, 18].

Meanwhile, polymers used in several industries such as food processing, biomedical devices, and filtering are required to have antiseptic ability to minimize the transmission of bacterial infections [19]. The dispersibility and compatibility of antimicrobials with polymers is one of the key factors for the preparation of antimicrobial polymers. To improve the compatibility between the antimicrobial and polymer, surface modification of the antimicrobial is required. Furthermore, a lot of researches [20–23] shown that nanoparticles, such as clay and graphene nanoplatelets which was incorporated in antimicrobial polymer nanocomposites, allowed for the tuning of the release of antimicrobial agents,

TABLE 1:  $d_{001}$  of MMT modified with different organic cations.

Sample	MMT	Ag-MMT	OMMT	2.25 mmol Ag-OMMT	4.5 mmol Ag-OMMT	6.75 mmol Ag-OMMT	9.0 mmol Ag-OMMT	11.25 mmol Ag-OMMT
$2\theta_{001}/^\circ$	7.019	6.396	4.460	4.498	4.480	4.360	4.419	4.418
$d_{001}/\text{nm}$	1.258	1.381	1.980	1.963	1.971	2.025	1.998	1.998

especially reducing the burst release effect, without hindering the antimicrobial activity of the obtained materials.

The aim of this work was to prepare organic antiseptic MMT with good compatibility and dispersibility for use as a nanoadditive in polymers. For this purpose, MMT was modified with  $\text{Ag}^+$  and quaternary ammonium nitrate via a one-step solution-intercalation technique. The structures of different antimicrobial organic MMTs were characterized by X-ray diffraction (XRD), Fourier transform infrared spectroscopy (FTIR), scanning electron microscopy (SEM), transmission electron microscopy (TEM), and energy dispersive spectroscopy (EDS) techniques, and the thermal stability was confirmed by differential scanning calorimetry-thermogravimetric (DSC-TG) analysis. The antimicrobial activity of the nanocomposites was evaluated by examining the minimum inhibitory concentration (MIC) and killing rate.

## 2. Experimental

**2.1. Materials.** Sodium MMT used in this study was supplied by Zhejiang Fenghong Clay Chemicals Co., Ltd (China). The cation exchange capacity (CEC) of MMT was 90 meq  $(100\text{ g})^{-1}$ . Silver nitrate ( $\text{AgNO}_3$ ) with a purity of 99.8% was provided by Hunan Hipure Chemical Reagent Factory (China). Dimethyl octadecyl hydroxy ethyl ammonium nitrate (DOHEAN) at 50% (w/w) in butanol was provided by Jiangsu Hai'an Petrochemical Plant (China). Other reagents used in this study were of analytical grade.

**2.2. Synthesis of Antimicrobial Organoclays.** 10 g sodium MMT was dispersed in 200 mL deionized water and stirred at  $80^\circ\text{C}$ .  $\text{AgNO}_3$  (equimolar with the CEC) was dissolved in deionized water and then slowly dropped into the MMT sol, which was then kept at  $80^\circ\text{C}$  for 1 h with stirring. An equimolar quantity of DOHEAN was added to the  $\text{Ag}^+$  and MMT sol and kept at  $80^\circ\text{C}$  for 2 h with stirring. The intercalated montmorillonite (Ag-OMMT) was repeatedly washed with deionized water to remove residual  $\text{AgNO}_3$  and DOHEAN. This composite was then dried at  $100^\circ\text{C}$  for 24 h and then ground to a size less than 300 mesh.

The preparation of Ag-MMT and OMMT were consistent with the above methods but absented the process of addition  $\text{AgNO}_3$  and DOHEAN, respectively.

**2.3. Measurements.** XRD measurements were performed using a D/Max 2550 diffractometer (Rigaku Electrical Co., Ltd.) with a Cu target and  $K_\alpha$  radiation ( $\lambda = 0.154\text{ nm}$ ). TG and DSC curves were recorded at  $20\text{--}800^\circ\text{C}$  with a heating rate of  $10^\circ\text{C}/\text{min}$  under  $\text{N}_2$  (Netzsch STA 449 C). FTIR spectra were collected from KBr pressed disks on a

Nicolet 380 spectrophotometer. SEM images were recorded with a JEOL JSM-6380LV microscope, and TEM and EDS characterizations were performed on a Tecnai G2 20 FEI AEM.

**2.4. Evaluation of Antimicrobial Activity.** Gram-positive bacteria *Staphylococcus aureus*, Gram-negative bacteria *Escherichia coli*, and fungi *Candida albicans* were provided by the China Center of Industrial Culture Collection (CICC at Beijing).

**2.4.1. Minimum Inhibitory Concentration [24].** MIC tests were performed in MHA for the bacteria and fungi. A serial twofold dilution of Ag-OMMT was added to an equal volume of medium to obtain a concentration of  $5000\ \mu\text{g}/\text{mL}$ , which was serially diluted by double technique to achieve solutions of  $2500\text{--}9.77\ \mu\text{g}/\text{mL}$ . Control dishes containing equal volumes of distilled water were also prepared. After cooling and drying, the plates were inoculated with  $2\ \mu\text{L}$  of  $10^7$  CFU/mL strain solutions and incubated aerobically at  $27^\circ\text{C}$  for 16–20 h for bacteria or 72–96 h for fungi. Growth control samples of each tested strain were also included. The MIC was defined as the lowest concentration required to inhibit bacterial growth, that is, the concentration at which  $<5$  microorganism colonies were visible.

**2.4.2. Antimicrobial Killing Rate [24].** The microorganism suspension was diluted using 0.9% (w/v) sterile saline water to  $10^4$  CFU/mL. 1 mL of cell suspension was added to 95 mL of 0.05, 0.025, and 0.0125 mg/mL nanocomposite (Ag-MMT and Ag-OMMT) solutions that had been autoclaved at  $121^\circ\text{C}$  for 20 min. Nanoscale  $\text{SiO}_2$  was used as a control. The samples were removed after 2 h shake cultivation.  $50\ \mu\text{L}$  aliquots were spread on nutrient agar plates, which were incubated at  $37^\circ\text{C}$  for 24 h, and the numbers of colonies were counted for each solution. The percent reductions in plate colony counts were calculated by comparing the experiment plates to the control. All presented data were averaged from at least 3 parallel experiments, where the discrepancies among them were  $<5\%$ .

## 3. Results and Discussion

**3.1. Structure and Morphology.** The XRD patterns of unmodified MMT, Ag-MMT, OMMT, and Ag-OMMTs (modified with different amounts of  $\text{Ag}^+$ ) are presented in Figure 1. Table 1 shows the  $d$ -spacing of 001 ( $d_{001}$ ) for MMT as calculated by Bragg's equation [25]. Ag-MMT features a larger basal spacing (1.381 nm) than MMT (1.258 nm), indicating that  $\text{Ag}^+$  was exchanged in the silicate layers. Both OMMT and Ag-OMMT feature wide basal spacings with

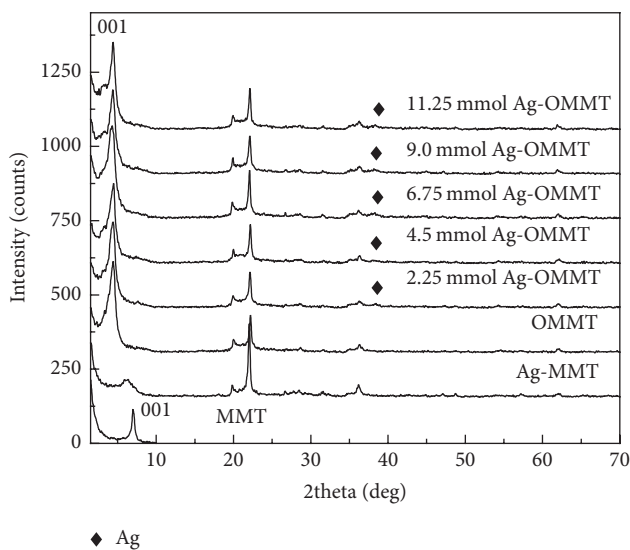


FIGURE 1: XRD patterns of MMT, Ag-MMT, OMMT, and Ag-OMMTs with different amounts of  $\text{Ag}^+$ . MMT: unmodified MMT; Ag-MMT: MMT modified with Ag; OMMT: MMT modified with DOHEAN; Ag-OMMT: MMT modified with Ag and DOHEAN.

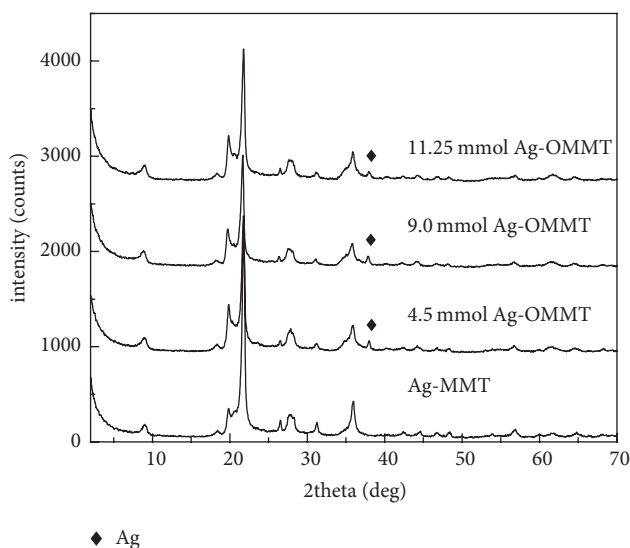


FIGURE 2: XRD patterns of Ag-MMT and Ag-OMMTs (different amounts of  $\text{Ag}^+$ ) after calcination at  $750^\circ\text{C}$  for 2 h. MMT: unmodified MMT; Ag-MMT: MMT modified with Ag; OMMT: MMT modified with DOHEAN; Ag-OMMT: MMT modified with Ag and DOHEAN.

high  $d_{001}$  values between 1.96 nm and 2.03 nm, indicating that DOHEAN has been intercalated into the MMT layers.

As shown in Figure 1, minimal metallic silver is present in all the Ag-OMMTs (at  $2\theta = 38^\circ$ ) but is absent in Ag-MMT. This is also noted in Figure 2, which shows the XRD patterns of Ag-MMT and Ag-OMMTs having different amounts of  $\text{Ag}^+$  after calcination at  $750^\circ\text{C}$  for 2 h. In the presence of easily oxidizable organic cations,  $\text{Ag}^+$  as an oxidant was partly reduced to metallic silver during the preparation process; after high temperature calcination, the reaction of

$\text{Ag}^+$  and DOHEAN was complete. However, in the absence of organic cation,  $\text{Ag}^+$  could not easily be deoxidized, even after calcination at  $750^\circ\text{C}$ . This has also been demonstrated by EDS (Figure 3).

Figure 3 shows the EDS pattern of Ag-OMMT and the morphologies of Ag-MMT and Ag-OMMT. The modified MMTs appear as sandwich-like crystals in the TEM images. Numerous black spots are homogeneously dispersed in the MMT crystals, as shown in Figure 3(b), which are metallic silver nanoparticles as demonstrated by EDS and XRD analyses. These silver nanoparticles are smaller in Ag-MMT (particle diameter within 2–5 nm, Figure 3(a)) than in Ag-OMMT (particle diameter within 10–20 nm, Figure 3(a)) because  $\text{Ag}^+$  is more easily deoxidized in the presence of organic cations; this is in agreement with the XRD results (Figures 1 and 2). Figure 4 presents SEM micrographs showing the morphology change of MMT before and after modification. Unmodified MMT (Figure 4(a)) has a compact and flat surface, while, after modification, the MMT surface becomes crinkled and rough with wide interspacing (Figure 4(b)), which is desirable for use as a nanoadditive.

**3.2. DSC-TG.** DSC-TG curves of DOHEAN, MMT, Ag-MMT, OMMT, and Ag-OMMT are shown in Figure 5. The TG curve of each sample shows an endothermic peak below  $100^\circ\text{C}$  with a corresponding weight-loss due to the removal of water. The DSC curves of MMT and Ag-MMT both feature a second endothermic peak at  $679.2^\circ\text{C}$  and  $674^\circ\text{C}$ , respectively, corresponding to the loss of hydrated water of the interlayer cations and the structural hydroxyls [26].

The sharp exothermic peak on the DSC curve of DOHEAN represents the evaporation or decomposition of DOHEAN. However, there are two exothermic peaks on the DSC curves of OMMT and Ag-OMMT. The low-temperature exothermic peak corresponds to the evaporation or decomposition of DOHEAN on the silicate plate surfaces, and the other peak represents the evaporation or decomposition of DOHEAN between the silicate plates. The TG curves of OMMT and Ag-OMMT reveal that the evaporation or decomposition of DOHEAN occurs at approximately  $220^\circ\text{C}$ , which is higher than that of pure DOHEAN ( $160^\circ\text{C}$ ). This indicates that the organic cation has intercalated into the MMT layers, similar to the initial state, and that the silicate platelets have the ability to protect organic molecules from decomposition. [27]. A similar behavior was reported by Scaffaro et al. [28] during the preparation of poly(ethylene-co-vinyl acetate) films with two commercial formulations of nisin.

**3.3. FTIR.** Figure 6 shows the FTIR spectra of MMT, DOHEAN, Ag-MMT, OMMT, and Ag-OMMT. Compared to MMT, OMMT has additional absorption peaks appearing at  $2921$ ,  $2850$ , and  $1384\text{ cm}^{-1}$ . The peaks at  $2921$  and  $2850\text{ cm}^{-1}$  arise from  $-\text{CH}_2-$  and  $-\text{CH}_3$  stretching vibrations, while the one at  $1384\text{ cm}^{-1}$  belongs to C–H symmetric deformation vibrations [29]. This further reveals that DOHEAN has intercalated into the MMT layers. The peak at  $3100$ – $3700\text{ cm}^{-1}$  represents O–H stretching vibrations [30] and the peak at  $1638\text{ cm}^{-1}$  belongs to H–O–H bending vibrations [31]. This

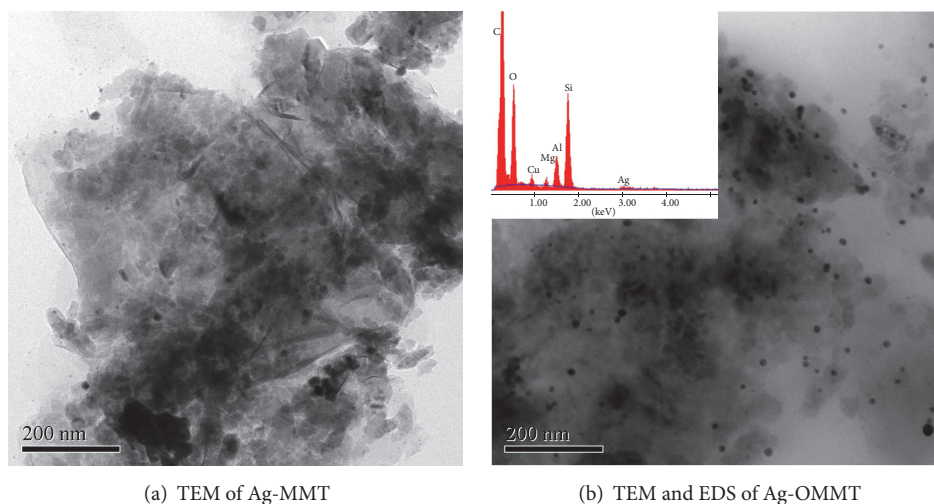


FIGURE 3: EDS pattern of Ag-OMMT and TEM micrographs of Ag-MMT and Ag-OMMT.

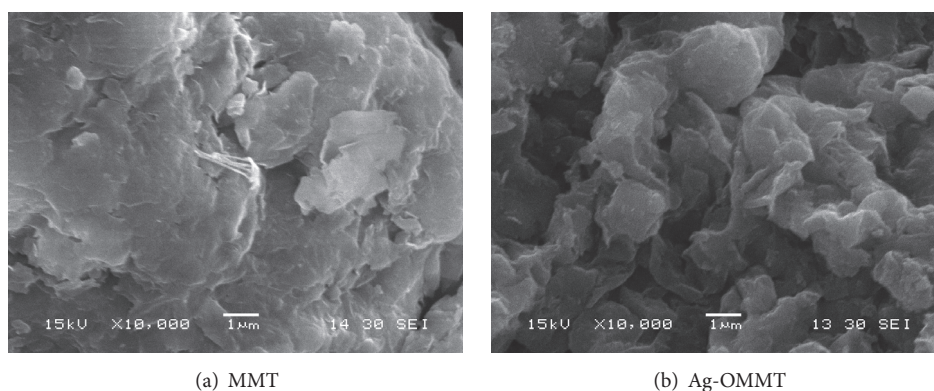


FIGURE 4: SEM micrographs of MMT and Ag-OMMT.

TABLE 2: MIC of the samples.

Samples	MIC (mg/mL)		
	<i>S. aureus</i>	<i>E. coli</i>	<i>C. albicans</i>
Ag-MMT	1.25	2.5	0.625
OMMT	2.5	>40	>40
Ag-OMMT	0.313	2.5	0.625

band, which is related to the  $\nu_2(\text{H-O-H})$  bending vibration of water adsorbed on MMT, shifted from  $1631\text{ cm}^{-1}$  in MMT to  $1638\text{ cm}^{-1}$  for Ag-OMMT. Meanwhile, the intensity of this band decreased, reflecting that the amount of water adsorbed on MMT decreased after modification of the MMT with organic cations.

**3.4. Antimicrobial Activity Assay.** As shown in Table 2, Ag-MMT and Ag-OMMT have obvious antimicrobial activity against a wide variety of microorganisms, including Gram-positive bacteria, Gram-negative bacteria, and fungi. They have the same MIC for *E. coli* and *C. albicans*, which are 2.5 and 0.625 mg/mL, respectively. In addition, Ag-OMMT

has a higher MIC (0.313 mg/mL) for *S. aureus* than Ag-MMT (1.25 mg/mL). Strong antimicrobial activity was also observed, as outlined in Table 3. At a concentration of 0.0125 mg/mL, Ag-OMMT can kill 100% of the *S. aureus*, *E. coli*, and *C. albicans* population in 2 h, and Ag-MMT can kill 99.995% of the *S. aureus*, 90.15% of *E. coli*, and 93.68% of *C. albicans* in 2 h.

OMMT can inhibit the growth of *S. aureus*; however, its ability to inhibit the growth of *E. coli* and *C. albicans* is less pronounced. This phenomenon is due to the different cell structures of these microbes. *S. aureus*, a Gram-positive bacterium, consists of a thick peptidoglycan layer and a cytoplasmic membrane. Its peptidoglycan layer is extensively crosslinked in three dimensions to form a solid mesh. Despite its thickness, the peptidoglycan layer of Gram-positive bacteria is not a barrier to the diffusion of foreign molecules. Gram-negative bacteria, however, have a small layer of peptidoglycan and an outer membrane made of a toxic liposaccharide layer. Because of this structure, Gram-negative bacteria are unusually permeable to foreign molecules. Therefore, Gram-negative bacteria are generally less susceptible to antibiotics and antibacterial agents than Gram-positive bacteria [32].

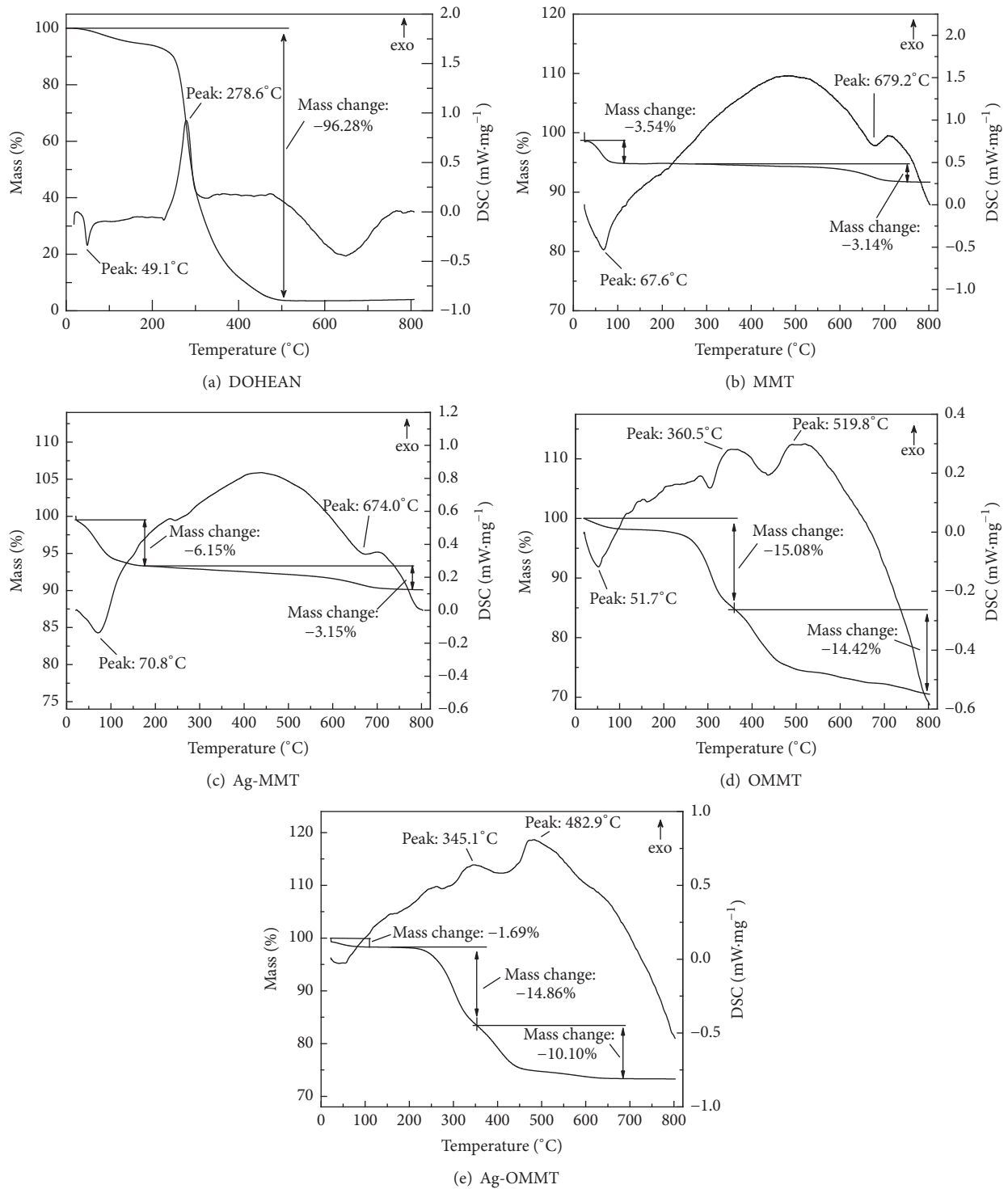


FIGURE 5: DSC-TG profiles of DOHEAN, MMT, Ag-MMT, OMMT, and Ag-OMMT.

TABLE 3: Killing rate of the samples.

$C_{\text{sample}}/(\text{mg}\cdot\text{ml}^{-1})$	Killing rate/%					
	<i>S. aureus</i>		<i>E. coli</i>		<i>C. albicans</i>	
	Ag-MMT	Ag-OMMT	Ag-MMT	Ag-OMMT	Ag-MMT	Ag-OMMT
0.05	100	100	100	100	100	100
0.025	100	99.996	100	99.99	100	99.996
0.0125	100	99.995	100	90.15	100	93.68

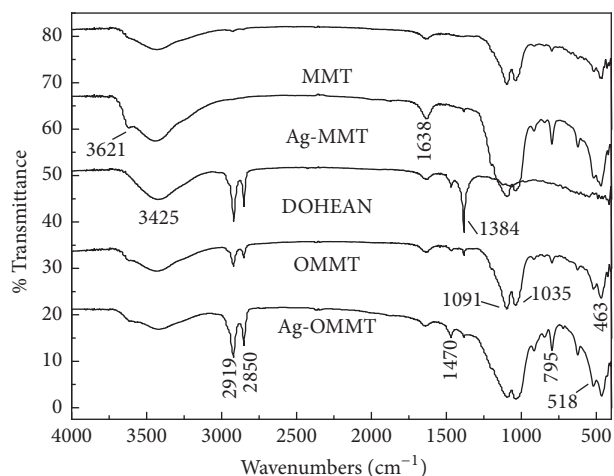


FIGURE 6: FTIR spectra of MMT, DOHEAN, Ag-MMT, OMMT, and Ag-OMMT.

#### 4. Conclusions

Novel antimicrobial nanocomposites featuring sodium MMT,  $\text{Ag}^+$ , and dimethyl octadecyl hydroxy ethyl ammonium nitrate were synthesized via a one-step solution-intercalated method. XRD, DSC-TG, FTIR, SEM, TEM, and EDS characterization indicated that  $\text{Ag}^+$  and DOHEAN were intercalated into the MMT layers. Ag formed both metallic species and  $\text{Ag}^+$  in the clay layer, while DOHEAN was chemically bonded with the MMT layers. The thermal stability of DOHEAN was improved by the protection from the MMT layers. The nanocomposite surface became crinkled and rough after modification, making it suitable for combining with polymers. Further, the nanocomposites showed a wide range of highly efficient antimicrobial activity. The results of this study may be used as a foundation for the future development of new types of nanocomposites of antimicrobial polymers in many industries, such as in wood adhesives, plastics, paints, and rubbers.

#### Conflicts of Interest

The authors declare that they have no conflicts of interest.

#### Acknowledgments

This work was supported by the National Special Program for International Science and Technology Cooperation (no. 2015DFA01120), the Hunan Province Major Program of Science and Technology (2017NK1010), the Key Projects in the National Science & Technology Pillar Program during the Eleventh Five-year Plan Period of China (2006BAD07A07-08), and the Hunan Province Natural Science Foundation (2015JJ5007).

#### References

- [1] R. K. Gogoi and K. Raidongia, "Strategic shuffling of clay layers to imbue them with responsiveness," *Advanced Materials*, vol. 29, no. 24, Article ID 1701164, 2017.
- [2] J. L. Suter, D. Groen, and P. V. Coveney, "Chemically specific multiscale modeling of clay-polymer nanocomposites reveals intercalation dynamics, tactoid self-assembly and emergent materials properties," *Advanced Materials*, vol. 27, no. 6, pp. 966–984, 2015.
- [3] X. Wang, B. Liu, and P. Yu, "Research on the Preparation and Mechanism of the Organic Montmorillonite and Its Application in Drilling Fluid," *Journal of Nanomaterials*, vol. 2015, Article ID 514604, 10 pages, 2015.
- [4] S. Sh, M. Rassa, and D. E. Mohammadi, "Spectroscopic study of silver halides in montmorillonite and their antibacterial activity," *Journal of Photochemistry and Photobiology B: Biology*, vol. 163, pp. 150–155, 2016.
- [5] C. Perrine, G. Fabrice, and E. Eliane, "Preparation, characterization and barrier properties of silver/montmorillonite/starch nanocomposite films," *Journal of Membrane Science*, vol. 497, pp. 162–171, 2016.
- [6] J. F. Martucci and R. A. Ruseckaite, "Antibacterial activity of gelatin/copper (II)-exchanged montmorillonite films," *Food Hydrocolloids*, vol. 64, pp. 70–77, 2017.
- [7] L. F. Jiao, Y. L. Ke, K. Xiao, Z. H. Song, J. J. Lu, and C. H. Hu, "Effects of zinc-exchanged montmorillonite with different zinc loading capacities on growth performance, intestinal microbiota, morphology and permeability in weaned piglets," *Applied Clay Science*, vol. 112–113, pp. 40–43, 2015.
- [8] T. Li, O. Lin, Z. Lu, L. He, and X. Wang, "Preparation and characterization of silver loaded montmorillonite modified with sulfur amino acid," *Applied Surface Science*, vol. 305, pp. 386–395, 2014.
- [9] S. Sohrabnezhad, M. Rassa, and A. Seifi, "Green synthesis of Ag nanoparticles in montmorillonite," *Materials Letters*, vol. 168, pp. 28–30, 2016.
- [10] G. Özdemir, S. Yapar, and M. H. Limoncu, "Preparation of cetylpyridinium montmorillonite for antibacterial applications," *Applied Clay Science*, vol. 72, pp. 201–205, 2013.
- [11] Y. L. Ke, L. F. Jiao, Z. H. Song et al., "Effects of cetylpyridinium-montmorillonite, as alternative to antibiotic, on the growth performance, intestinal microflora and mucosal architecture of weaned pigs," *Animal Feed Science and Technology*, vol. 198, pp. 257–262, 2014.
- [12] P. Herrera, R. Burghardt, H. J. Huebner, and T. D. Phillips, "The efficacy of sand-immobilized organoclays as filtration bed materials for bacteria," *Food Microbiology*, vol. 21, no. 1, pp. 1–10, 2004.
- [13] B. K. G. Theng, J. Aislabie, and R. Fraser, "Bioavailability of phenanthrene intercalated into an alkylammonium-montmorillonite clay," *Soil Biology & Biochemistry*, vol. 33, no. 6, pp. 845–848, 2001.
- [14] S. Bensalem, B. Hamdi, S. Del Confetto et al., "Characterization of chitosan/montmorillonite bionanocomposites by inverse gas chromatography," *Colloids and Surfaces A: Physicochemical and Engineering Aspects*, vol. 516, pp. 336–344, 2017.
- [15] V. Ambrogi, D. Pietrella, M. Nocchetti et al., "Montmorillonite-chitosan-chlorhexidine composite films with antibiofilm activity and improved cytotoxicity for wound dressing," *Journal of Colloid and Interface Science*, vol. 491, pp. 265–272, 2017.
- [16] K. Saha, B. S. Butola, and M. Joshi, "Synthesis and characterization of chlorhexidine acetate drug-montmorillonite intercalates for antibacterial applications," *Applied Clay Science*, vol. 101, pp. 477–483, 2014.

- [17] P. Herrera, R. C. Burghardt, and T. D. Phillips, "Adsorption of *Salmonella enteritidis* by cetylpyridinium-exchanged montmorillonite clays," *Veterinary Microbiology*, vol. 74, no. 3, pp. 259–272, 2000.
- [18] Y. Zhou, M. Xia, Y. Ye, and C. Hu, "Antimicrobial ability of  $\text{Cu}^{2+}$ -montmorillonite," *Applied Clay Science*, vol. 27, no. 3-4, pp. 215–218, 2004.
- [19] H. Weickmann, J. C. Tiller, R. Thomann, and R. Mülhaupt, "Metallized organoclays as new intermediates for aqueous nanohybrid dispersions, nanohybrid catalysts and antimicrobial polymer hybrid nanocomposites," *Macromolecular Materials and Engineering*, vol. 290, no. 9, pp. 875–883, 2005.
- [20] R. Scaffaro, L. Botta, A. Maio, and G. Gallo, "PLA graphene nanoplatelets nanocomposites: Physical properties and release kinetics of an antimicrobial agent," *Composites Part B: Engineering*, vol. 109, pp. 138–146, 2017.
- [21] R. Scaffaro, L. Botta, A. Maio, M. C. Mistretta, and F. P. La Mantia, "Effect of graphene nanoplatelets on the physical and antimicrobial properties of biopolymer-based nanocomposites," *Materials*, vol. 9, no. 5, article 351, 2016.
- [22] V. H. Campos-Requena, B. L. Rivas, M. A. Pérez, K. A. Garrido-Miranda, and E. D. Pereira, "Polymer/clay nanocomposite films as active packaging material: modeling of antimicrobial release," *European Polymer Journal*, vol. 71, pp. 461–475, 2015.
- [23] C. Viseras, C. Aguzzi, P. Cerezo, and M. C. Bedmar, "Biopolymer-clay nanocomposites for controlled drug delivery," *Materials Science and Technology*, vol. 24, no. 9, pp. 1020–1026, 2013.
- [24] GB/T21510-2008, Antimicrobial property detection method for nano-inorganic materials.
- [25] S. M. M. Meira, G. Zehetmeyer, A. I. Jardim, J. M. Scheibel, R. V. B. de Oliveira, and A. Brandelli, "Polypropylene/montmorillonite nanocomposites containing nisin as antimicrobial food packaging," *Food and Bioprocess Technology*, vol. 7, no. 11, pp. 3349–3357, 2014.
- [26] H. He, Z. Ding, J. Zhu et al., "Thermal characterization of surfactant-modified montmorillonites," *Clays and Clay Minerals*, vol. 53, no. 3, pp. 287–293, 2005.
- [27] R. Scaffaro, L. Botta, A. Frache, and F. Bellucci, "Thermo-oxidative ageing of an organo-modified clay and effects on the properties of PA6 based nanocomposites," *Thermochimica Acta*, vol. 552, pp. 37–45, 2013.
- [28] R. Scaffaro, L. Botta, S. Marineo, and A. M. Puglia, "Incorporation of nisin in poly (ethylene-co-vinyl acetate) films by melt processing: a study on the antimicrobial properties," *Journal of Food Protection*, vol. 74, no. 7, pp. 1137–1143, 2011.
- [29] A. Moslemizadeh, S. Khezerloo-ye Aghdam, K. Shahbazi, H. Khezerloo-ye Aghdam, and F. Alboghobeish, "Assessment of swelling inhibitive effect of CTAB adsorption on montmorillonite in aqueous phase," *Applied Clay Science*, vol. 127-128, pp. 111–122, 2016.
- [30] H. Slosiariková, J. Bujdák, and V. Hlavatý, "IR Spectra of octadecylammonium-montmorillonite in the range of the Si-O Vibrations," *Journal of Inclusion Phenomena and Molecular Recognition in Chemistry*, vol. 13, no. 3, pp. 267–272, 1992.
- [31] L. Jiao, F. Lin, S. Cao, C. Wang, H. Wu, and M. Shu, "Preparation, characterization, antimicrobial and cytotoxicity studies of copper/zinc-loaded montmorillonite," *Journal of Animal Science Biotechnology*, vol. 8, no. 1, p. 27, 2017.
- [32] H. Liu, Y. Du, J. Yang, and H. Zhu, "Structural characterization and antimicrobial activity of chitosan/betaine derivative complex," *Carbohydrate Polymers*, vol. 55, no. 3, pp. 291–297, 2004.